Ore breakage characterisation of UG2 deposits using the JK RBT

Christopher Chikochi

A dissertation submitted to the Faculty of Engineering and the Built Environment, University of Cape Town in fulfilment of the requirements for the degree of Master of Science in Chemical Engineering.

June 2017

ABSTRACT

Ore breakage characterisation is a methodology that is used to determine the ore hardness, or resistance to breakage which can be compared across a database of different rock types. It thus develops a relationship between specific energy input and degree of breakage which can be applied to impact breakage in comminution devices. The present study is focussed on investigating the breakage properties of UG2 chromitite, pyroxenite, spotted anorthosite and mottled anorthosite grab samples from run-of-mine (RoM) ore stockpile (particle selection method) and cut drill core particles (cut core method).

A mineralogical analysis of UG2 chromitite, pyroxenite, spotted anorthosite and mottled anorthosite was performed using Leica EZ4D optical microscope and QEMSCAN 650F to determine their mineral composition and texture. The presence of cracks in chromitite stockpile and cut drill core samples was also explored using a Nikon XTH 225 ST micro-focus X-ray system. RoM ore stockpile and cut drill core particles of each of these rock types were subjected to impact breakage in the JK Rotary Breakage Tester (RBT). The progeny particle size distributions and degrees of breakage of UG2 rock types obtained via the particle selection and cut core methods were compared. Standard breakage characterization models were fitted to the breakage data of different rock types and the relative hardness parameters compared.

It was found that UG2 chromitite comprised mainly fine, isolated, round chromite grains in a plagioclase matrix. Pyroxenite samples were found to be made up of granular orthopyroxene, interstitial plagioclase and clinopyroxene. The mineralogical analysis also revealed that spotted anorthosite primarily contains plagioclase with orthopyroxene crystals forming isolated “spots” creating a poikilitic texture. Mottled anorthosite is made up of mainly plagioclase.

Results from breakage tests showed that the progeny particle size distributions and the degrees of breakage for particles sourced from the RoM ore stockpile breaks into a finer product compared to cut drill core samples. This was attributed to the presence of cracks in the RoM ore particles as revealed by the tomographic scans. No visible cracks were found in the cut core particle.

The ore hardness parameters were determined from fitting the breakage data to standard impact breakage characterisation models (t_{10} breakage and size dependent

breakage model). Samples obtained via the particle selection method were consistently found to offer less resistance to impact breakage as shown by the higher Axb values compared to the cut drill core samples. Using the ore hardness classes presented by Napier-Munn et al (1999), UG2 chromitite, spotted anorthosite, mottled anorthosite and pyroxenite were thus classified as very soft, soft to very soft, soft to very soft and medium to soft respectively.

The hardness indicator, $3600.M.f_{mat}.x$, for each size class determined using the parameters obtained from the size dependent breakage model decrease with an increase in the parent particle size. This shows that particles become more resistant to impact breakage as the initial particle size increases. However, for pyroxenite, spotted and mottled anorthosite, the indicator decreases between the particle sizes 14 to 28.6 mm but then increases for 41.1 mm.

PLAGIARISM DECLARATION

I declare that this dissertation, submitted for the degree of Master of Science in Chemical Engineering at the University of Cape Town is my own work, and has not been submitted prior to this for any degree at this university or any other institution.

I know the meaning of plagiarism and declare that all the work in the document, save for that which is properly acknowledged, is my own.

This thesis/dissertation has been submitted to the Turnitin module (or equivalent similarity and originality checking software) and I confirm that my supervisor has seen my report and any concerns revealed by such have been resolved with my supervisor.

Signed by candidate

Signature Removed

Signature: ----------

Date: 03th of April 2017

TABLE OF CONTENTS

ACKNOWLEDGEMENTS

I would like to express my sincere gratitude to my supervisors, Dr Lawrence Bbosa and Professor Aubrey Mainza for their unparalleled supervision, support, encouragement, suggestions and advice throughout the study.

I would also like to thank the Department of Chemical Engineering (University of Cape Town) for their financial support. This project would not have been a success without them.

My sincere appreciation is extended to Lonmin Platinum for their support and providing the facility, equipment and material for a large part of the test work. Special mention goes to Phil Mostert, Kaja Tshimanga, Victor Ross, Nomonde Solomon and the team at the Concentrator's Technical Centre.

To Dr Megan Becker, Lunga Bam, Gaynor Yorath and Silvio Elias, I am really grateful for your assistance and support with the mineralogical studies of this work. I would also like to thank CMR for the support throughout my experimental work

My utmost gratitude goes to my parents (Mr & Mrs Chikochi), siblings (Tendai, Ozasala, David and Bridget) and family members for the continuous support and believing in me always. I would also like to thank my friends for their moral support and encouragement. A special mention goes to Tafadzwa Marozva, Thembeka Ncube, Veronica Munyongani and Wonder Chimonyo. To Stacey (Ruvimbo), may you be a source of happiness in our lives forever. To my lovely wife, Patience, thank you for being patient and supportive throughout this work.

Above all I would like to thank God Almighty for making all things possible.

"Tinongoti Ebenezer, Jehovah matisvitsa pano"

List of Figures

List of Tables

List of Abbreviations

DWT	Drop Weight Tester
SHPB	Split Hopkinson Pressure Bars
UFLC	Ultrafast Load Cell
RBT	Rotary Breakage Tester
XRD	X-ray Diffractometry
SEM	Scanning Electrons Microscope
EDX	Energy Dispersive X-ray
BSE	Back Scattered Electron
QEMSCAN	Quantitative Evaluation of Minerals with Scanning Electron Microscopy
MLA	Mineral Liberation Analyser
UCT	University of Cape Town
CSIRO	Commonwealth Scientific and Industrial Research Organisation
JKMRC	Julius Kruttschnitt Mineral Research Centre
RBT	Julius Kruttschnitt Rotary Breakage Tester
PSM	Particle Selection Method
CCM	Cut Core Method
UG2	Upper Group 2
PGM	Platinum Group Mineral
BMS	Base Metal Sulphides

Symbols and Nomenclature

E_k	kinetic energy
m	mass of the particle
Vi	velocity of the particle prior to impact
E_{cs}	specific input energy (kWh/t)
r	rotor radius (m)
N	rotor speed (rpm)
C	velocity constant
t_{10}	size distribution 'fineness' index
A and b	impact breakage parameters
Esv	volumetric specific input energy (kWh/m^3)
d	particle size (mm)
α∞, βm and n	three model parameters fitted to the drop weight test data
f_{mat}	material breakage property (kg J^{-1} m^{-1})
x	initial particle size(m)
$W_{m,kin}$	mass-specific kinetic impact energy (J kg^{-1})
$W_{m,min}$	threshold energy below which breakage does not occur(J kg^{-1})
k	successive number of impacts with the single impact energy
M	maximum t_{10} for a material subject to breakage (%)
E_{min}	threshold energy (J kg^{-1})
D_n^*	"damage" or fractional reduction in particle
γ	specific strain energy absorbed by particle
E_{n-1}	energy required to disintegrate particle

1. INTRODUCTION

1.1 Background of the research

In most mineral processing circuits, comminution devices such as crushers, tumbling mills and grinding rolls are employed in the size reduction of run-of-mine (RoM) ore to liberate valuable minerals (Wills & Napier-Munn, 2006). Particulate materials in these devices are fractured primarily by impact (Kapur et al., 1997; Crabtree et al., 1964). This mode of breakage determines the throughput for circuits which employ these devices (Napier-Munn et al., 1996). Impact breakage is induced through rapid application of compressive stress as normal forces to the particle surface resulting in disintegrative fracture (body breakage) (King, 2001).

It has been well established by many authors that comminution devices consumes relatively high amounts of energy (Fuerstenau & Abouzeid, 2002; Napier-Munn et al., 1996; Schoenert, 1986). Cohen (1983) estimated that 30-50% of the total power draw of most mineral processing plants is consumed by comminution devices. As a consequence, the power costs associated with the comminution process usually forms more than half of many mineral processing plants' capital and operating cost (Morrell at al., 1991).

The principal reason for the high energy consumption is that comminution devices are typically inefficient in their use of energy (Umucu et al., 2013; Napier-Munn et al., 1996). Considerably more energy is consumed in driving and operating the equipment rather than in the breakage of the particles (Tavares & King, 1998). The energy that is used in size reduction is estimated to be the range of 0.1 to 5% of the supplied energy (Cleary, 1998). Napier-Munn et al (1996) also pointed out that ore particles must be heavily stressed to break into smaller fragments and this process requires large amounts of energy.

In addition, Bueno *et al* (2013) and Hahne *et al* (2003) reported that run-of-mine ore composition strongly affects the performance (energy consumption and target grind) in the comminution circuits. One of the key factors influencing the performance that can be achieved with respect to each ore type in comminution devices is its hardness or resistance to breakage (Napier-Munn et al., 1996).

Ore hardness, which results from the mineralogy and the minerals grain structure of the ore body, largely affects the time ore particles spend (residence time) in the comminution devices. Hard ores typically limit the mill throughput, due to slower breakdown characteristics. This consequently results in material build-up in the mill which detrimentally impacts the mill power (Bueno et al., 2013). Softer ores affect the product size distribution because they comminute readily to generate more fines.

The Bushveld complex in South Africa is the world's largest source of Platinum Group Minerals (PGMs). It contains approximately 80% of the world's reserves of PGMs (Liddell et al., 1986). There are three distinct PGMs bearing ore bodies within the Bushveld complex namely the Merensky reef, Upper Group 2 (UG2) reef and Platreef (Cramer, 2001).

Ore breakage characterisation is one of the fundamental areas in comminution research in optimising the energy available for breakage (Bourgeois & Banini, 2002). It aims to establish the relationship between specific energy input and resultant product size through various types of laboratory tests on a given ore (Napier-Munn et al., 1996). Rock breakage devices such as the drop weight tester (Napier-Munn et al., 1996), impact load cell (Bourgeois & Banini, 2002), split Hopkinson pressure bars (Hopkinson, 1914) and rotary breakage tester (Shi et al., 2009) have been developed to conduct single-particle breakage tests.

Of relevance to this study is the Julius Kruttschnitt Rotary Breakage Tester (RBT). The RBT was developed as part of an AMIRA P9N project by the *JKTech* to complement the drop weight tester as an ore breakage characterisation device (Shi et al., 2006). It can be used to assess the amenability of ores to breakage via impact (Shi et al., 2009) The RBT overcomes several noted limitations of the drop weight tester, such as the lengthy time required to conduct tests and the limited range of input energies attainable (Kojovic et al., 2008)..

As pointed out by Bueno *et al* (2013), that ore composition to the comminution circuits strongly affects the energy consumption and target grind, there have been attempts by researchers such as Van Eck (2007), Mainza & Powell (2006) to develop a relationship between specific energy input and resultant product of UG2 ore using the drop weight tester. However, these studies did not conduct tests per rock type from the UG2 deposit thus a need to characterise the rock types found in the UG2 ore.

Based on the aforementioned background, this study seeks to investigate the ore breakage behaviour of UG2 abundant rock types sourced from RoM stockpile and cut drill core particles. The RBT is used as a characterisation device based on the standard breakage testing procedure.

1.2 Research objectives

The main objectives of this project are to:

- Select and group the abundant rock types (chromitite, pyroxenite, spotted anorthosite and mottled anorthosite) from the UG2 RoM ore and drill core samples on the bases of visible physical characteristics such as colour, texture, grain size and composition (lithology).
- Determine and compare the mineralogical composition and texture of UG2 chromitite, pyroxenite, spotted anorthosite and mottled anorthosite.
- Conduct standard impact breakage characterisation tests using a Rotary Breakage Tester for the abundant UG2 rock types collected from the RoM ore stockpile (particle selection method) and cut drill core samples (cut core method).
- Determine and compare the product size distribution and the degree of breakage of UG2 chromitite, pyroxenite, spotted anorthosite and mottled anorthosite obtained via the particle selection and cut core methods.
- Fit standard impact breakage characterization models to the breakage data of the abundant rock types.
- Compare the relative hardness parameters of the different rock types, as determined by the fitted models.

1.3 Scope of project

This research project will be limited to ore breakage characterisation of UG2 rock types via impact. The work will characterize different UG2 rock types in terms of their amenability to impact breakage using the RBT. It is well known that run-of-mine ore composition affect the mill power draw and the resultant product distributions. Mineralogical analysis will be done to establish a link between the mineralogical properties of the rocks and their breakage characteristics. Ore hardness parameters will be determined from fitting the breakage data for the different rock types in the UG2 ore to standard impact breakage characterisation models. A comparison of ore

hardness parameters showing the responsiveness to breakage of samples collected from the RoM ore stockpile and cut drill core particles will be made.

1.4 Thesis Structure

This thesis is structured into five chapters followed by references and appendices. An overview of each chapter is presented in this section.

Chapter One: Introduction

An introduction to comminution research is presented highlighting the energy inefficiencies in comminution devices and how ore breakage characterisation is useful in the optimisation of the available energy for breakage. The research objectives and the scope of the study are also outlined in this chapter.

Chapter Two: Literature Review

Chapter two gives a review of the literature pertinent to this study. It concludes by presenting the key findings of the literature review and the proposed hypothesis.

Chapter Three: Experimental Methods

The experimental methodology used to test the validity of the proposed hypothesis is given in this chapter. A description of the materials used, types of ores, sampling methods and equipment used in the study are also given in detail. The conditions and operating procedures are also outlined in this chapter.

Chapter Four: Results and Discussion

Chapter four presents and discusses the results of the experimental work. The mineralogy of the main rock types from the UG2 deposit is presented. The progeny particle size distributions resulting from impact breakage in the RBT and energy-size relationships for each rock type obtained using the two sampling techniques are also presented and discussed.

Chapter Five: Conclusions and Recommendations

This chapter summarises the key findings of this research as well as the recommendations for future studies. The objectives of the study presented in chapter one are revisited as well as the hypothesis proposed to determine if they were addressed.

2. LITERATURE REVIEW

Overview

A review of the literature relevant to the research is presented in this section. Particle breakage research, single particle breakage tests and experimental techniques developed to carry out impact breakage characterisation experiments are briefly reviewed. Also, the standard hardness characterisation models that have been put forward are explored. A review of the mineralisation for the Bushveld Complex specifically for UG2 will also be made. This chapter concludes with summarising the key findings from the literature and presenting the proposed hypothesis.

2.1 Brief background to comminution research

Comminution is the progressive reduction of solid materials from one average particle size to a smaller one (Tavares & King, 1998). In minerals processing, the comminution of rocks that contain valuable minerals (ore) is accomplished through blasting, crushing and grinding. Blasting is achieved via ignition of explosives to remove ores from their natural beds and reduces the in situ rock to a size that is readily transportable (Yahyaei et al., n.d.). Also, blasting usually pre-weakens rock particles, probably due to increase in micro-crack intensity (Napier-Munn, 2014). Alternative mining methods such as rock cutting technology are being sought to replace conventional drilling and blasting (Van Den Berg, 2014). Rock cutting technology involves excavating ore along the reef containing valuable mineral from the rock bed. This will result in less gangue material being processed thus increasing productivity (Pickering & Ebner, 2001).

Most minerals are finely scattered in an ore body and are primarily separated from gangue (liberated) by crushing and grinding (Wills & Napier-Munn, 2006). Crushing and grinding rely on mechanical techniques to comminute the run-of-mine ore (ore entering the mill from the mine).

Industrial comminution processes are well known to be energy inefficient (Umucu et al., 2013). Devices such as crushers, tumbling mills and grinding rolls are installed in many comminution circuits for the size reduction of the extracted ore. Cohen (1983) estimated that 30-50% of the total power draw of most mineral processing plants, and up to 70% for hard ores (Fuerstenau et al., 1999), is consumed in such devices. The major source for the high energy consumption is that most of the energy supplied is

dissipated in powering the equipment than is actually used to break the particles (Tavares & King, 1998). Cleary (1998) reported that 0.1 to 5% of the supplied energy is typically used in actual breakage of particles.

Ore breakage characterisation is one of the major fields in comminution research. Its key aim is to derive the relationship between specific energy input and resultant progeny particles through various types of laboratory testing on a given ore (Napier-Munn et al., 1996). A detailed review on ore breakage characterisation is presented in section 2.5.

A number of studies have been done successfully employing and improving the concepts of ore breakage characterisation (Narayanan, 1985; Leung, 1987; Napier-Munn et al., 1996; Banini, 2000; Bbosa, 2007; Shi & Kojovic, 2007; Larbi-Bram, 2009: Zuo & Shi, 2016).

2.2 Particle breakage

Particle breakage or fracture is the separation of one particulate body into two or more progeny fragments under the action of stress (force per unit cross sectional area) (King, 2001). It is the elementary process that governs comminution (Tavares & King, 1998) as particle sizes are reduced to smaller ones required for further concentration processes like flotation.

The nature of how particulate materials break is governed by the material characteristics, nature of stress fields around and within individual particles (stressing conditions) and the environment (Umucu et al., 2013). Material characteristics relevant to particle breakage include the fracture strength (energy required to cause breakage) and the deformation behaviour (Tavares, 2007). Stressing conditions can be classified by the type of stress applied (compressive, tensile or shear), number of loading points, stressing intensity and stress rate (Wills & Napier-Munn, 2006). Contributions of the environment are generally associated with the presence of moisture or chemical additives which adsorb onto the particle (Hartley et al., 1978).

The fracture of particles depends on their behaviour under applied load. Rock particles exhibit macro measures of response and microfracture mechanisms when placed under an applied force. The macro measures of response are elucidated through

classic rock mechanics whilst microfracture mechanisms can be explained using fracture mechanics.

2.2.1 Rock mechanics

Particle fracture is caused by stress fields which result from applying a force leading to disintegration (Schönert, 2004). The applied force to a particle can be plotted against relative deformation to get a stress–strain relationship that can be analysed to understand single particle breakage phenomena (Sahoo, 2006). The behaviour of a cylindrical rock sample under uniaxial loading can be described by a stress–strain curve shown in Figure 2-1.

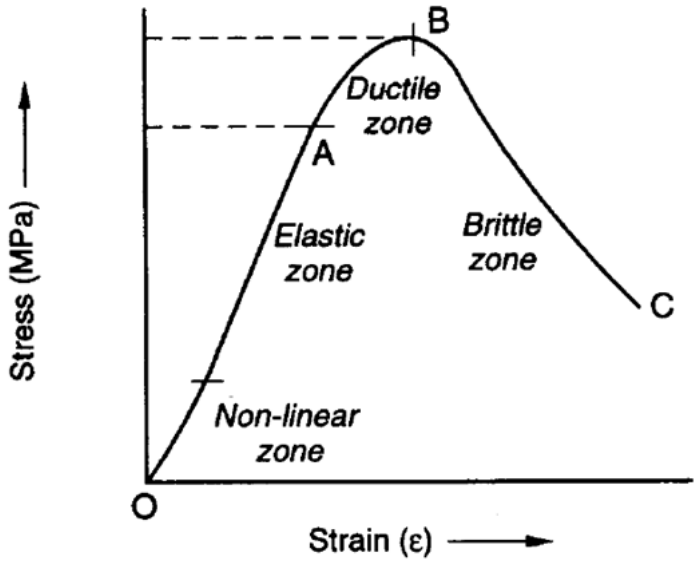

Figure 2-1: Idealised stress-strain relationship for a cylindrical sample of rock under uniaxial compression (Napier-Munn et al., 1996).

A rock sample under compressive loading undergoes elastic deformation (ability to sustain stress without permanent deformation) depicted by the elastic zone in Figure 2-1. The ratio of stress to strain in this region gives the Young's modulus which is a measure of material's ability to return to original shape after deformation (elasticity).

The rock sample continues to deform without losing its ability to resist load in the ductile zone illustrated by region between A and B. Point B is the maximum stress a material can undergo before it breaks (Ultimate Compressive Stress). It denotes the transition from ductile to brittle behaviour.

Except for very small particle sizes, most ore particles are considered to behave as brittle materials (Garcia et al., 2009). As a result, industrial comminution processes deal with the breakage of brittle particles under conditions of applied compressive stress (Umucu et al., 2013). Sudden catastrophic fracture of material occurs in the region between B and C in Figure 2-1. The response of the particulate material to the stress field is largely elastic but significant non-elastic behaviour occurs, particularly at the tips of growing cracks where large quantities of energy are dissipated when the criteria for fracture are met (Umucu et al., 2013).

2.2.2 Fracture mechanics

Fracture mechanics is the field of applied mathematics concerned with the study of the formation and propagation of cracks in materials (Anderson, 2005). The fracture of brittle particles can be considered to take place in two steps i.e. crack initiation and propagation (Garcia et al., 2009). Propagation of cracks break chemical bonds and eventually lead to particle fracture (Anderson, 2005).

A theory of brittle fracture was developed by Griffith (1921). He examined the low tensile strength of glass assuming that small penny-shaped cracks existed throughout the fabric material. He postulated that the low observed strengths of brittle material were due to the presence of internal cracks and flaws which played an important role in the fracture of the material (King, 2001). According to Wills and Napier-Munn (2006), distribution of stress depends upon the mechanical properties of a material, but more importantly upon the presence of cracks or flaws in the matrix. The presence of cracks act as sites for stress concentration (stress raisers) when the particle is under load (Tavares & King, 1998) as illustrated in Figure 2-2.

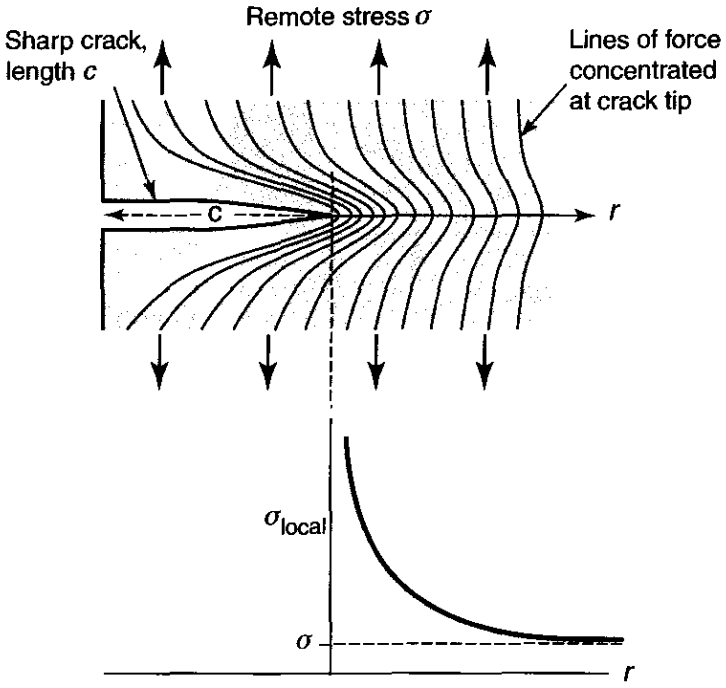

Figure 2-2: Lines of force and local stress variation from a body with sharp crack (Ashby, Shercliff & Cebon, 2007)

The stress at a crack tip was shown by Inglis (1913) to be proportional to the square root of the length of the crack perpendicular to the stress direction. Therefore, there is a critical value for the crack length at any particular level of stress at which the increased stress level at the crack tip is sufficient to break the atomic bond at that point. Such rupture of the bond will increase the crack length, thus increasing the stress concentration and causing a rapid propagation of the crack through the material, resulting in fracture (Wills & Napier-Munn, 2006). Crack growth will occur when there is enough energy to generate new crack surface. This ultimately led to the development of modern theory of fracture mechanics, specifically Linear Elastic Fracture Mechanics (Anderson, 2005).

The theory of Linear Elastic Fracture Mechanics (LEFM) assumes that at the edge of every crack within a loaded material, there is a stress intensity factor (K_I) (Napier-Munn et al., 1996). Furthermore, for every material there exists a critical stress intensity factor (K_{IC}), also known as fracture toughness, which is a measure of the material's resistance to brittle fracture when a crack is present. According to LEFM, for a crack in a material to propagate, K_I should be greater than or equal K_{IC} (Anderson, 2005).

2.3 Mechanisms of particle breakage

Particle size reduction in industrial comminution devices such as tumbling mills occur through three basic mechanisms namely impact, abrasion and attrition (Wills & Napier-Munn, 2006). The three breakage mechanisms are described in Figure 2-3.

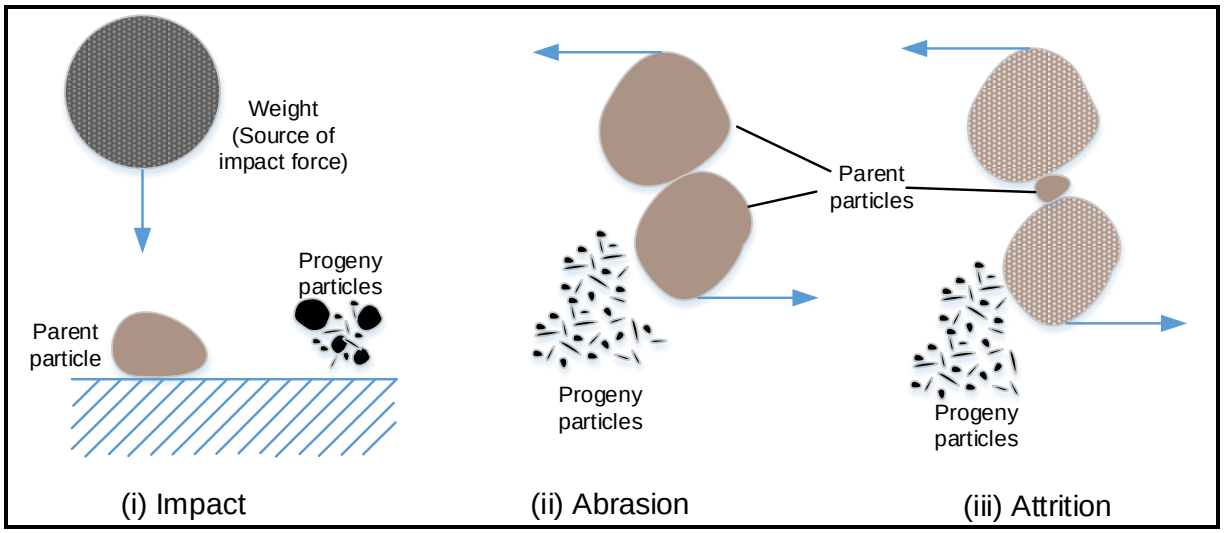

Figure 2-3: Principal breakage mechanism (adapted from Napier-Munn et al., 1996; King, 2001)

Particulate materials are fractured principally by impact (Kapur et al., 1997) shown as (i) in Figure 2-3. This mechanism is induced through rapid application of compressive stress (King, 2001). These are applied as normal forces to the particle surface resulting in disintegrative fracture (body breakage) (Tavares, 2007). A broad spectrum of product sizes is produced. This may occur in form of single particle fracture or bed breakage when the cataracting charge in a tumbling mill impacts the base of the mill (Cleary, 1998).

Subsidiary fracture of particles is produced by high shearing stress resulting from force acting parallel at the surface of the particle (King, 2001). Abrasion and attrition, shown as (ii) and (iii) in Figure 2-3, are surface breakage mechanisms (Wills & Napier-Munn, 2006). The particle suffers gradual wearing of its surface leaving the parent particle largely intact but usually more rounded (King, 2001).

Abrasion occurs when the particle grinds against other particles, gradually wearing it down and reducing it in size as shown in Figure 2-3 (ii). This is usually a characteristic of ore behaviour at the base of mills (Wills & Napier-Munn, 2006). Small pieces of each particle are broken from the surface, leaving the parent particles largely intact.

Attrition takes place when a relatively small particle is trapped and rubbed between two much larger particles as illustrated in Figure 2-3 (iii) or between the mill shell and a particle. The small particle is subsequently broken in preference to the larger ones.

2.3.1 Patterns in particle breakage

Particle fracture occurs along zones of structural weakness resulting in different breakage patterns. Random fracture, intergranular fracture and preferential breakage are some of the breakage patterns displayed in a multi-phase ore (Vassiliev et al., 2008) as shown in Figure 2-4.

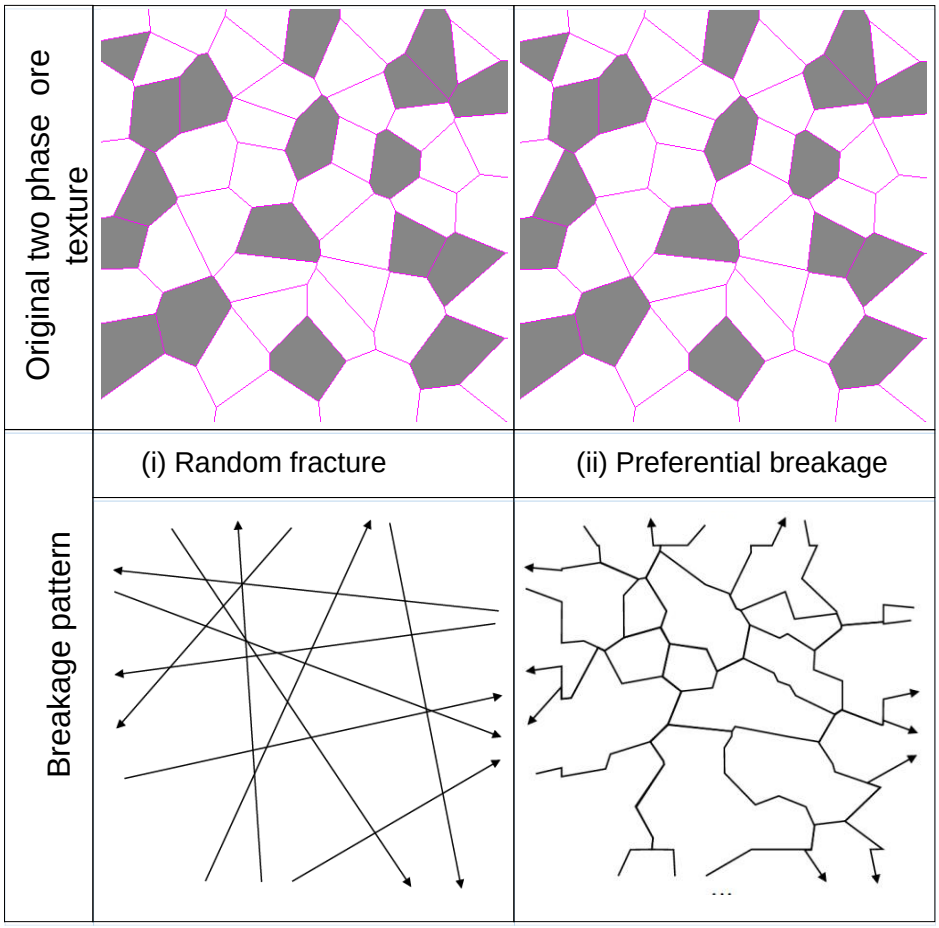

Figure 2-4: Fracture pattern in a two phase ore (adapted from Vassiliev et al (2008))

Random fracture is independent of the ore texture (spatial relationship between the minerals of which a rock is composed) (King, 2001) and there is no selective breakage of one mineral over another. The propagation of cracks in the ore particle is random as shown in Figure 2-4 (i). According to Stamboliadis (2008), during random breakage, all the size classes produced from the same initial particle after several breakage events have the same grade, which is equal to the grade of the initial particle.

When fracture patterns are dependent on the mineralogical texture, the breakage process is considered a non-random fracture (King, 2001). Preferential breakage is one of the non-random fracture patterns identified when multiphase particles are broken (King, 2001). As shown in Figure 2-4 (ii), during preferential breakage, propagation of cracks in an ore particle occur along grain boundaries, resulting in separation of different mineral phases. (Xu et al., 2013). Significant grain boundary fracture will enhance the exposure of minerals during comminution. However, there is no convincing experimental evidence to describe the extent to which this actually occurs in practice or to indicate what processes can be employed to enhance preferential breakage (Garcia et al., 2009). In addition Garcia et al (2009) pointed out that there is a lack of clear fundamental understanding of initiation and propagation of cracks along grain boundary during brittle fracture of multiphase ore particles. Conditions that are favourable for preferential breakage have not yet been identified (Xu et al., 2013).

2.3.2 Rock breakage in AG/SAG mills

In industrial comminution devices such as AG/SAG mills, particles are mainly fractured by impact or compressive loading (Kapur at al., 1997). The size reduction processes via impact in a mill when in steady state are shown in Figure 2-5. The feed enters the mill and is subjected to impact breakage from collision with other particles and/or the mill shell. The products from breakage either exit via the grate if they are smaller than the grate aperture size or remain to undergo further collisions (Morrell et al., 1996).

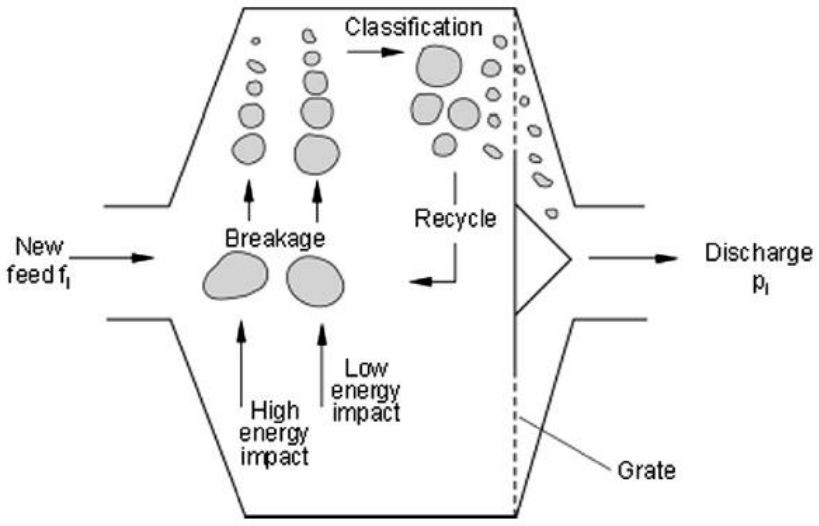

Figure 2-5: Schematic diagram of AG/SAG mill process mechanisms (Morrell et al., 1996)

Morrell et al (1996) showed that rock particles that are fed to the mill are subjected to high and low impact energy. At high impact energy, size reduction of rock particles occur primarily by brittle fracture and crushing producing a broad spectrum of product particle sizes (King, 2001). These energies are mimicked in the JK ore breakage characterisation method for AG/SAG mill modelling (Larbi-Bram, 2009). The specific impact breakage energies used in the characterisation method are in the range 0.1 to 2.5 kWh/t (Napier-Munn et al.. 1996). These impact energies are usually sufficient to cause the particles to fracture in a single impact (Larbi-Bram, 2009).

Some of the rock particles may survive the first cycle and are recycled back to the impact zone. The unbroken particles are progressively weakened by repeated low energy impacts and eventually are comminuted (Kapur et al., 1997).

The feed ore to the comminution circuit often contains various rocks with different mineralogical composition and texture thus different breakage characteristics. Fluctuations in run-of-mine ore composition strongly affect the performance in the comminution devices (Esen et al., 2007) especially in the AG/SAG mills which derives the grinding media from the feed ore (Hahne, Pålsson & Samskog, 2003). The hard components usually limit the mill throughput, due to its slower breakdown characteristics. As a result, the material preferentially accumulates in the mill contents adversely impacting the mill power (Bueno et al., 2013). Softer ores affect the product size distribution as they comminute readily to generate more fines.

The fundamental properties of the fracture process of particulate materials can be studied most effectively by well-controlled experiments on single particles (Tavares & King, 1998). The subsequent section will thus explore the single particle breakage tests.

2.4 Single particle breakage tests

Single particle breakage is the most efficient size reduction method as energy losses by friction and unsuccessful impact events are minimized or avoided altogether and losses due to particle–particle interactions do not exist (Tavares, 2004) Single particle breakage tests have been used to elucidate a number of phenomena in particle breakage, including:

- energy utilization in the comminution process and a measure of the different types of losses (Tavares, 1999),
- effect of particle size, shape, material physical properties and modes of loading on particle breakage characteristics (Tavares & King, 1998),
- energy-size reduction relationships (Vogel & Peukert, 2004),
- breakage characteristics of materials for modelling comminution and degradation processes (Napier Munn et al., 1996),
- material deformation response under applied stress (Tavares & King, 2004).

Various testing methods have been used to measure the breakage characteristics of single particles subjected to compression, each allowing investigation over a restricted range of deformation rates. These tests can be classified according to the mode of application of stresses and the number of contact points as shown in Figure 2-6.

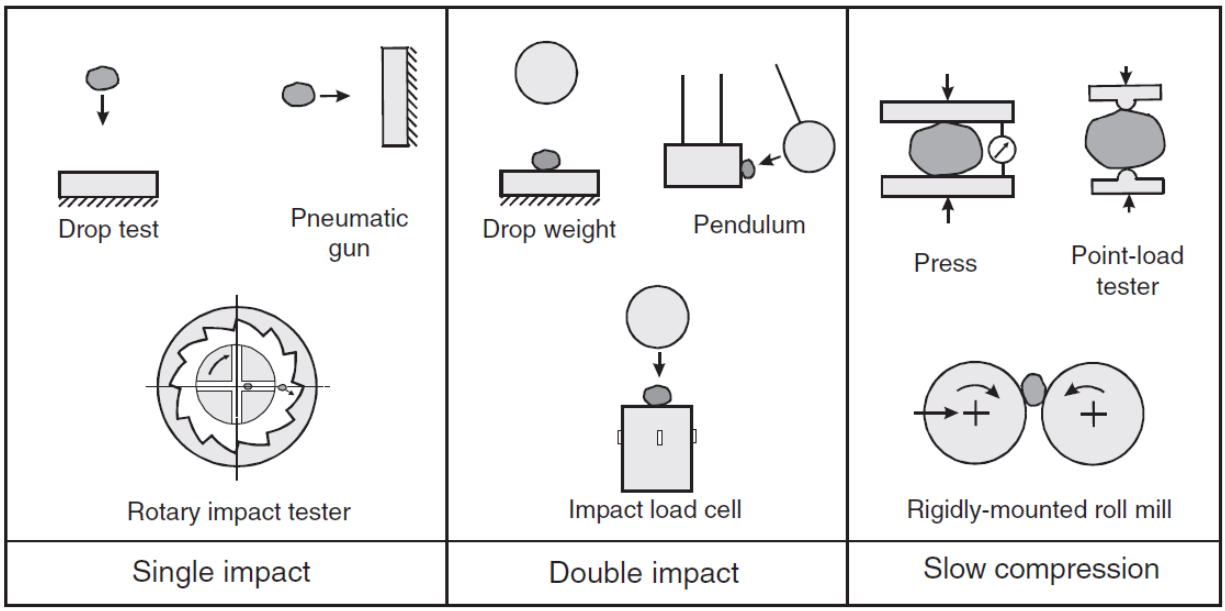

Figure 2-6: Different modes of single particle breakage tests (Tavares, 2007)

As illustrated in Figure 2-6, the test particle is subjected to single impact in three possible ways namely:

- Free fall (low velocity)
- propelling the particle against a hard surface (high velocity)
- subjecting the particle to impact from a hard projectile (high velocity)

According to Narayanan (1985), the degree of breakage generally increases with impact velocity up to a maximum impact velocity depending on the material characteristics. Excess energy from particle fracture is converted to kinetic energy of the progeny particles.

Double impact tests correspond to experiments where a test specimen is crushed between two hard surfaces at a moderate deformation rate as shown in Figure 2-6. These tests can be classified into two types (Sahoo, 2006). The first type is the classical drop weight tests where a particle resting on a hard surface is struck by a falling weight. The second type is known as the pendulum test where a particle is hit by one or two moving hammers or pendulums.

In slow compression tests, a specimen is squeezed in a press. The tests are conducted using uniaxial compression presses or using the rigidly mounted roll mill (Tavares, 2007) as shown in Figure 2-6. The applied force can be plotted against deformation to get a stress–strain relationship that can be analysed to understand single particle phenomena (Napier-Munn et al., 1996).

Some of the common single particle impact breakage experiment devices differing from the mode of application of stresses and the number of contact points as explained include:

- Drop weight tester (DWT)
- Split Hopkinson pressure bars (SHPB)
- Impact load cell (ILC)
- Rotary breakage tester (RBT)

The first three devices will be discussed briefly. However, the rotary breakage tester which was used to conduct experiments for this study will be discussed in detail.

2.4.1 Drop weight tester

A drop weight tester (DWT) is one of the simplest and most commonly used devices for investigating breakage characteristics of materials (King, 2001). It involves dropping a weight from a predetermined height onto a single particle (or a bed of particles) that is supported on a hard surface (anvil) so that it breaks. A schematic diagram of the drop weight tester is shown in Figure 2-7.

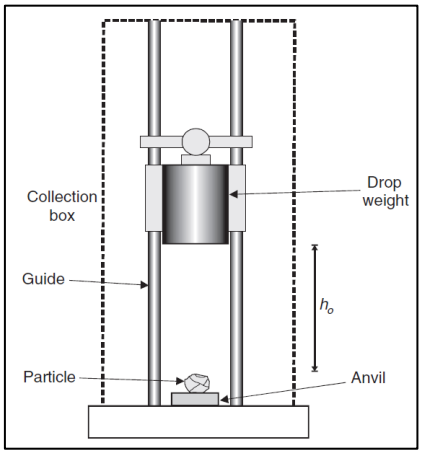

Figure 2-7: Schematic diagram of the drop weight tester (Tavares, 2007).

Assuming conservation of energy, kinetic energy of a weight prior to impact is equal to the available potential energy before the weight is released. This kinetic energy is transferred to a particle, which may or may not fracture. Progeny particles are collected for the determination of product size distribution.

The DWT can be used to determine the breakage and energy utilisation parameters for comminution modelling. A wide range of input energy is achieved by changing the release height (h_o) as well as the mass of the drop weight (standard DWT energy range from 0.01 to 50kWh/t) (Napier-Munn et al., 1996). In addition, the DWT has the ability to conduct particle bed breakage tests (Bearman et al., 1997).

However, the DWT does not give information about the actual energy used by the rock particles during breakage (Bourgeois & Banini, 2002). Also testing of repetitive impacts at small energies using the DWT is time-consuming (Shi et al., 2009). The frictional losses from the guide rails and rebounding velocities from weights at greater heights lower the energy that is transferred to the particle (Radziszewski & Laplante, 2006).

2.4.2 Split Hopkinson pressure bars

Split-Hopkinson pressure bars (SHPB) are apparatus generally used to investigate dynamic compressive properties (e.g. stress-strain response) of materials (Huang et al., 2014). The apparatus typically consists of compression gas gun, striker, two steel bars in series (an incident and transmission bar) which are mounted with strain gauges, with a specimen loaded between them as illustrated in Figure 2-8.

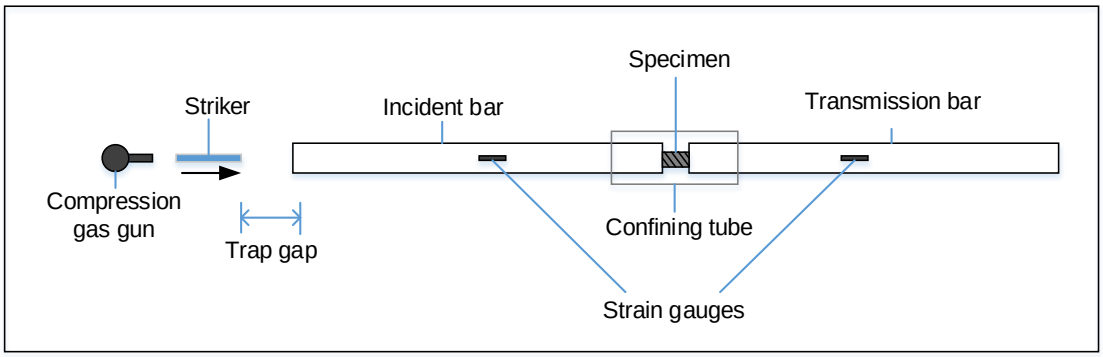

Figure 2-8: Schematic diagram of the Split Hopkinson pressure bars (adapted from Huang et al., 2014)

Compression gas gun launches a striker, which impacts against the incident bar. By a measure of the time taken by the striker to cover the trap gap, the initial kinetic energy of the striker can be calculated as a confirmation of the impact energy (Bbosa et al., 2006). The impact causes an elastic compression wave to travel in the incident bar towards the specimen (Frew et al., 2001). A portion of this wave follows through to the transmission bar while the remainder is reflected through the incident bar. The deformation waves that travel through the bars are measured by strain gauges mounted on both bars (Napier-Munn et al., 1996). These signals can be captured and recorded over the entire loading duration by a computer and used to resolve force to fracture, incident strain energy, and the fraction of this energy that is absorbed by the sample during impact.

The technique allows for measurement of loads and their interactions with specimens and provides data that can be used to assess how stress and energy interactions lead to breakage. Also, the SHPB allows incremental breakage tests as shown successfully by Bbosa et al (2006). The test is limited to lengthy time taken to perform experiments.

2.4.3 Impact load cell

Impact Load Cell (ILC) is a hybrid of the drop weight tester and Split Hopkinson Pressure Bar (Tavares & King, 1998). It allows in-situ characterisation of single-particle impact breakage of different material (Bourgeois & Banini, 2002).

The ILC typically consists of a long vertical steel rod instrumented with solid-state strain gauges. The strain gauges capture the impact event on which a single particle or a bed of particles is placed and impacted by a falling steel ball. A laser accelerometer set just above the particle measures the velocity of the falling steel ball prior to impact. A schematic diagram of the arrangement of the ILC is shown in Figure 2-9.

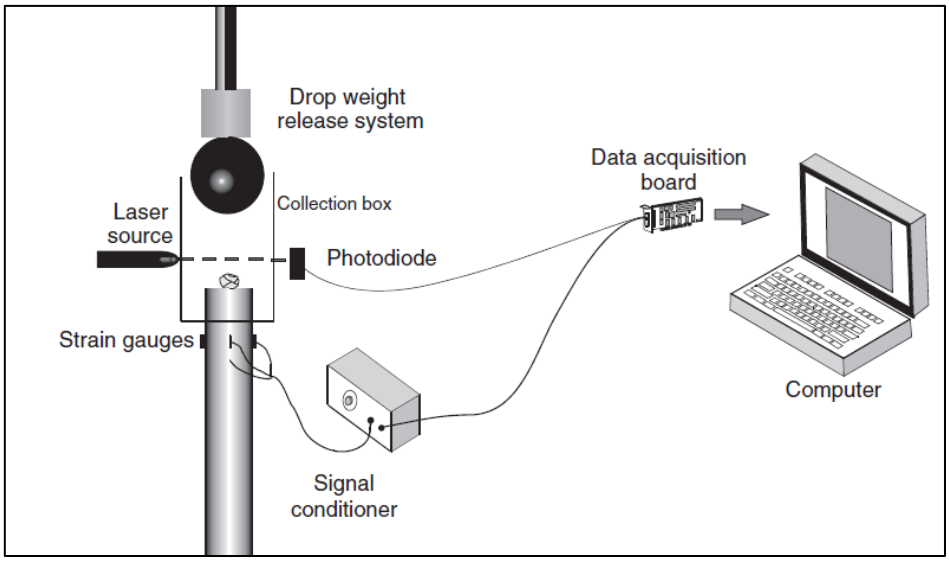

Figure 2-9: A schematic diagram of the impact load cell (Tavares, 2007).

The compressive wave resulting from the force exerted by the ball on the single particle (or particle bed) during impact travels down the rod and is detected by the solid-state strain gauges (Tuzcu et al., 2012). This results in a voltage change in the Wheatstone bridge (signal conditioner), which is then recorded as a function of time using a computer software (Tavares & King, 1998).

The ILC can be used for single particle and bed breakage characterisation. It also provides force-time measurements during impact (Bourgeois & Banini, 2002).

2.4.4 JK Rotary Breakage Tester

JK Rotary Breakage Tester (RBT) is a rapid breakage characterisation testing device developed by the Julius Kruttschnitt Mineral Research Centre (JKMRC) comminution research team to complement the drop weight tester (Shi et al., 2009). The JKRBT overcomes noted limitations of the drop weight tester such as lengthy time required to perform tests and the limited range of input energies achievable (Kojovic et al., 2008). A schematic diagram of the RBT is presented in Figure 2-10.

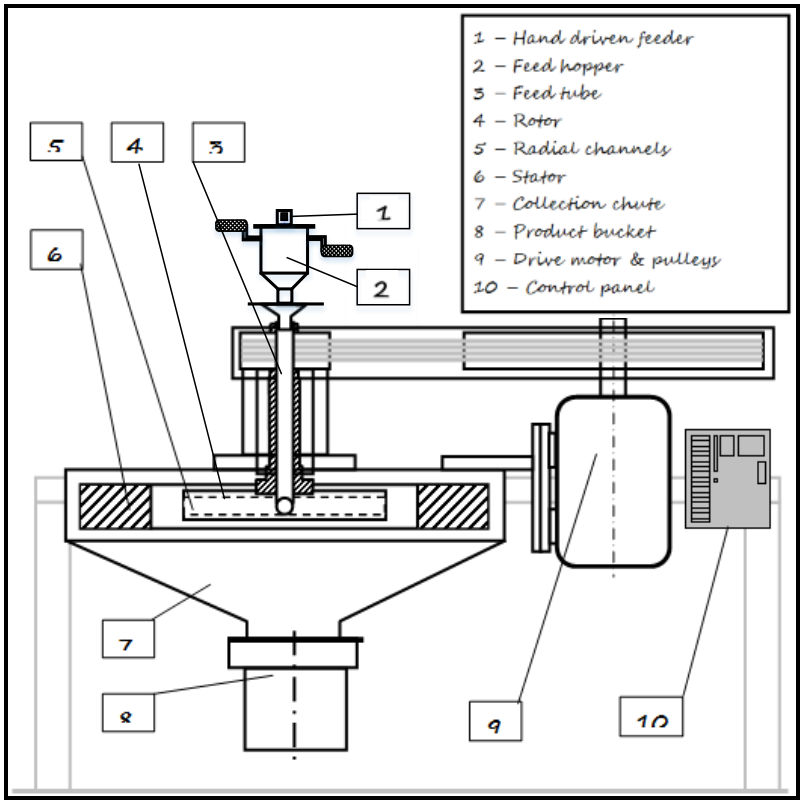

Figure 2-10: A labelled systematic diagram of the JK Rotary Breakage Tester prototype (adapted from Shi et al., 2006)

The RBT consists of three basic systems, namely, feeding system, impacting and product collection (Larbi-Bram, 2009). Pre-sized particles are fed manually to the rotating centrifuge (rotor), shown as 4 in Figure 2-10, through a hand driven feeder. The feeder (1) has compartments which are manually fed with rocks to control the feeding rate of one particle at a time to ensure single particle impact breakage mode.

The RBT uses a rotor-stator impacting system, in which particles gain a controlled kinetic energy while they are spun in a rotor with a number of guiding radial channels (Shi et al., 2009). The particles are then ejected and impacted against anvils mounted

in a surrounding stator (6) causing the particles to break. The rotor speed is controlled and displayed on the control panel.

The broken product drops onto a collecting chute which is radially inclined (7) and reports to a product collection bucket (8) by gravity. A vacuum automatically switches on when the rotor is stopped to suck finer material into the product bucket.

The particles are broken under impact at the required specific input energy using the RBT. The specific input energy of each impact, E_{cs}, is the kinetic energy per particle mass and is related to the particle velocity through equation 2 -1.

$$E_{CS} = \frac{E_K}{m} = \frac{0.5 \times m \times V_i^2}{m} = 0.5 \times {V_i}^2 \qquad \ldots\ldots\ldots\ldots\ldots\ldots\ (2-1)$$

where E_k is the kinetic energy, m is the mass of the particle and V_i is the velocity of the particle prior to impact

Specific input energy depends solely on the impact velocity (V_i) as shown by equation 2-1 (Shi et al., 2009). The impact velocity is the resultant of the rotor tangential velocity (V_t) and the radial velocity (V_r) as shown in Figure 2-11.

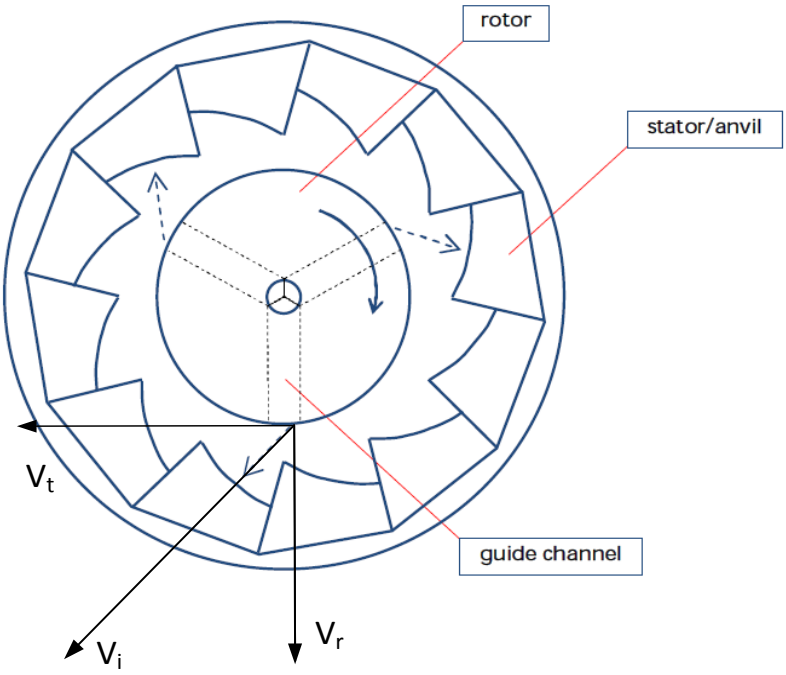

Figure 2-11: Sketch of the velocity components of a particle being ejected from the rotor (adapted from (Shi & Kojovic, 2011)

The velocity the particle possesses as it is ejected from the rotor is given by equation 2-2:

$$V_i^2 = V_r^2 + V_t^2 \quad \ldots\ldots\ldots\ldots\ldots\ldots\ldots \quad 2-2$$

It can be assumed that the velocity at which the particle is ejected is the same as the impact velocity at the stator (Bbosa, 2007). This is because the rotor spins at constant velocity and the particle travel relatively a short distance after leaving the radial channels to the stator. If the two velocity components (V_r and V_t) are assumed to be equal, V_i is given by:

$$V_i = \sqrt{2\,V_t} \quad \ldots\ldots\ldots\ldots\ldots\ldots\ldots \quad 2-3$$

The actual impact velocity of a particle is smaller due to frictional losses in the guide channel. Hence, a constant C is introduced to account for the efficiency of a given design is in transferring the kinetic energy from the rotor to the particle fed into the machine (Shi et al., 2009). The specific input energy is then determined from equation 2-4:

$$E_{CS} = \frac{0.5 \times \left[C \times \sqrt{2} \times \frac{2 \times \pi \times N \times r}{60}\right]^2}{3600} = 3.046 \times 10^{-6} C^2 N^2 r^2 \quad \ldots\ldots\ldots\ldots\ldots \quad (2-4)$$

where E_{cs} is the specific input energy (kWh/t), r is the rotor radius (m), N is the rotor speed (rpm), and C is the velocity constant (Shi et al, 2009).

The RBT allows rapid characterization of particle impact breakage properties. One RBT test (equivalent to one standard DWT) can be completed in approximately 1/8th to 1/10th of the time it takes to complete a DWT test (Larbi-Bram, 2009). The RBT can be used for both single impact and incremental breakage as demonstrated in work such as Bbosa (2007), Bonfils and Powell (2013). The ability to test a large number of particles offers statistically more reliable results. Although the RBT predicts the impact velocity and thus available impact energy to test particles, it cannot quantify how much of this is actually utilized to cause breakage.

2.5 Ore breakage characterisation

Ore breakage characterisation is a process of assessing how particulate materials fracture in comminution devices, such as crushers or tumbling mills (Napier-Munn et al., 1996). It generates parameters that are used to describe the resistance of particles to breakage (hardness). Ore feed supplied to the comminution circuit is composed of various rock types with different characteristics (Hahne et al., 2003). Ore breakage characterisation therefore allows the mapping of the different rock types, in terms of their hardness, within the feed being supplied to the comminution circuit.

Variations in ore characteristics or blending of different rock types mined from different deposits result in throughput fluctuations in comminution devices (Williams & Holtzhausen, 2001). These fluctuations consequently affect the estimation of the energy requirements and product characteristics in these devices (Hahne et al., 2003). This has led to the increasing significance of ore breakage characterisation (Bourgeois & Banini, 2002) particularly in optimising comminution processes.

2.5.1 Effect of input energy on the resultant breakage

The input energy in comminution processes has been identified as the most significant variable controlling the progeny size distribution from single-particle breakage (Tavares, 2007).

Kick (1885) observed that input energy was proportional to the volume of material broken and proposed another energy-size reduction relationship. He formulated a "law of comminution" based on the assumption that energy supplied to a body increases the level of strain within the body to propagate its internal micro-cracks and that the strain energy of the body is proportional to its volume. Tavares (2007) also pointed out that increasing the input energy, increases the stressing intensity which will inturn intensifies the propagation of cracks in a material.

As a consequence of the increase input energy, the degree of breakage generally increases (Narayanan, 1985; Kapur et al., 1997; Banini, 2000; Shi & Kojovic, 2007). However, particles of infinite fineness are not produced in a single loading event by increasing indefinitely the stressing energy, so that a maximum progeny size distribution is reached (Napier-Munn et al., 1996). The maximum product size distribution depends on the spatial distribution of fragments from the first few fracture

events, loading geometry, loading rate and on the material's amenability to agglomerate (Tavares, 2007).

Bonfils and Powell (2013) highlighted that a particle that survives an impact becomes increasingly weaker with repeated impact cycles and eventually breaks if the energy supplied is above energy threshold (See Section 2.6.2). Krogh (1980) demonstrated that anorthosite particles become increasingly weaker after receiving multiple impacts. A similar trend was reported by Pauw and Maré (1988) who found that after repeated impacts at a very low energy level, quartzite particles were eventually broken. Furthermore, Tavares and King (2002) showed that particle weakening from repeated impacts is the result of the growth of crack-like damage

2.5.2 Effect of particle size on the resultant breakage

The effect of the particle size on the resultant has been investigated extensively in work such as Tavares and King (1998), Banini (2000), Shi and Kojovic (2007). Tavares and King (1998) observed that the ability of a particle to withstand a force without fracturing (particle strength) increases with a decrease in particle size. In view of this, bigger particles tend to offer less resistance to breakage (weaker) and therefore easier to break than smaller particles. These findings were also confirmed by Banini (2000) as well as Shi and Kojovic (2007). This trend is because the crack density of larger particles is much greater than that for smaller particles (Tavares & King, 1998). As pointed out in Section 2.2.2, the presence of internal cracks and flaws plays an important role in the fracture of the material.

However, Banini (2000) fitted the A and b parameters (see Section 2.6.1) to all the materials tested. He observed that for some materials the fitted parameters varied irregularly with particle size as illustrated in Figure 2-12.

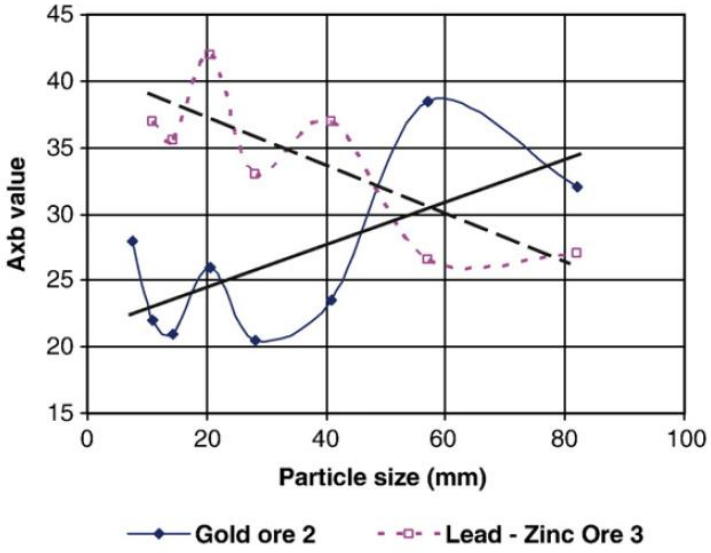

Figure 2-12: Relationship between the product of parameters A and b and the particle size for materials without regular size effect (redrawn by Shi and Kojovic (2007) after Banini (2000)).

From the results presented in Figure 2-12, Banini (2000) concluded that there are some materials without a significant size effect.

2.6 Standard impact breakage characterisation models

Breakage or hardness characterisation models involve an application of mathematical relations to represent the relationship between the input energy and the resultant size distribution (Napier-Munn et al., 1996). A single curve comprising the breakage performance of various materials can be used to describe the breakage probability of different materials (Vogel & Peukert, 2004). This information is useful in predicting the performance in comminution devices (Morrell et al., 1996; Bueno et al., 2013).

2.6.1 t_{10} breakage model

The work done by Leung (1987) developed an appearance or breakage distribution function. This is a description of how an ore particle in an AG/SAG mill breaks when energy is imparted to it (Morrell et al., 1996). Leung (1987) showed that the relationship between the degree of breakage represented by the percentage material passing $1/10^{th}$ of the original feed size (t_{10} parameter) and the specific input energy, (E_{cs}) is not linear as proposed by Narayanan (1985), but an exponential one of the form shown in equation 2-5.

$$t_{10} = A(1 - e^{-b.E_{cs}}) \qquad \ldots\ldots\ldots \qquad (2-5)$$

where t_{10} is a size distribution 'fineness' index, E_{cs} is the specific input energy (kW h/t), and A and b are the ore impact breakage parameters.

This equation is also implemented in JKSimMet (Mineral Processing Simulator - an industry standard software package) to analyse and predict AG/SAG mill performance (Schwarz & Richardson, 2013; Morrison & Richardson, 2002). The impact breakage parameters, A and b, characterize the material's fragmentation behaviour and can be determined through interpretation of typical t_{10}-E_{cs} curve shown in Figure 2-13 (Tavares, 2007).

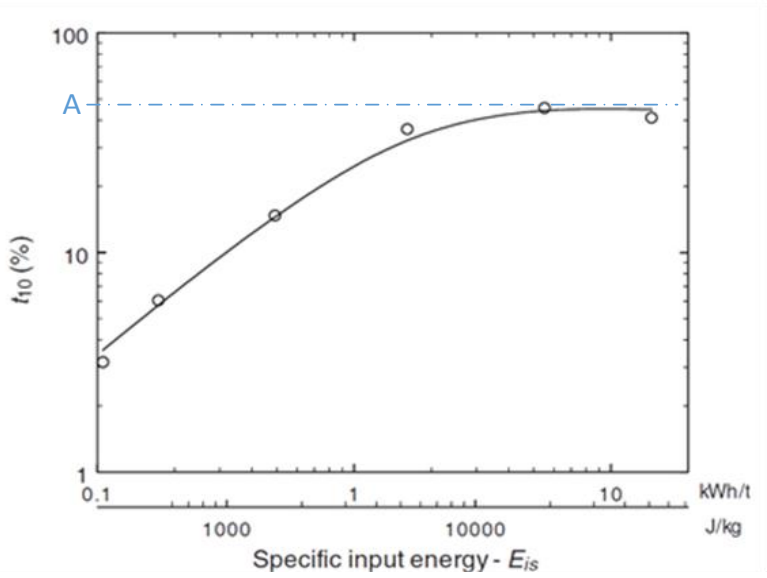

Figure 2-13: Relationship between the parameter t_{10} and specific input energy (E_{cs} or E_{is}) (adapted from Tavares, 2007).

The value of parameter A corresponds to the maximum degree of breakage (t_{10}) obtainable for an ore. It indicates that at higher energies little additional size reduction occurs as the specific input energy is increased. Parameter b is the linear gradient of the curve at energies lower than 1 kWh/t and can be related to material stiffness (Napier-Munn et al., 1996).

Also of significance is the value of slope of the curve at 'zero' input energy derived from equation 2-5. Differentiating equation 2-6 with respect to E_{cs} gives,

$$\frac{dt_{10}}{dEcs} = (-Ae^{-b.Ecs}) \cdot (-b) \qquad \ldots\ldots\ldots \qquad (2-6)$$

Letting E_{cs} in equation 2-6 to approach zero results in:

$$\lim_{Ecs \to 0} \left(\frac{dt_{10}}{dEcs}\right) = Axb \quad \ldots\ldots\ldots\ldots \quad (2-7)$$

Equation 2-7 illustrates that Axb is the slope of the curve at 'zero' input energy. It represents material's amenability to fragmentation via impact (ore hardness indicator) (Shi & Kojovic, 2007). A lower Axb value shows that the ore has a high resistance to impact breakage whilst a higher Axb indicates a readiness to fracture of the ore type (Hahne et al., 2003).

Typical ore hardness classes reported in Table 2-1 were determined using the JK Drop weight tester at the JKMRC.

Table 2-1: Reported ranges of Axb values impact breakage parameters (Napier-Munn et al., 1999).

Property	Very Hard	Hard	Mod. Hard	Medium	Mod. Soft	Soft	Very Soft
A*b	<30	30-38	38-43	43-56	56-67	67-127	>127

Ore particles can be classified by comparing the hardness parameters as presented in Table 2-1.

A comparisons of breakage mechanisms and characterisation data between the JKRBT and the Drop Weight Tester was made by Shi and Kojovic (2011). It was noted that the JKRBT produces a finer product. This is attributable to the differences in breakage modes between the DWT and the JKRBT. As discussed in section 2.4, there are two points of contact in the DWT test when a force is loaded on a particle, while in the JKRBT test, there is only one contact point (Tavares, 2007). Shi and Kojovic (2011) pointed out that 2-point breakage is less efficient than 1-point breakage at the same specific applied energy. Shi and Kojovic (2011) also discussed the difference in the specific energy, strain rate and the potential for secondary breakage for the two breakage characterisation devices.

Despite the differences in the breakage modes, the JKRBT can provide statistically similar A*b parameters, by using a data reduction procedure which takes into account the difference in the number of contact points, strain rate and potential for secondary

breakage. However, no publication has been made which explains the data reduction procedure.

Some of the limitation of Leung's approach as noted by Larbi-Bram (2009) and Banini (2000) are:

- The method assumes that the size of the particle does not affect the breakage process and thus the mass and the particle size are not factored in resultant breakage model. The study conducted by Banini (2000) to model the particle size effect on ore breakage demonstrated that A and b are usually not constant over all particle size.
- The model does not account for material properties. Work done by Vogel and Peukert showed that the breakage probability is related to material properties (Vogel & Peukert, 2003, 2004, 2005).
- Leung's approach does not consider the effect of particle interaction associated with different number of particles. Banini (2000) showed that the number of particles inside a mill can significantly influence the abrasion index.

As a result, Shi and Kojovic (2007) modified the breakage probability model published by Vogel and Peukert (2004) to develop a size-dependent model shown in equation 2-9 (in section 2.6.2) to describe the degree of breakage.

2.6.2 Size dependent breakage model

Vogel and Peukert developed a breakage probability which depends on the mass-specific impact energy, a minimum energy required to cause any particle fracture, the initial particle size and a material parameter which describes the material-specific breakage behaviour (Vogel and Peukert, 2004). The model expresses breakage probability (S) in terms of a series of parameters given in equation 2-8.

$$S = 1 - \exp\{-f_{mat}.x.k\,(W_{m,kin} - W_{m,min})\} \qquad \ldots\ldots\ldots\ldots\ldots\ldots \quad (2-8)$$

where f_{mat} (kg J^{-1} m^{-1}) is the material breakage property, x (m) the initial particle size, $W_{m,kin}$ (J kg^{-1}) the mass-specific kinetic impact energy, $W_{m,min}$ (J kg^{-1}) the threshold energy below which breakage does not occur, and k the successive number of impacts with the single impact energy (Vogel and Peukert, 2004).

Shi and Kojovic (2007) argued that the qualitative description of the breakage function to know whether a particle will break (breakage probability) presented by Vogel and Peukert (2004) is only a part of the process. It is more important to know the particle progeny size distribution subject to breakage. A modification to the Vogel and Peukert's breakage probability model to describe the degree of breakage, t_{10} (%), in relation to material property, particle size and net cumulative impact energy, is given as follows:

$$t_{10} = M\{1 - exp[-f_{mat}.x.k\,(E_{cs} - E_{min})]\} \qquad \ldots\ldots\ldots\ldots\ldots\ldots \quad (2-9)$$

where M (%) represents the maximum t_{10} for a material subject to breakage, E_{cs} (J kg^{-1}) the mass-specific impact energy, and E_{min} (J kg^{-1}) the threshold energy (Shi & Kojovic, 2007).

The modified model directly correlates to the t_{10} breakage model (equation 2-5) such that the value of A would be replaced by M, while b replaced by f_{mat}.x, and E_{cs} replaced by k(E_{cs}-E_{min}). Shi and Kojovic (2007) fitted both the t_{10} breakage model (equation 2-5) and the size dependent model (equation 2-9) to the data of Mt Coot-tha quarry material as shown in Figure 2-14.

(a)

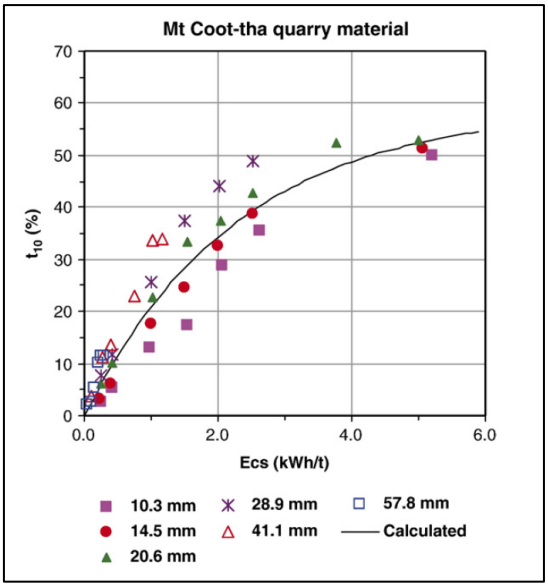

(b)

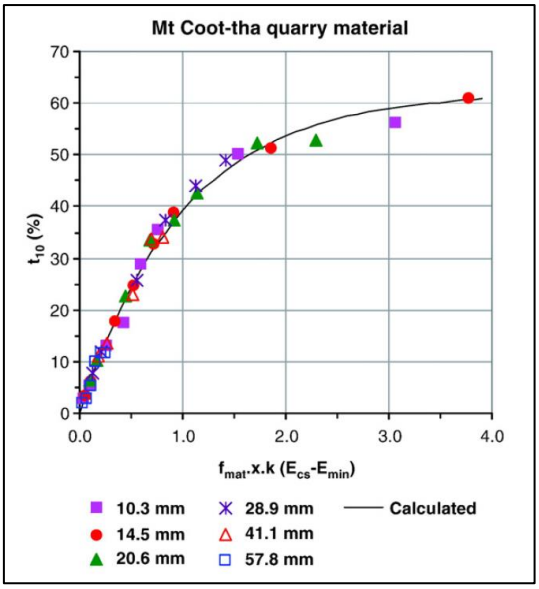

Figure 2-14: Example of (a) t_{10} against E_{cs} and (b) t_{10} against f_{mat}.x.k (E_{cs}-E_{min}) curves (Shi & Kojovic, 2007).

The plots, (a) and (b), in Figure 2-14 show that the two models estimate the same maximum value for t_{10} (approximately 60%). However, the size dependent model fits all the data sets better as compared to the t_{10} breakage model.

2.7 Process mineralogy

Process mineralogy in the mining industry is the application of scientific study of minerals to understand and solve problems encountered during processing of ores, concentrates and smelter product (Petruk, 2000). According to Xiao and Laplante (2004), process mineralogy can also be viewed as an integration of mineral processing and the study of minerals (mineralogy). Its salient characteristics as presented by Baum (2013) include:

- Representative ore sampling
- Characterisation (quantitative mineralogy)
- Interpretation and understanding (including metallurgical tests)
- Prediction of the location of ore bodies, behaviour of ores during processing and potential recovery of certain minerals, metals or elements.

Cropp and Goodall (2013) highlighted that continuous deterioration of ore quality regarding grade, hardness, finer particle sizes and increase of metallurgical complexities has made process mineralogy an integral part of new project development. Mineralogical studies provide information on the ore variability and behaviour of various mineral components during processing by assessing internal structures, compositions, physical, chemical and optical properties of ore bodies (Schouwstra & Smit, 2011). These mineralogical studies also provide information on mineral classification, mode of formation and occurrence (Petruk, 2000). Information obtained from mineralogical studies allow for better planning, plant design and plant optimisation (Rule & Schouwstra, 2011).

2.7.1 Ore texture

Ore texture refers to the relationship between the minerals of which the rock is composed. It includes the size, shape, distribution and association of the mineral grains in the rock. The texture of an ore defines several factors that have a major influence throughout an operation, from mining strategy through to blending, processing, target grade and recovery, and tailings management. According to Cropp and Goodall (2013) some of these factors include:

- grain size distribution(s) and target grind size
- grindability of the ore

- degree of liberation of the target minerals
- phase specific surface area of the target minerals
- amount of fines
- number of coarse composite particles.

All textures, including crystallinity, grain boundary relations, grain orientations, fractures and veinlets have a bearing on processing ores. However, the sizes of the mineral grains and the bonding between the grains are the main characteristics that influence ore breakage and mineral liberation (Petruk, 2000).

2.7.2 Characterisation of ore bodies

Ore characteristics such as mineral identities, grain size, mineral associations, degree of liberation and the distribution of the minerals present can be determined from mineralogical studies. These characteristics can be explained by the relationship between minerals present in the ore (ore texture). Understanding the ore texture leads to identification of the minerals present in an ore body and their proportions. This is essential for the prediction of their response to various treatment processes and optimising the existing circuits (Schouwstra & Smit, 2011).

2.7.3 Common devices employed in process mineralogy

Many devices have been developed for determining mineralogical characteristics. The most common ones are:

- Optical microscope - It is used in the identification of many minerals, observing mineral textures and determining mineral quantities by point counting.
- X-ray diffractometer (XRD) – It is used to identify many minerals with a high degree of certainty, and to qualitatively determine mineral contents in powdered materials.
- Quantitative Evaluation of Minerals with Scanning Electron Microscopy (QEMSCAN) – It produces mineral maps (colour coded by mineral) which describe texture and mineral association in each sample. In addition to the coloured map, the output of the QEMSCAN measurement includes a quantitative measure of modal mineralogy, mineral grain size, mineral liberation and element deportment by mineral.

- Mineral Liberation Analyser (MLA) - It is an automated mineral analysis system that can quantify a wide range of mineral characteristics, such as mineral abundance, grain size and liberation.

2.8 Mineralogy of the Bushveld Complex ores

The Bushveld Complex is the largest known layered intrusion in the world (Clarke et al., 2005) which consists contains about 50 and 75% of the world's reserves of palladium and platinum respectively (Cawthorn, 1999). The layered intrusion consists of rocks which cooled slowly from molten magma, deep within the earth (Schouwstra et al., 2000). The Bushveld Complex consists of northern, western and eastern limbs (Cawthorn, 1999) as presented in Figure 2-15.

There are three distinct ore bodies within the Bushveld complex namely the Merensky reef, Upper Group 2 (UG2) reef and Platreef (Cramer, 2001). The total platinum group element (PGE) abundance of these reefs ranges between 4 and 10 g/t (Schouwstra et al., 2000). Merensky reef is the most abundant in PGM content followed by UG2 and then Platreef (Lee, 1996). Merensky and UG2 reefs outcrop on both the eastern and western limbs. Generally, UG2 lies below the Merensky reef by anywhere from 15 meters to 330 meters (Cramer, 2001). The northern limb of the Bushveld complex contains Platreef.

Merensky reef which is mainly pyroxenite rock type largely consists of the silicates, orthopyroxene (70 – 90%) and up to 30% of plagioclase (Xiao & Laplante, 2004). UG2 reef is made up of chromitite which consists predominantly of rounded chromite grains (60 to 90 percent by volume) cemented mainly by plagioclase (Schouwstra et al., 2000; Mathez & Mey, 2005). Platreef on the other hand consists of a complex assemblage of pyroxenites, serpentinites and calc-silicates (Schouwstra at al., 2000).

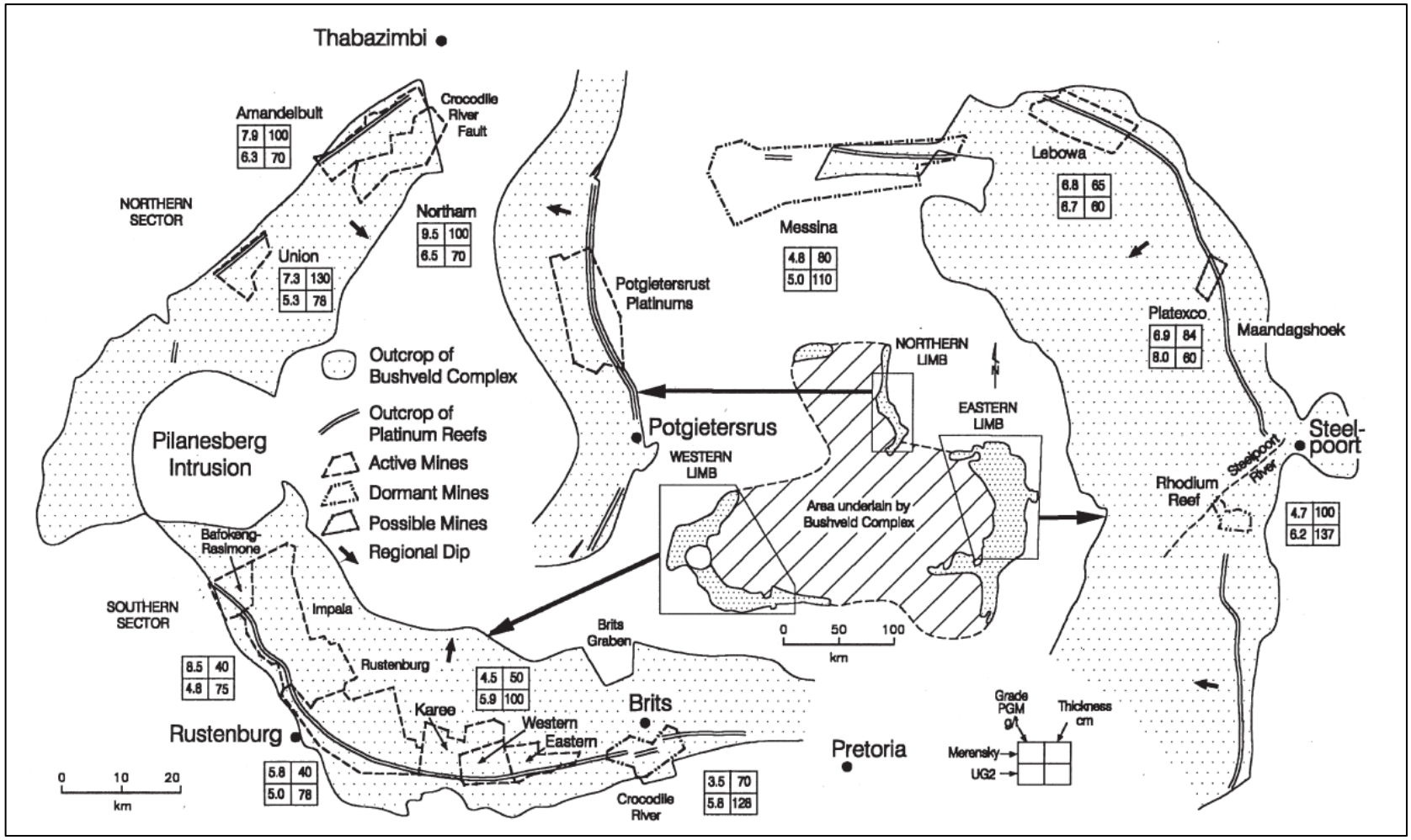

Figure 2-15: Map of the Bushveld Complex in South Africa (centre), showing the different mining operations in the northern, western and eastern limbs (exploded views) (Cawthorn, 1999)

Mainza and Powell (2006) investigated the breakage parameters of three platinum bearing ores namely UG2, Merensky and Platreef using the JK drop weight test in their work on RoM ball mills. The breakage parameters for the three platinum bearing ores obtained by Mainza and Powell (2006) are presented in Table 2-2.

Table 2-2: Typical breakage parameters for the main platinum ores from the Bushveld complex (Mainza & Powell, 2006)

Ore Type	Axb
UG2 Reef	151
Merensky Reef	77
Platreef	30-40

The breakage parameters from the drop weights indicate that the UG2 ore is the softest as shown by the largest value of the A×b of 151. Liddell et al (1986) pointed out that the UG2 reef is friable and it easily crumbles when a load is applied. Merensky was found to be harder than chromitite but softer than Platreef. Platreef ores were found to have the least A×b (30-40) indicating that it is the hardest.

The Merensky reef has been exploited since the late 1920s (Cramer, 2001). UG 2 reef mining started in 1983 (Liddell et al., 1986) but exploitation has accelerated to the point where at present, it has become the primary source of PGE production (Steyn, 2012; Cawthorn, 1999). Due to the increase in exploitation of UG2 reef, a lot of work have been done to get a better understanding of the mineralogy, texture and breakage properties (Liddell et al., 1986; Cramer, 2001; Penberthy, 2001; Steyn, 2012).

Figure 2-16 shows the structure of rock layers (stratigraphy) of Karee Mine in the Western limb of the Bushveld complex. The stratigraphy illustrates that the UG2 reef, which is a chromitite layer, is deeper than the Merensky reef as pointed out by Cramer (2001). UG2 chromitite consists mainly of rounded chromite grains (60 to 90 percent by volume) held together in a plagioclase matrix (Schouwstra et al., 2000; Mathez & Mey, 2005). In addition, Figure 2-16 shows that mining of the UG2 deposit which is done along the reef will result in the composition of the RoM ore consisting mainly of chromitite.

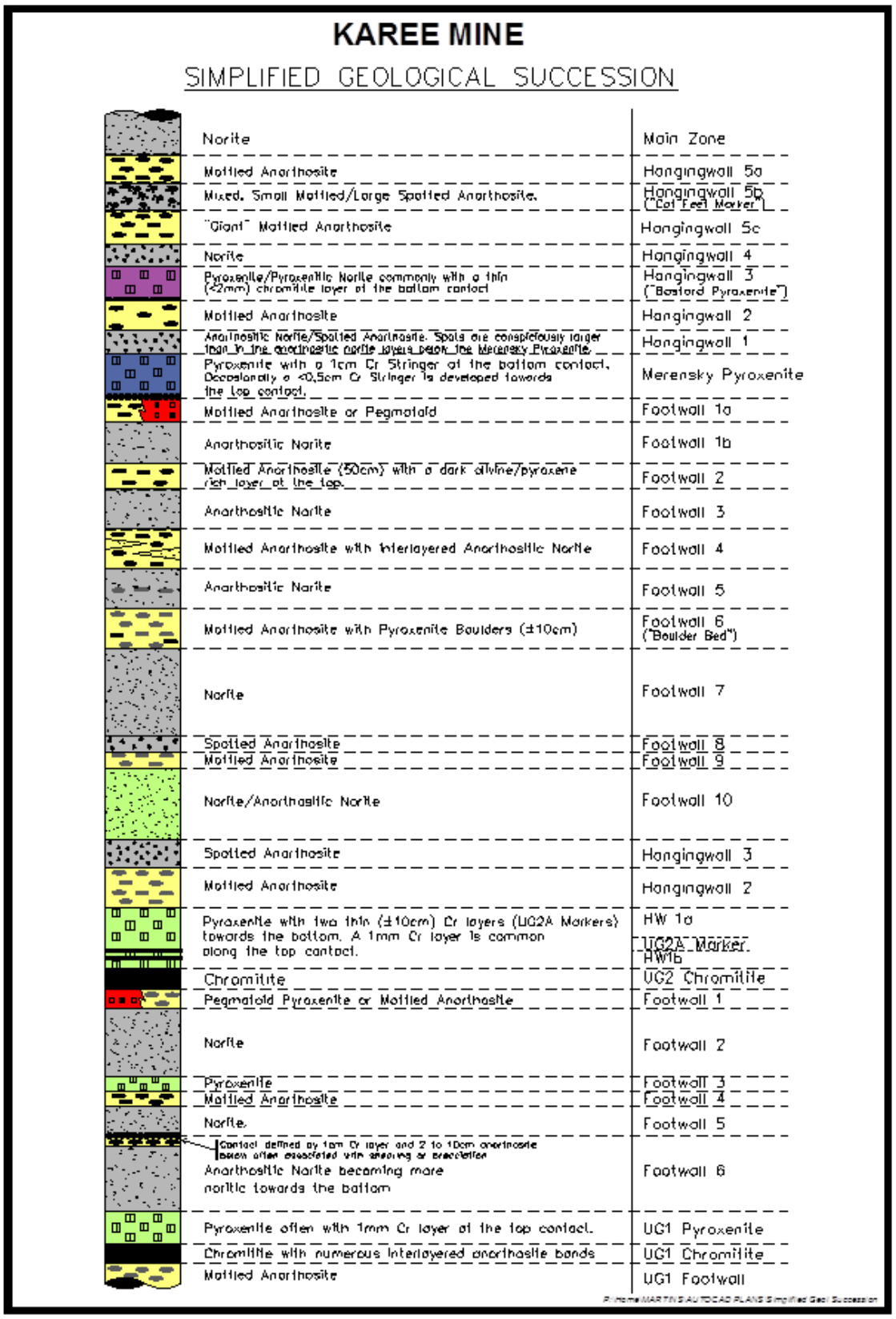

Figure 2-16: Stratigraphy of Karee mine in the Western limb of the Bushveld Complex

Other rock types that are likely to report to the stockpile include pyroxenite, norite, spotted anorthosite and mottled anorthosite. Pyroxenite consists of granular orthopyroxene, interstitial plagioclase and clinopyroxene (Mondal & Mathez, 2006). Norite is a mafic intrusive igneous rock composed largely of the calcium-rich plagioclase labradorite and hypersthene with olivine. Mottled anorthosite spotted anorthosite. Mottled and spotted anorthosite are coarse-grained igneous rocks consisting mainly of plagioclase feldspar (60 – 100%) with minimal orthopyroxene (0 – 30%) (Klerk, 1995; Ashwal, 1993). Orthopyroxene fills the interstices between the plagioclase crystals creating cumulus to poikilitic textures (Ashwal, 1993). In mottled anorthosite, the pyroxene mineral creates grey mottles giving a blotched appearance (Klerk, 1995). Spotted anorthosite has speckling of dark orthopyroxene minerals giving it a “spotted” appearance (Condie, 1992).

2.9 Summary of literature and hypothesis

The composition of run-of-mine ore strongly affects the target grind and energy consumption in the comminution circuits. One of the key factors influencing the performance that can be achieved with respect to each ore type in these devices is its hardness or resistance to breakage (Napier-Munn et al., 1996). In particular, RoM ore from the UG2 deposit contains different rock types namely chromitite, pyroxenite, norite, spotted and mottled anorthosite.

RoM ore particles have been reported to be exposed to pre-weakening during blasting and transportation to stockpile (Napier-Munn, 2014; Hahne et al. 2003). In addition, weathering of rock particles also occurs on the stockpile. These processes induce microflaws in the particles which act as stress raisers when the particle is under load (Tavares & King, 1998). The presence of cracks thus makes the particle less resistant to breakage and generates fine fragments (Schönert, 2004).

Therefore, it is hypothesized in the current study that:

- UG2 rock particles sourced from a run-of-mine ore stockpile break more readily to produce a finer product than cut drill core samples from the shaft supplying the same stockpile.

3. EXPERIMENTAL PROGRAMME

Overview

This chapter describes the approach used to meet the objectives of the project laid out in the introduction. A design of experiment to assess the effect of specific input energy and particle size on the product size distribution for a given ore type is discussed briefly. The sample preparation and impact breakage testing procedure using the rotary breakage tester are presented. Mineralogical analysis of the UG2 rock samples is also presented.

3.1 Introduction

The product size distribution resulting from impact breakage for a particular ore type depends on the specific input energy and particle size (Shi & Kojovic, 2007; Banini, 2000). The effect of these two factors on the particle size distribution was investigated to determine the impact breakage parameters.

There is a non-linear relationship between the degree of breakage measured by the percentage material passing 1/10th of the original feed size (t_{10} parameter) and specific input energy (Narayanan, 1985). As a result of the non-linear relationship, for a standard hardness characterisation test using a RBT, three energy levels (low, intermediate and high) were considered. In addition, four particles size classes from the standard breakage test using the RBT were used (named small, medium, large, and very (V.) large in this project). A design shown in Figure 3-1 permitted the testing of each particle size fraction at different input energy, as well as the effects of interactions between these two factors.

Particle size		Low	Intermediate	Large
Small	(-16.0 + 13.2 mm)	•	•	•
Medium	(-22.4 + 19.0 mm)	•	•	•
Large	(-31.5 + 26.5 mm)	•	•	•
V. Large	(-45.0 + 37.5 mm)	•	•	•

Figure 3-1: Schematic design for the impact breakage experiments

Figure 3-1 shows that a total of twelve experiments (without repeats) were done for a full analysis of the effect of specific input energy and particle size on the degree of breakage for each ore type.

3.2 Materials and sample preparation for RBT tests

The main equipment and apparatus that were required to carry out impact breakage tests are presented in this section. The sample preparation for the standard breakage tests for RBT installed at Lonmin Research and Design (R&D) labs at the Concentrators Technical Centre in Marikana are also briefly discussed.

3.2.1 Experimental apparatus

The main apparatus that were used to carry out the standard breakage characterisation tests are:

- JK Rotary Breakage Tester (RBT)
- Gilson sieve shaker with standard screens aperture sizes ranging from 13.2 mm to 45 mm.
- *Endecells D50* vibrating screen shaker
- Root 2 series of 200 mm diameter screens (aperture sizes ranges from 0.106 mm to 45 mm
- *Precisa BJ6100D* weighing scale
- Rotary divider
- Collecting trays and sample bags

Sample particles were subjected to breakage via impact in the RBT. Screens were used in sizing the particles in the preparation of samples and analysis of the products from the RBT. The rotary divider was used to randomly split the bulk samples into sets of particles required for the tests. The weighing scale was used to determine the mass of the particles.

3.2.2 Type of ores

Ore breakage characterisation tests were carried out on the platinum bearing Upper Ground 2 (UG2) ore, from the Bushveld complex in South Africa, mined by Lonmin Platinum. The ore was sourced from Karee 3 mine in the Marikana region of the North West province. The abundant rock types were grouped based on the visible physical characteristics such as colour, texture, grain size, or composition (lithology). The abundant rock types identified were:

- Chromitite
- Pyroxenite
- Mottled anorthosite
- Spotted Anorthosite

3.2.3 Sourcing the ore

Two methods were used to prepare the sets of particles used in the breakage tests namely particle selection and the cut core method.

(a) Particle selection method

Rock samples were collected from the Karee 3 UG2 Run-of-Mine (RoM) ore stockpile in Marikana as shown in Figure 3-2.

(a) (b)

Figure 3-2: Images showing (a) run-of-mine ore from Karee 3 UG2 mine being deposited on the stockpile (b) sample collection from Karee 3 stockpile.

Particles were selected based on the upper size limitation of the RBT (≤ 45 mm). The samples were then transported to the Lonmin R&D labs at the Concentrators Technical Centre for ore sorting and further sizing. Rock particles were sized using a

Gilson vibrating screen shaker shown in Figure 3-3 with standard sieve trays (45x37.5, 37.5x31.5, 31.5x26.5, 26.5x22.4, 22.4x19, 19x16, 16x13.2 and minus 13.2 mm).

Figure 3-3: Gilson vibrating screen shaker used in sizing of particle for breakage in the RBT

From these size classes, the fractions required for a standard breakage test were selected. The abundant rock types were grouped from each size class based on their lithology.

(b) Cut core method (CCM)

Drill cores from Karee 3 UG2 mine with diameter of 31 mm, were cut longitudinally into cylindrical pieces with lengths of 16 and 31 mm. The 16 mm cylindrical core slices were then quartered to give particles in the -16.0 + 13.2 mm size class shown in Figure 3-4 (a). Cylindrical pieces with lengths of 31 mm shown in Figure 3-4 (b) were then classified as -31.5 + 26.5 mm size class.

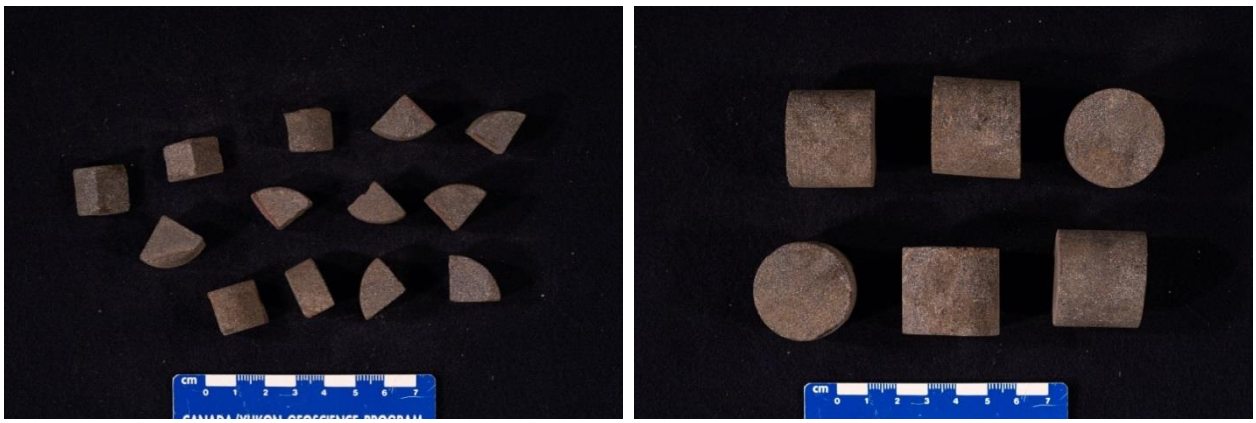

(a) (b)

Figure 3-4: Images of (a) -16.0 +13.2 mm and (b) -31.5 + 26.5 mm size classes for chromitite samples collected via the cut core method

3.2.4 Sizing particles for RBT tests

Four size classes were required for a standard test using the RBT. These size classes were named small (-16 + 13.2 mm), medium (-22.4 + 19 mm), large (-31.5 + 26.5 mm) and very large (-45 + 37.5 mm).

For a standard test, 3 sets of 30 particles for each size class were required. To ensure that samples were representative, a rotary divider in Figure 3-5 was used to randomly split the finer fractions (small and medium) into the splitter containers.

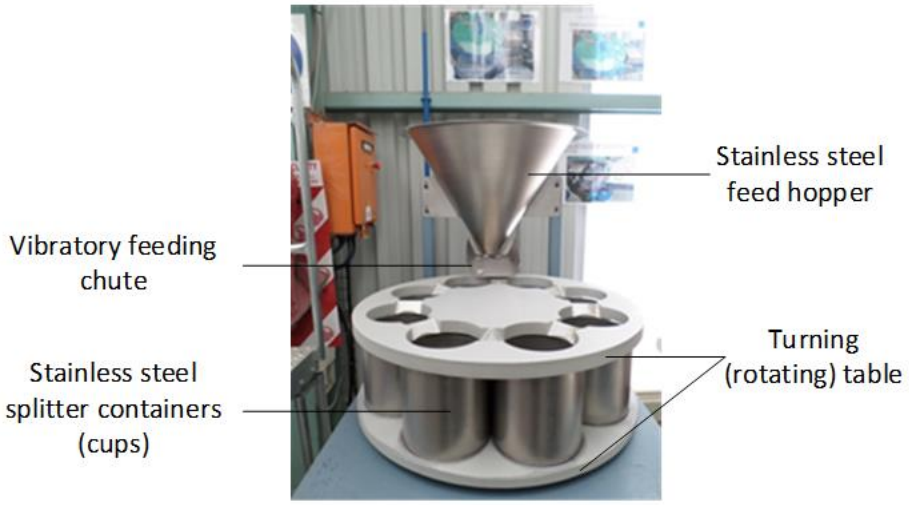

Figure 3-5: Rotary divider used to split particles

The bulk samples were fed into the feed hopper. The samples were channelled down the vibrating feed chute into different splitter containers on a rotating table shown in Figure 3-5.

The particles in the splitter containers were sub divided into sets of 30 particles for each size fraction as shown in Figure 3-6. The large and very large size fractions were randomly hand-picked into different sets because of the size limitation of the rotary splitter.

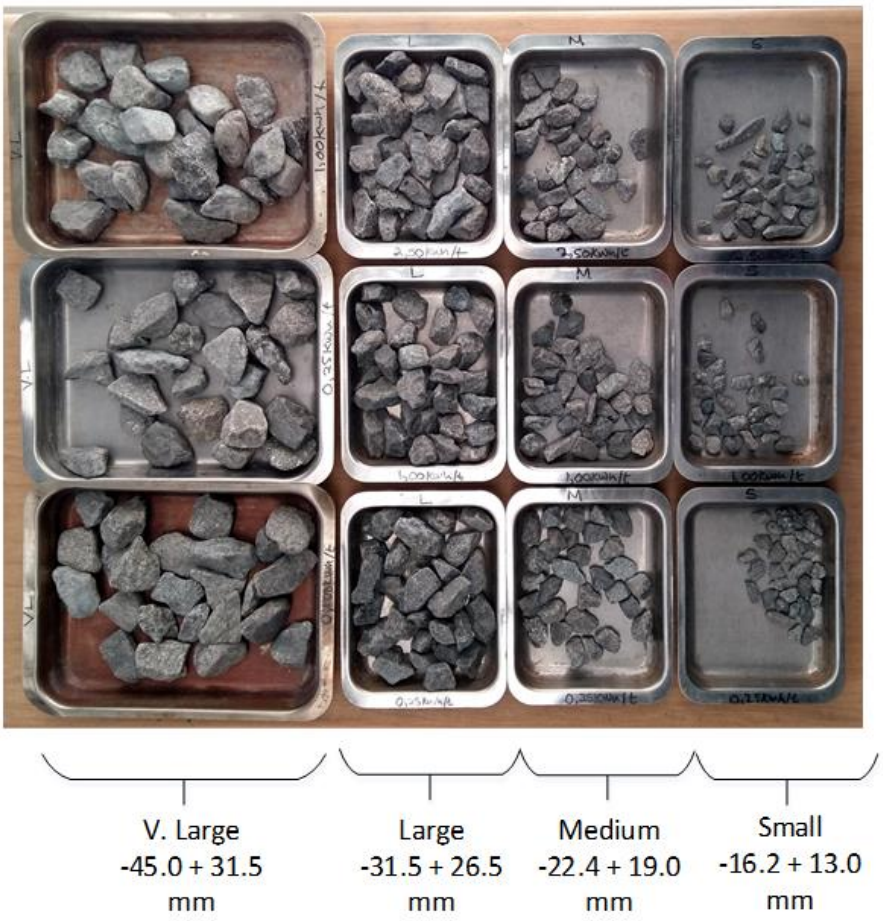

Figure 3-6: Trays containing sets of particles of different size fraction

To improve the statistical reliability of the results, repeat experiments were conducted depending on the availability of each rock type. In addition, even for the 30 particles per size-energy test used in the standard breakage experiments, the obtained results are statistically valid (Napier-Munn et al., 1996).

The sample preparation and testing procedure for impact breakage characterisation tests using the RBT are illustrated in Figure 3-7. The diagram shows all the steps from sourcing the rocks, ore preparation, sizing, conducting the impact breakage using the RBT and the product screening analysis. Some of the equipment, areas were data was captured and manual steps that were involved in the conducting the experiments are also colour coded.

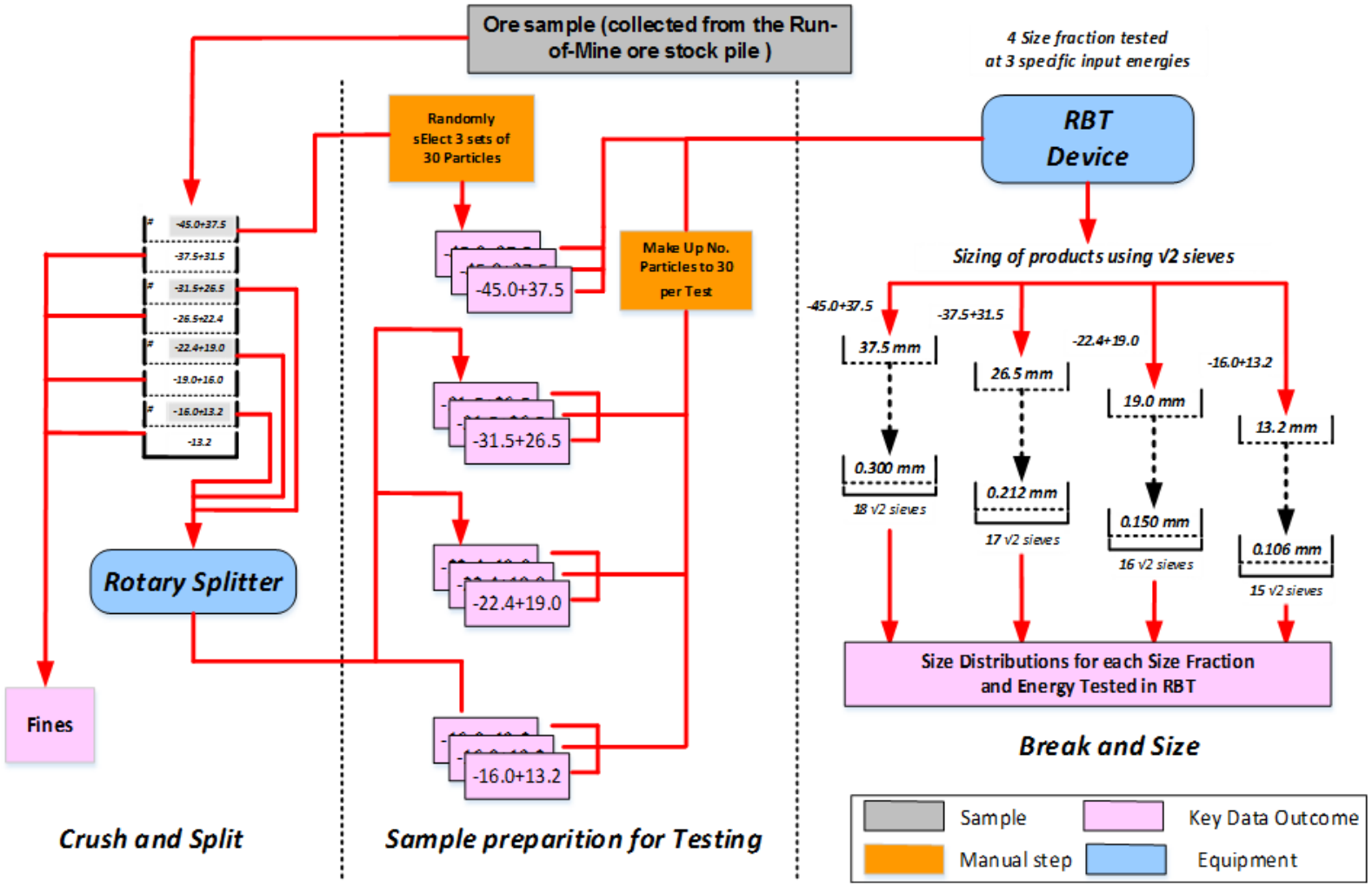

Figure 3-7: JK RBT sample preparation and testing protocol (adapted from JKMRC Rotary Breakage Tester, 2012)

3.3 Experimental Procedure

3.3.1 Single impact breakage tests using the RBT

The JK Rotary Breakage Tester (RBT) installed at the Lonmin Concentrators Technical Centre in Marikana that was used as an impacting device is shown in Figure 3-8.

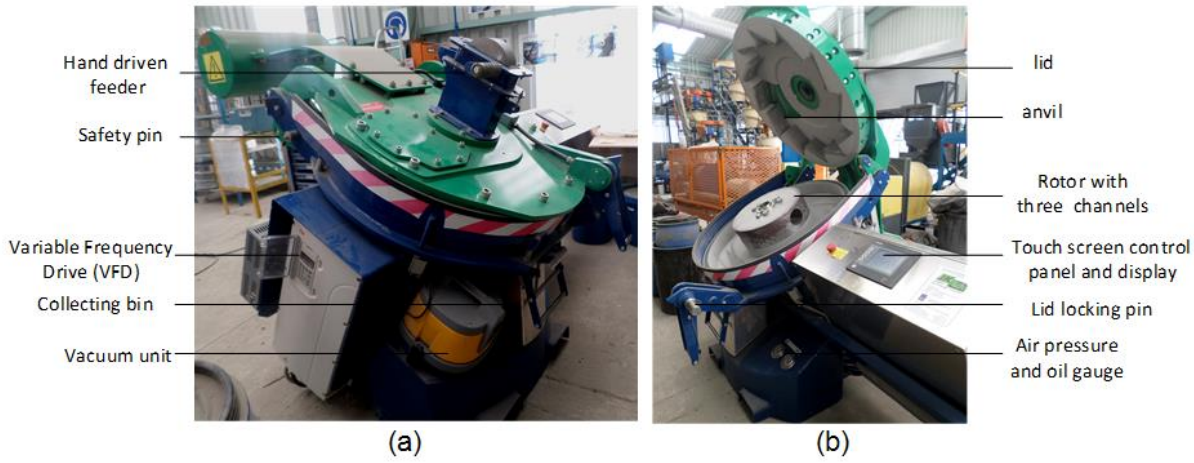

Figure 3-8: JK Rotary Breakage Tester (RBT) installed at the Lonmin Concentrators Technical Centre in Marikana with the lid in closed (a) and open (b) positions

Particles from each size class were subjected to impact breakage in the RBT at three energy levels as presented in the Table 3-1.

Table 3-1: Impact breakage tests at different energy levels

Size (mm)		Energy levels (kWh/t)				No. of particles per test	
						Particle Selection Method	Cut Core Method
Small	-16.0 + 13.2	×	0.25	1.00	2.5	30	30
Medium	-22.4 + 19.0	×	0.25	1.00	2.5	30	×
Large	-31.5 + 26.5	×	0.25	1.00	2.5	30	30
V. Large	-45.0 + 37.5	0.1	0.25	1.00	×	30	×

As presented in Table 3-1, 30 particles were required per test for each energy level. The energy levels are standard breakage energies identical to those used in Drop Weight Tests. Also these energies are usually above the energy for which a solitary impact would certainly cause breakage (Larbi-Bram, 2009).

(a) RBT operating procedure

The RBT was operated using the testing procedure from the JKMRC Rotary Breakage Tester machine manual. The key operating steps that were followed are as listed:

a) After the initial start-up procedure was completed, the oil level and air pressure were checked. The mist separators were drained of any moisture by pressing the discharge buttons on the side of the filters.

b) The desired rotor speeds or energies were set on the touch screen control panel shown in Figure 3-9 according to Table 3-2 by entering the desired energy input (in rpm or kWh/t) via the number pad.

Figure 3-9: Touch screen control panel for the JK RBT

Alternatively, the desired energy was set by pressing and holding 'Increase' or 'Decrease' until the required value was attained.

Table 3-2: RBT rotor speeds for standard breakage energies

Size Class mm	Required RPM for the target E_{cs} values			
	0.1 kWh/t	0.25 kWh/t	1.0 kWh/t	2.5 kWh/t
-45.0 + 37.5	938	1408	2606	-
-31.5 + 26.5	-	1408	2606	3915
-22.4 + 19.0	-	1408	2606	3915
-16.0 + 13.2	-	1408	2606	3915

c) After setting the desired speed, the start 'button' was pressed to accelerate the rotor. The light on the top of the RBT lid signalled when the rotor has stabilised at the required speed.

d) The pre-weighed samples were fed to the RBT at a rate of two particles per second at most using the hand driven feeder as shown in Figure 3-10. This ensured single particle impact breakage in the machine.

Figure 3-10: Operator feeding ore samples to the RBT through a hand driven feeder

e) After processing the sample, the stop “button” was pressed to bring the rotor to a halt. The vacuum pump automatically switched on when the flywheel reduces to below 1500 rpm to collect fines into the bin

f) The front lid of the RBT was raised after the rotor had stopped to access to the interior of the impact chamber. The remaining fragments from the anvil and around the flywheel were swept into the collection bucket to maximize recovery as illustrated in Figure 3-11.

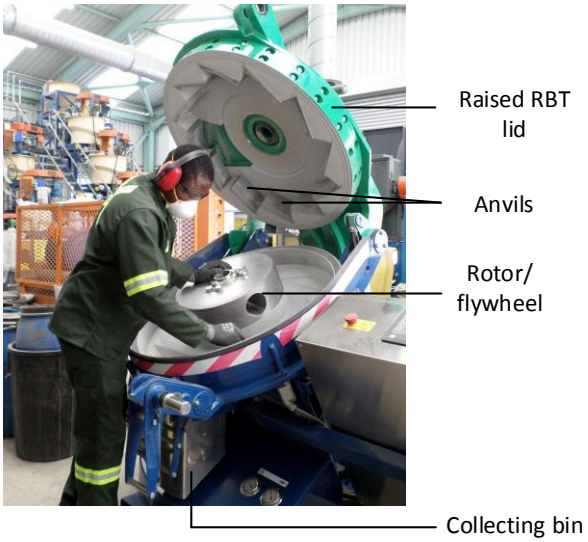

Figure 3-11: Brushing down the anvils, around the rotor into the collection bin

g) The collecting bin was emptied and the filters which trapped the fine materials were cleaned. The broken materials were passed on to the screening process.

3.3.2 Product Analysis: Screening

The breakage product of each test was collected and screened using standard root 2 series of screens (Napier-Munn et al., 1996). The screening procedure is summarised below.

a) The masses of the broken samples were recorded before screening.
b) The samples were dry screened using a *Endecells D50* vibrating screen shaker and a root 2 series of screen with the 0.106 mm being the smallest and 45.0 mm being largest, shown in Figure 3-12, for 10 minutes.

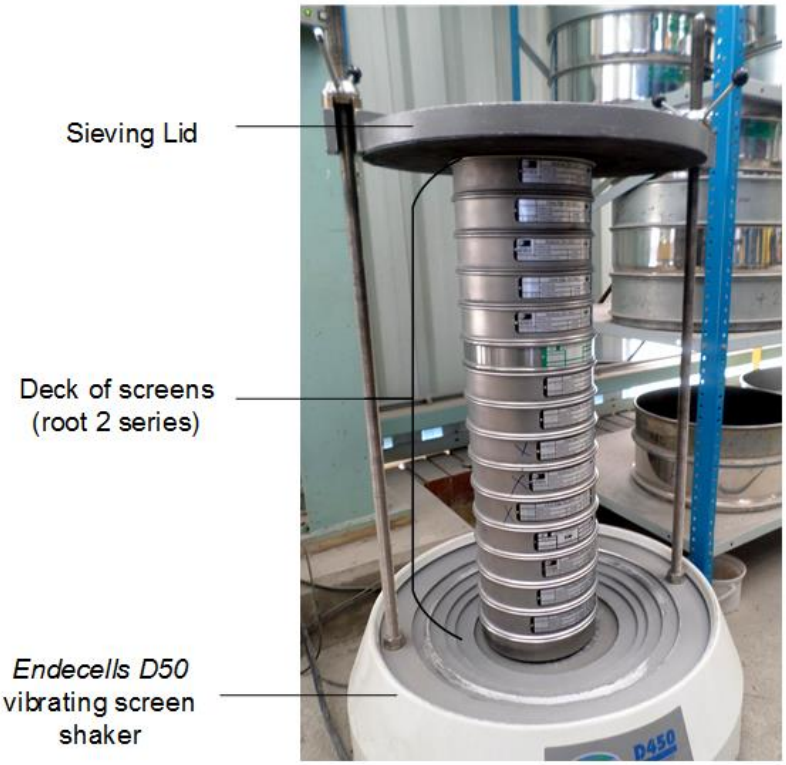

Figure 3-12: Endecells D50 vibrating sieve shaker packed with a deck of root 2 series of screens

c) The mass retained on each screen was recorded.

3.4 Mineralogical Analysis

Mineralogical analysis was performed to determine the texture and the mineralogical composition of the chromitite, pyroxenite, spotted anorthosite and mottled anorthosite specimens. Specimens were selected from the samples collected from the Karee 3 UG2 mine and were prepared according to the following procedure.

3.4.1 Sample preparation

1. Rock samples for UG2 chromitite, pyroxenite, spotted anorthosite and mottled anorthosite were prepared so that they fit into the 30 mm moulds and also ensuring that they are < 20 mm in height.

2. The moulds were labelled and lubricated. The individual samples were inserted into the moulds.

3. The moulds were placed in the Citovac under vacuum for 5 minutes before adding resin and for another 5 minutes. The resin was continuously added to the moulds to cover the rock samples.

4. The printed labels were added to the moulds which were then placed in the oven overnight to cure (30º C).

5. Once completely cured, the blocks were removed from the moulds for polishing. Polishing was done in a series of grinding and polishing steps until a 1 µm polish was achieved.

6. The samples were rinsed in the ultrasonic bath for approximately 10 minutes. A generous squirt of ethanol was then used for the rinsing with much caution being taken to avoid scratching the surface.

7. The samples were dried in the oven (30º C) for a minimum of 1 hr.

8. The quality of the final polish was checked using an optical microscope ensuring that there are no plucked grains, large differences in relief, cracked or grungy looking grains on the sample surface.

9. The samples were carbon-coated using the Emitech carbon evaporator to diffuse electrons off the surface of the sample when they are in the QEMSCAN.

3.4.2 Optical microscope

Polished moulds were examined under the Leica EZ4D microscope presented in Figure 3-13 to identify the major ore minerals and their association.

Figure 3-13: Leica EZ4 D optical microscope

Observations were made with a reflected light. The integrated digital camera on the Leica EZ4 D microscope offers a live video on a computer screen. Colour images of the samples were captured and saved onto the computer.

3.4.3 QEMSCAN Analysis

The Quantitative Evaluation of Minerals by Scanning electron microscopy (QEMSCAN 650F) shown in Figure 3-14 (a) was used to generate detailed mineral maps or false colour, field-scan image (field images) of the different rock samples. These field scans detail the mineralogical texture and modal mineral abundances of the rock samples.

QEMSCAN uses a mineral library system, called Species Identification Protocol (SIP). The SIP determines how the elemental information measured by the SEM scanning a sample, is classified into a mineralogical composition or species. The SIP consists of a list of entries (SIP definitions), each with a set of user-specified criteria to match the X-ray spectra and BSE (Back Scatter Electron) data from a measurement point to a mineral species. As each point on a sample is scanned, its spectrum is converted to element information which is compared to the entries in the SIP list until one is found with parameters matching the scanned material.

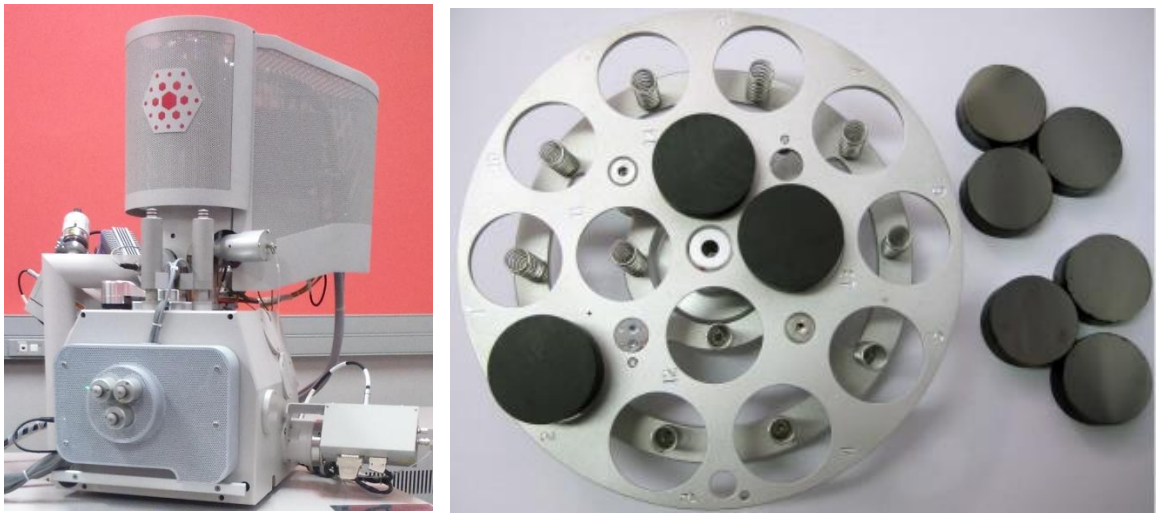

(a) (b)

Figure 3-14: (a) QEMSCAN 650F installed at the University of Cape Town (UCT) (b) Sample block holder with 30 mm sample disks

The QEMSCAN tests were performed at UCT. Mounts of the samples were placed in the samples chamber for analysis. The scanning parameters are summarized in Table 3-3.

Table 3-3: Scanning parameters for the mineralogical analysis using the QEMSCAN

Type	FEG QEMSCAN 650 F
Voltage	25 kV
Beam Current	10 nA
Field size	1500
FEG Steps	25 microns

3.4.4 X-ray computed tomography (XCT) analysis

The XCT analysis was conducted on the -16.0 + 13.2 mm and -31.5 + 26.5 mm size fractions for the UG2 chromitite RoM ore stockpile particles and cut drill core samples. The Nikon XTH 225 ST micro-focus X-ray system installed at the micro-focus X-ray radiography and tomography (MIXRAD) facility situated at the South African Nuclear Energy Corporation (Necsa) presented in Figure 3-15 was used for the analysis.

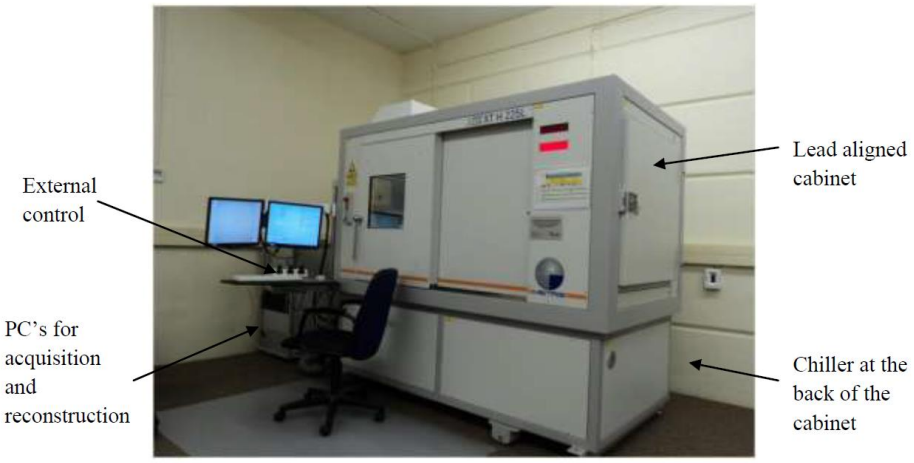

Figure 3-15: Micro-focus X-ray machine at the MIXRAD facility at Necsa (Hoffman & Beer, 2011)

An illustration of the tomographic process displaying basic layout of the XCT system is shown in Figure 3-16.

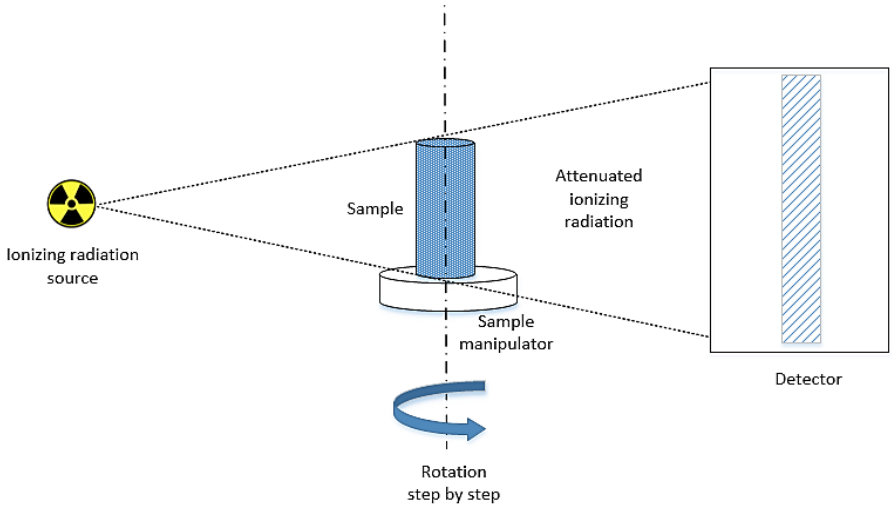

Figure 3-16: The basic layout of the XCT system

A sample is fixed on the manipulator between the X-ray source and a detector to ensure no movement of the sample occurs during scanning as shown in Figure 3-16. X-rays pass through the sample as it rotates about a single axis. The X-rays passing through the sample are partially attenuated. The attenuated X-rays are captured at the detector from each angle of rotation to form an image/radiograph. The collected images are then reconstructed to form a 3D digital copy of the sample to be analysed or quantified.

The UG2 chromitite particles were scanned using the parameters summarised in Table 3-4.

Table 3-4: Experimental conditions used for XCT measurements

Voltage	140 kV
Current	100 µA
Exposure time	2 seconds
Number of frames	1000 images
Resolution/pixel size	20 µm

4. RESULTS AND DISCUSSION

Overview

This chapter presents and discusses the results obtained from the experimental work performed to meet the objectives of this study. The breakage properties of different rock types from the UG2 ore deposit obtained from the Marikana region in the North West Province in South Africa were determined using the RBT as a characterisation device.

4.1 Introduction

As summarized in section 3.2, run-of-mine (RoM) ore and drill core samples were sourced from Karee 3 (K3) UG2 shaft mined by Lonmin Platinum in the Marikana region. The RoM samples were screened into four size classes required for a standard breakage test using the RBT namely; -16 + 13.2 mm, -22.4 + 19 mm, -31.5 + 26.5 mm and -45 + 37.5 mm. In this thesis, these size classes were named small, medium, large and very large respectively. The available drill cores of diameter 30 mm were cut into small and large particles.

Four main rock types namely; chromitite, pyroxenite, spotted anorthosite and mottled anorthosite, were identified from the samples based on visible physical characteristics such as colour, texture, grain size and composition. The mineralogical analysis of each of these rock types was conducted using an optical microscope and a QEMSCAN. This was done to establish a link between the mineralogical properties of the rocks and their breakage properties.

To determine breakage characteristics of the main rock types sourced from UG2 ore deposit, particles from each size class were subjected to impact breakage using the RBT. Three energy levels were used as required for a standard breakage test described in the previous chapter. For each full breakage characterization test, 12 product samples were thus generated. The effects of energy input on the progeny particles were explored. The progeny particle size distribution and degree of breakage attained for each rock type for a particular size class and specific energy input are presented and discussed. An evaluation of energy-size relationships of each rock type and breakage parameters obtained from fitting the standard hardness characterisation models are presented in this chapter.

4.2 Mineralogical analysis of the rock tested

Mineralogical analysis was performed for each of the main rock types identified in the UG2 ore sourced for the experimental work. The main rock types found includes chromitite, pyroxenite, spotted anorthosite and mottled anorthosite. Specimens of each rock type were analysed using a Leica EZ4D optical microscope and QEMSCAN 650F to determine the texture and mineralogical composition. Results from the mineralogical analysis are presented in the subsequent sections.

4.2.1 UG2 Chromitite

Chromitite is the most abundant rock type in UG2 ore. The texture of UG2 chromitite specimen tested in this work is illustrated in Figure 4-1. The analysed UG2 chromitite consists predominantly of fine, discrete, rounded chromite (black) grains cemented by plagioclase as shown in Figure 4-1 (a). This is in line with the findings reported by Schouwstra et al (2000) and Mathez and Mey (2005). Figure 4-1 (b) shows the composition of the chromitite specimen which mainly contained chromite and significant amounts of plagioclase and orthopyroxene.

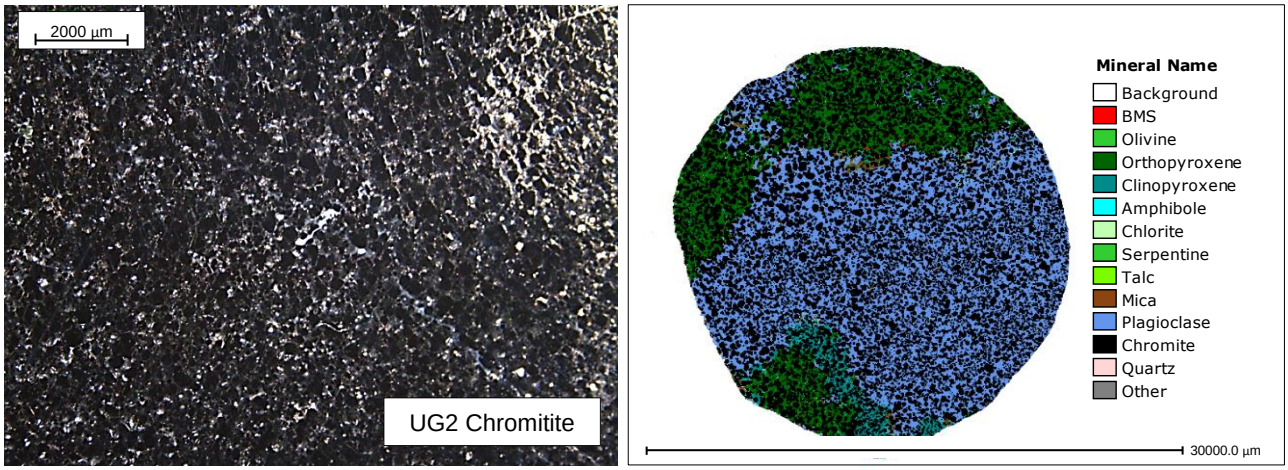

(a) (b)

Figure 4-1: Optical microscope (a) and QEMSCAN false colour images (b) for a UG2 chromitite

The bulk mineralogical analysis which shows the relative abundance of minerals present in the chromitite specimen determined using a QEMSCAN is presented in Figure 4-2. The analysis showed that the specimen contained 65.8 wt. % chromite, 20.3 wt. % plagioclase and 10.9 wt. % orthopyroxene and 1.58 wt. % clinopyroxene. Schouwstra et al (2000) reported that the chromite content in UG2 chromitite varies

between 60 and 90 wt. %. The chromite content of 65.8 wt.% found in this study is within the reported range by Schouwstra et al (2000).

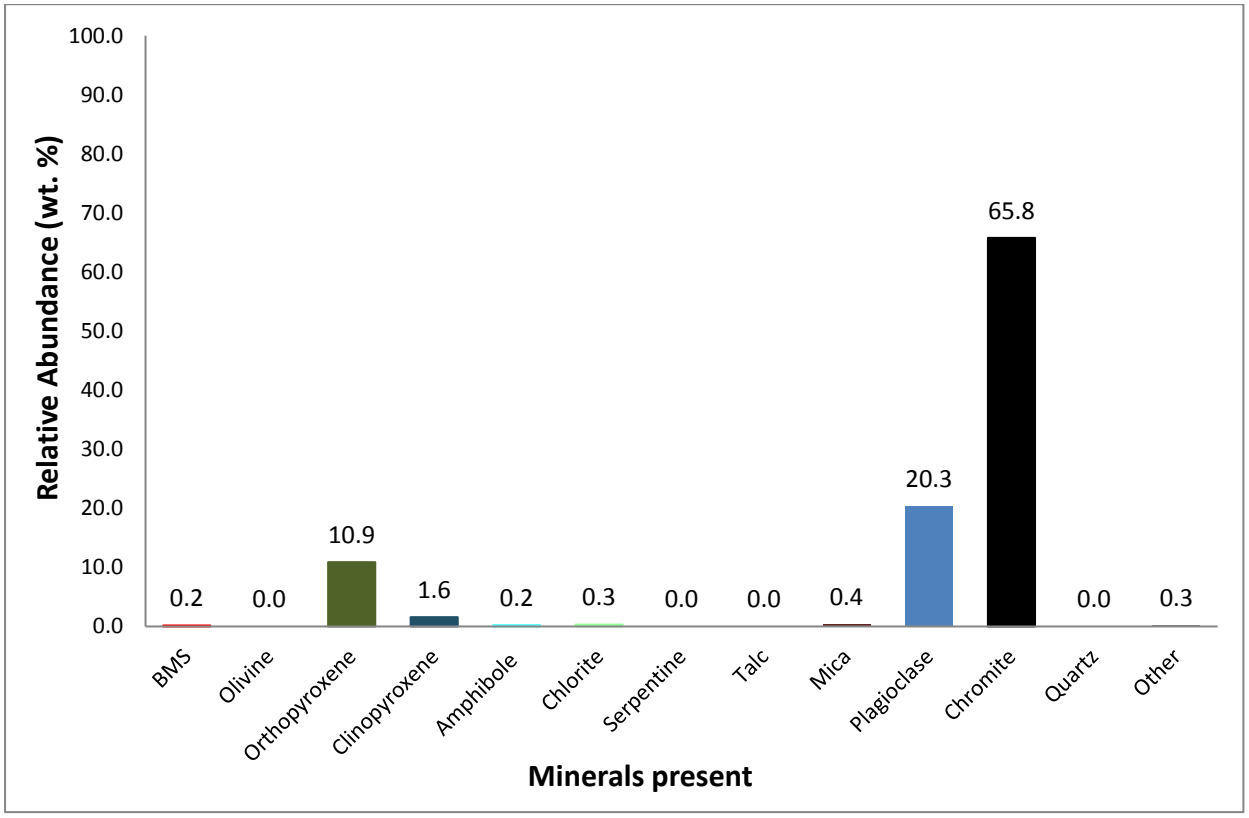

Figure 4-2: Bulk mineralogy of a UG2 chromitite specimen

4.2.2 UG2 Pyroxenite

Pyroxenite is one of the rock types that is found in UG2 ore. Figure 4-3 shows the texture of a UG2 pyroxenite specimen from K3 UG2 shaft. UG2 pyroxenite specimen analysed was found to contain predominantly granular orthopyroxene, interstitial plagioclase and clinopyroxene as presented in Figure 4-3. Similar texture of UG2 pyroxenite was reported by Mathez and Mey (2005). The orthopyroxene grains in Figure 4-3 (b) were found to be relatively larger than the chromite grains in chromitite particles shown in Figure 4-1 (b).

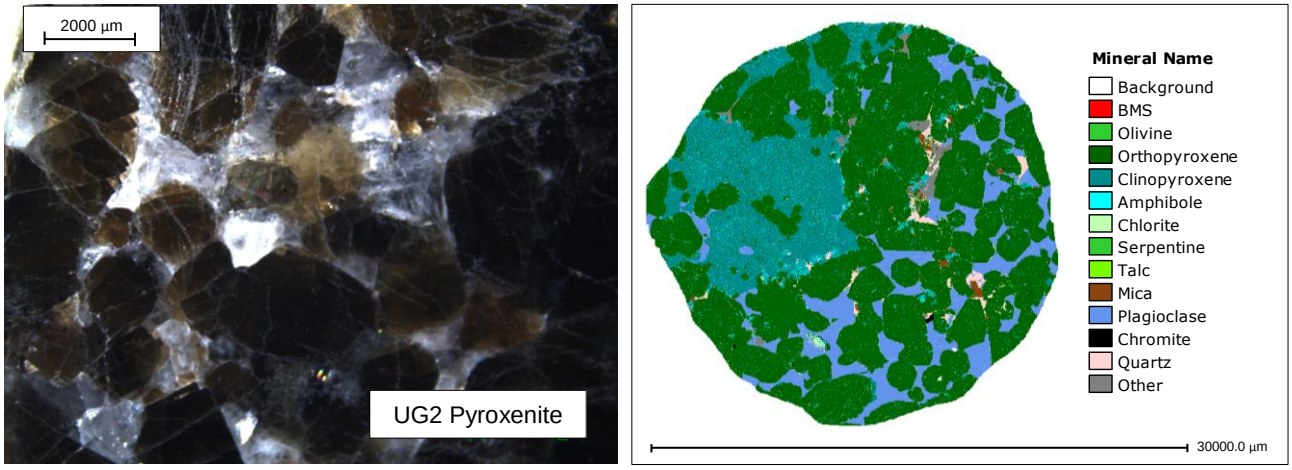

(a) (b)

Figure 4-3: Optical microscope (a) and QEMSCAN false colour images (b) for a UG2 pyroxenite

The relative abundance of minerals present in the UG2 pyroxenite specimen were determined using a QEMSCAN. It was found that pyroxenite contained primarily orthopyroxene, clinopyroxene and plagioclase in the proportions presented in Figure 4-4. The UG2 pyroxenite specimen tested consisted of large amounts (67.5 wt. %) of orthopyroxene as highlighted in Figure 4-4. The specimen also contained significant amounts of clinopyroxene and plagioclase with relative amounts of 18.0 wt. % and 9.3 wt. % respectively. Other species were in relatively insignificant amounts.

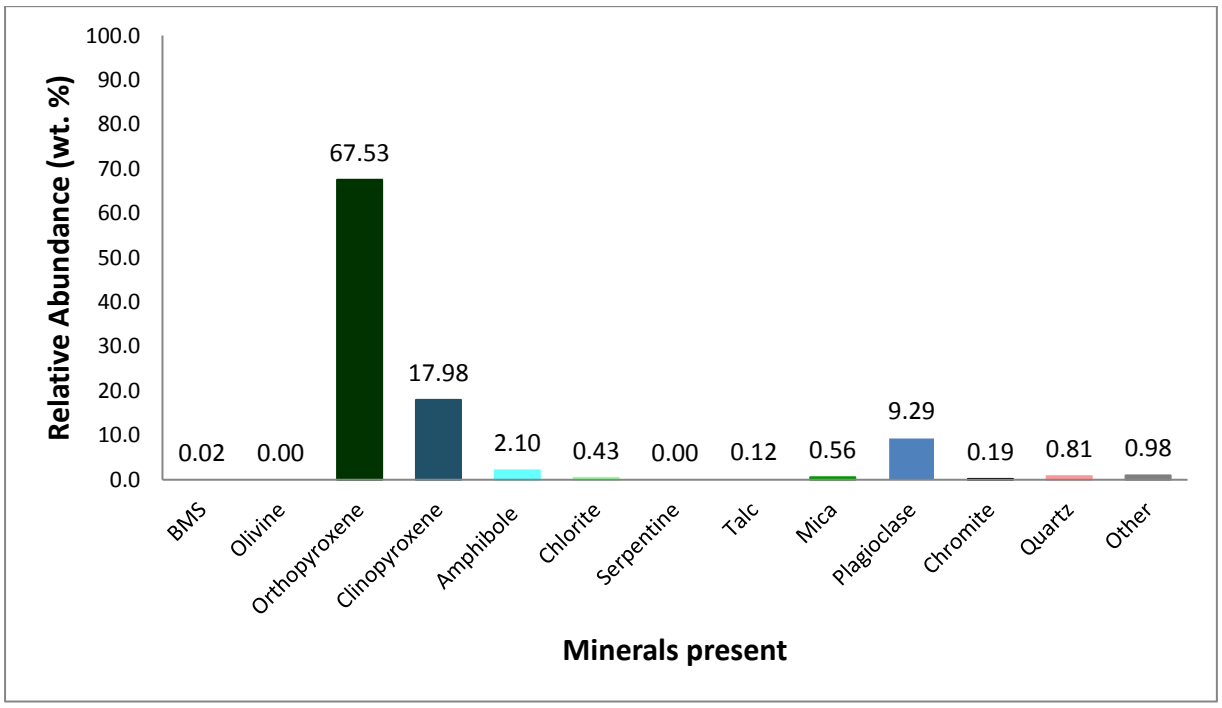

Figure 4-4: Bulk mineralogy of a UG2 pyroxenite specimen

4.2.3 UG2 Spotted Anorthosite

One of the rock types that was found in UG2 ore sourced from Karee 3 shaft was spotted anorthosite. The optical microscopic observations and QEMSCAN scans for UG2 spotted anorthosite specimen are presented in Figure 4-5. UG2 spotted anorthosite specimen was found to contain mainly plagioclase, which is the glassy material revealed in the optical microscope observations in Figure 4-5 (a). Orthopyroxene crystals form isolated interstitial "spots" within the plagioclase creating a poikilitic texture clearly displayed in the QEMSCAN false colour image in Figure 4-5 (b). As similarly pointed out by Condie (1992), spotted anorthosite has speckling of dark orthopyroxene minerals thus the "spotted" appearance. The anorthosite specimen was also found to be coarse grained due to individual plagioclase crystals which are a few centimetres long (shown in Figure 4-5 (a)) just as pointed out by Klerk (1995) and Ashwal (1993).

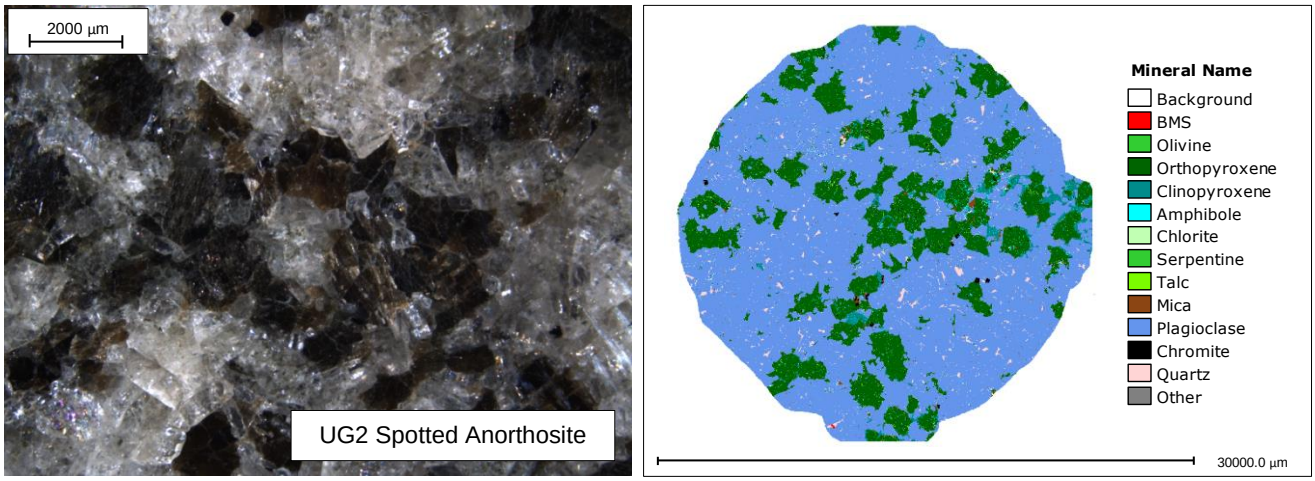

(a) (b)

Figure 4-5: Optical microscope (a) and QEMSCAN false colour images (b) for a UG2 spotted anorthosite

The bulk mineralogy of the spotted anorthosite specimen determined using a QEMSCAN is presented in Figure 4-6. UG2 spotted anorthosite specimen predominantly contained plagioclase and orthopyroxene with relative abundances of 66.6 wt.% and 26.95 wt.% respectively as shown in Figure 4-6. The relative abundances of plagioclase and orthopyroxene fall in the ranges of 60 to 100% and 0 to 30% respectively reported by Klerk (1995) and Ashwal (1993).

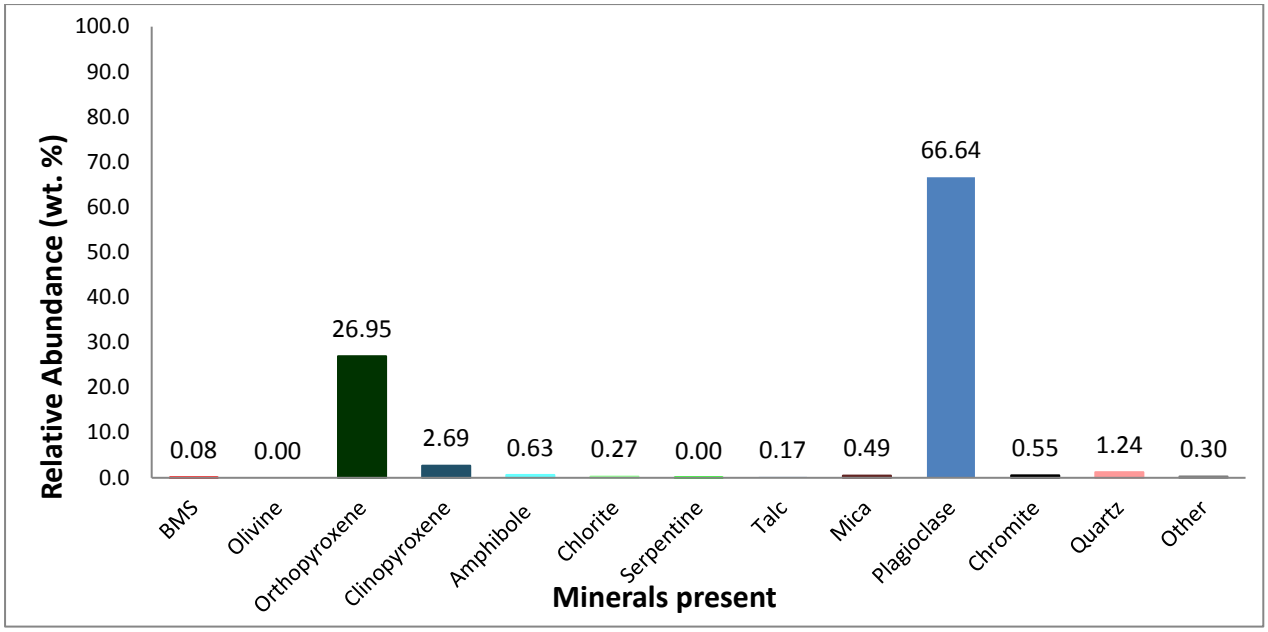

Figure 4-6: Bulk mineralogy of a UG2 spotted anorthosite specimen

4.2.4 UG2 Mottled Anorthosite

Mottled anorthosite is another abundant rock type that was found in UG2 ore. The texture of the UG2 mottled anorthosite specimen tested is illustrated in the optical microscopic and QEMSCAN false colour images in Figure 4-7. UG2 mottled anorthosite is dominated by plagioclase Figure 4-7 (b). Klerk (1995) found that in mottled anorthosite, pyroxene minerals create grey mottles giving a blotched appearance. However, the specimen tested did not display the blotched appearance as described by Klerk (1995) because of negligible amounts of the pyroxene minerals.

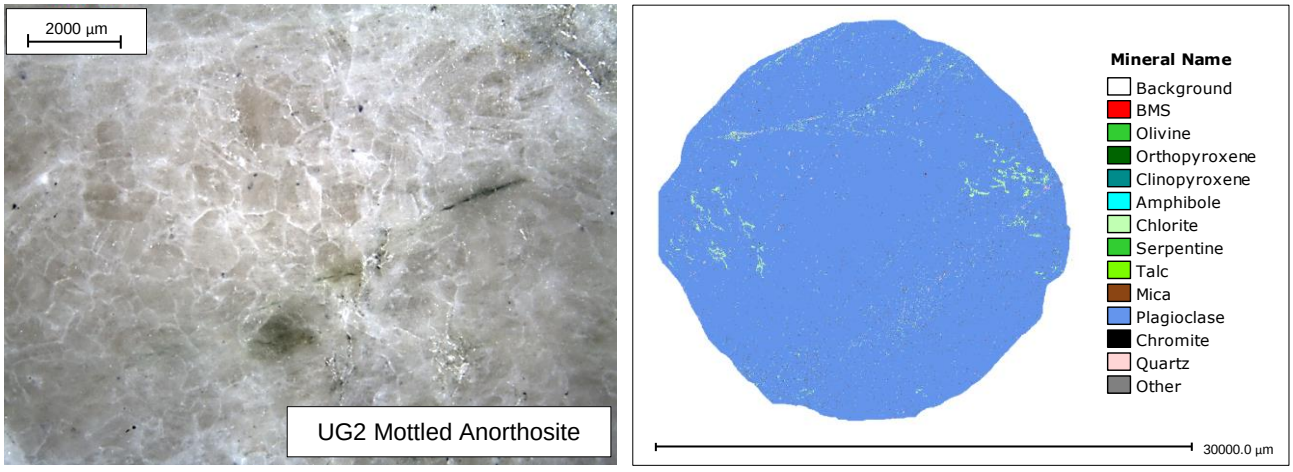

(a) (b)

Figure 4-7: Optical microscope (a) and QEMSCAN false colour images (b) for a UG2 mottled anorthosite

The bulk mineralogical analysis using a QEMSCAN showed that the specimen tested was composed of 96.6 wt. % of plagioclase as presented in Figure 4-8. Klerk (1995) reported that mottled anorthosite consist mainly plagioclase feldspar (60 – 100%). The plagioclase content found in this study is within the reported range by Klerk (1995).

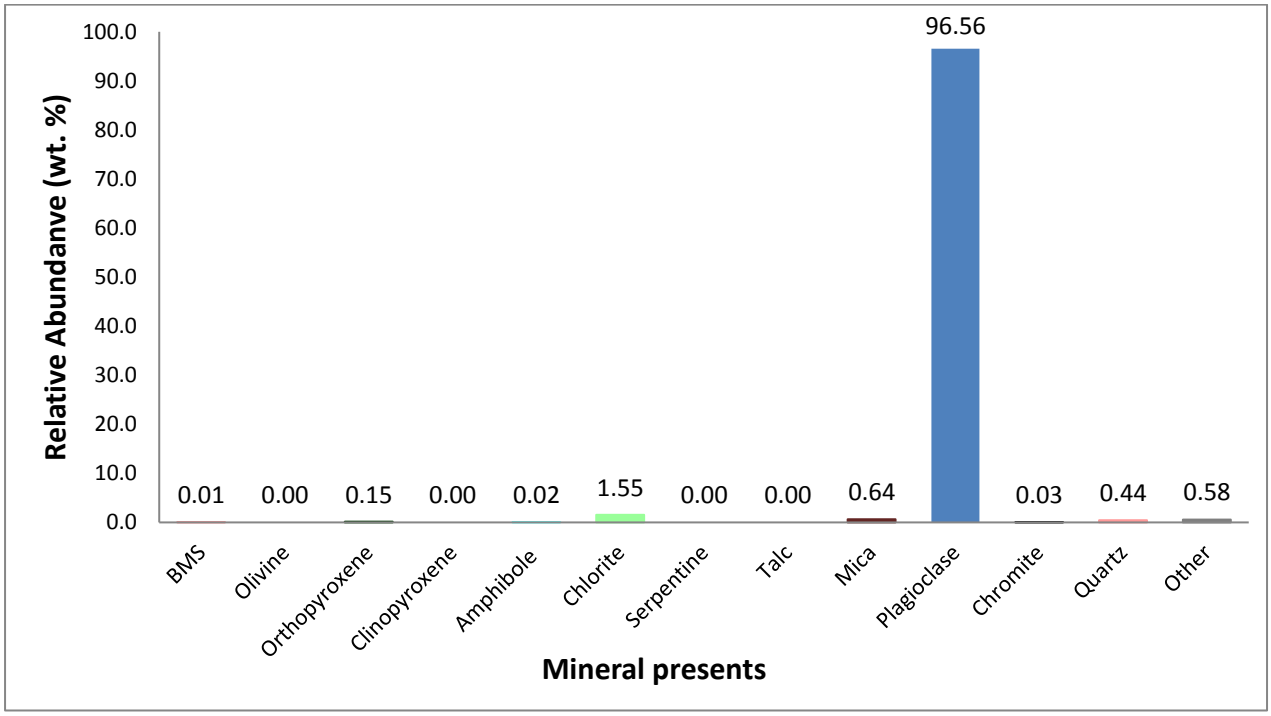

Figure 4-8: Bulk mineralogy of a UG2 mottled anorthosite specimen

It has been pointed out by many authors (Schouwstra & Smit, 2011; Petruk, 2000; Napier-Munn et al., 1996) that the mineral composition and texture strongly affects the breakage properties of a given rock type. The findings from the mineralogical analysis will be useful in explaining the exhibited breakage characteristics presented in the following sections.

4.3 Progeny particles

The selected rock types discussed in section 4.2 of various feed sizes were subjected to impact breakage using the RBT at three energy levels. Progeny particles were examined visually to assess the extent of damage caused to the particles by single impact. Photographs of the parent and progeny particles of UG2 chromitite sourced from K3 stockpile are presented in Figure 4-9 (a) and (b) respectively. It can be seen from Figure 4-9 that for each size class, the progeny particles become finer with increase in the specific input energy.

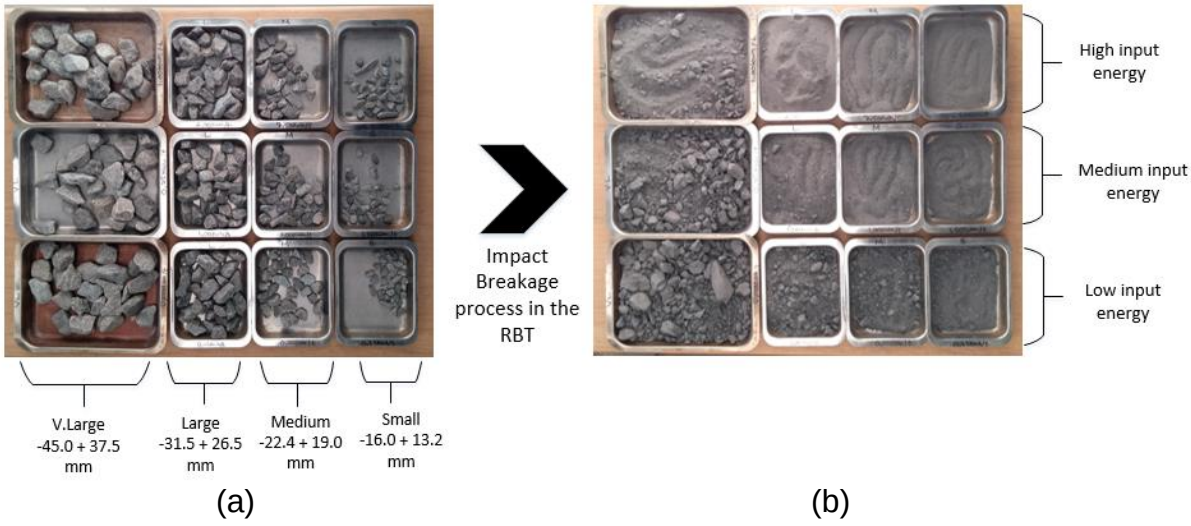

Figure 4-9: Parent (a) and progeny (b) particles of UG2 chromitite

The trend exhibited in Figure 4-9 is well pronounced by the particle size distributions of the RBT progeny particles presented in the following section. The progeny particle size distributions were also used to compare the breakage charcteristics of samples obtained from the RoM stock pile and cut drill core particles as well as evaluating the main rock types identified in the Karee 3 UG2 ore.

4.4 Progeny particle size distributions

For each breakage test performed, particle size distributions of the progeny fragments were obtained and used to assess the damage achieved after each primary fracture in the RBT. The progeny particle size distributions were plotted in the form of cumulative material passing a given particle size.

The initial assessment involved comparing the progeny particle size distributions obtained from the two different sampling methods employed in this study. An evaluation of the progeny particle size distributions of the main rock types identified in

the UG2 ore collected was also performed. The main rock types found includes chromitite, pyroxenite, spotted anorthosite and mottled anorthosite. The effect of input energy on progeny particle size distributions was also assessed.

4.4.1 Progeny particle size distribution for particle selection method (PSM) and cut core method (CCM)

A comparison of the progeny particle size distributions obtained for grab samples from RoM ore (particle selection method) and cut drill core particles (cut core method) subjected to single impact breakage was done. The comparison was done for small (-16.0 + 13.2 mm) and large (-31.5 + 26.5 mm) particles due to the availability of cut drill core particles only in these size fractions. Due to limited samples of cut drill core particles, no test was performed for the large size class of UG2 chromitite at 2.50 kWh/t. Figure 4-10 and 4-11 show the particle size distributions of the progeny fragments at three energy input levels for UG2 chromitite and pyroxenite respectively.

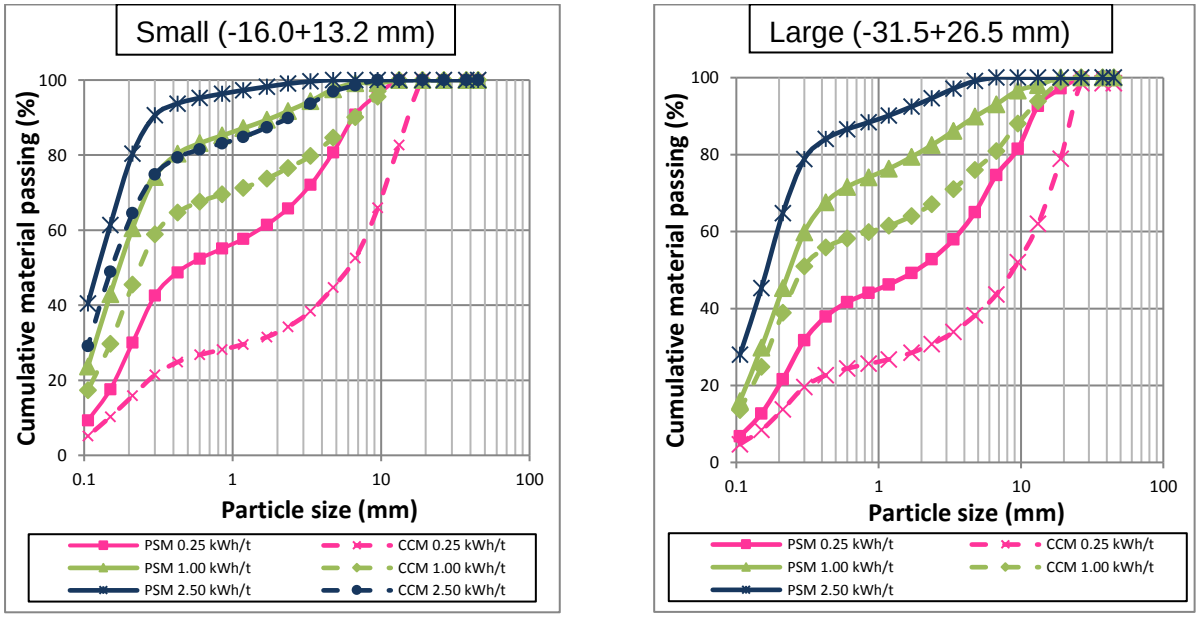

Figure 4-10: Progeny particle size distributions for small (-16.0 + 13.2 mm) and large (-31.5 + 26.5 mm) UG2 chromitite

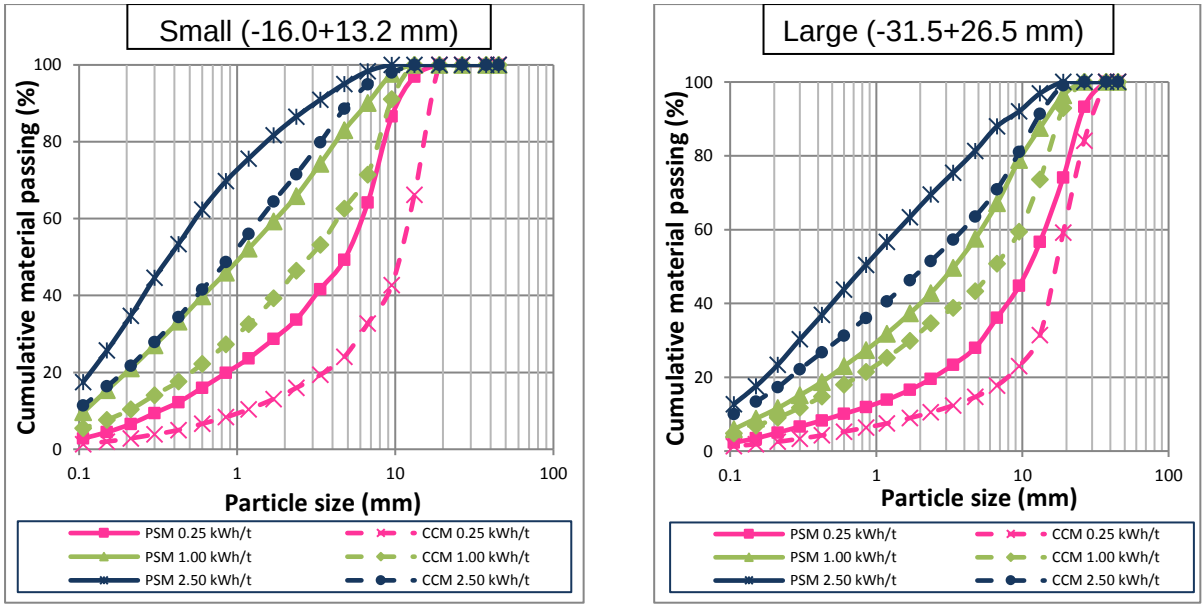

Figure 4-11: Progeny particle size distributions for small (-16.0 + 13.2 mm) and large (-31.5 + 26.5 mm) UG2 pyroxenite

As illustrated in Figure 4-10 and 4-11, for the same rock type, size class and input energy, the progeny particle size distributions from RoM ore samples were consistently finer than that from cut drill core particles. The observed trend was similar for all rock types tested. The results for spotted and mottled anorthosite are given in Appendix C. RoM ore particles are exposed to pre-weakening during blasting and transportation to stockpile. These pre-weakening processes induce flaws in the particles. As illustrated by Ashby, Shercliff and Cebon (2007) in Figure 2-2, the presence of cracks act as sites for stress concentration (stress raisers) when the particle is under load. The stress at a crack tip is proportional to the square root of the crack length perpendicular to the stress direction (Inglis, 1913). Thus, for the stockpile particles, a smaller amount of energy is sufficient to break the atomic bond at the crack tip. Such rupture of the bond will increase the crack length, thus increasing the stress concentration and causing a rapid propagation of the crack through the material, resulting in a catastrophic fracture (Wills & Napier-Munn, 2006).

X-ray computed tomography (XCT) analysis was done to investigate the presence of cracks in RoM stock pile particles and cut drill core samples. Tomography scans for the large (-31.5 + 26.5 mm) and small (-16.5 +13.2 mm) UG2 chromitite particles randomly selected from the RoM and cut core samples are presented in Figure 4-12 to 4-15.

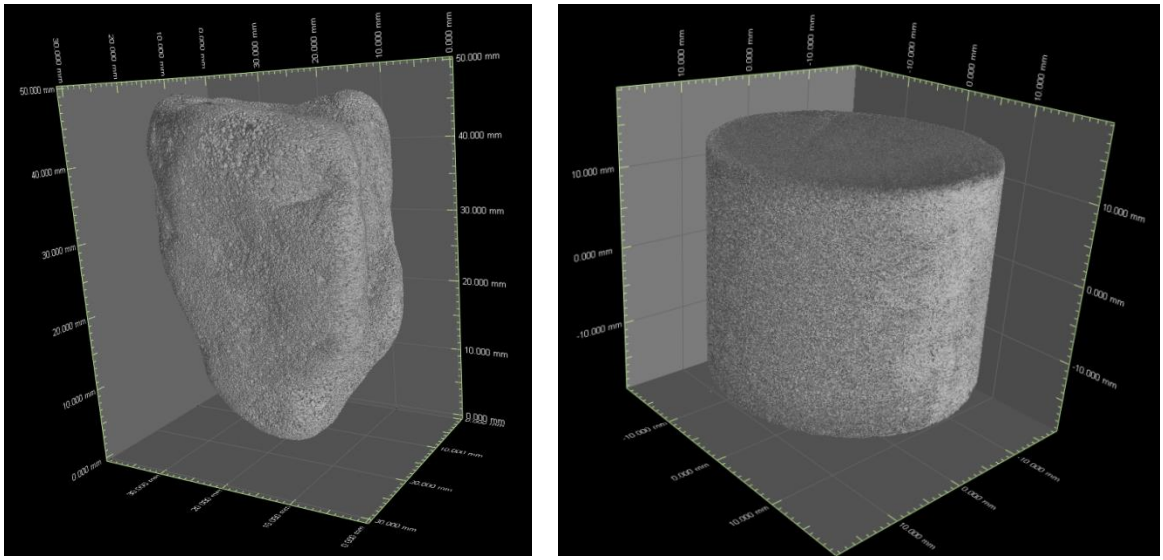

(a) (b)

Figure 4-12: 3D tomography images for (a) RoM and (b) cut drill core UG2 chromitite -31.5 + 26.5 mm specimens

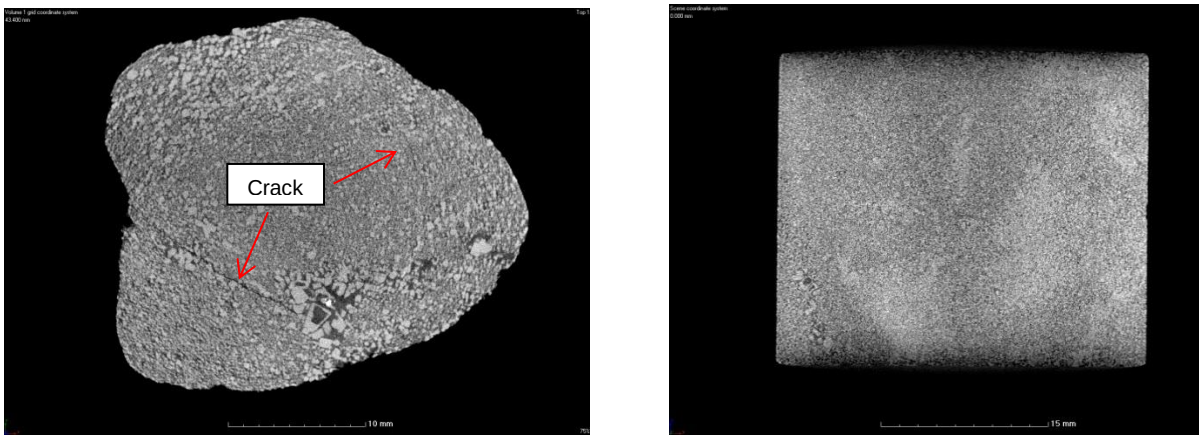

(a) (b)

Figure 4-13: 2D tomography images for (a) RoM and (b) cut drill core UG2 chromitite -31.5 + 26.5 mm specimens

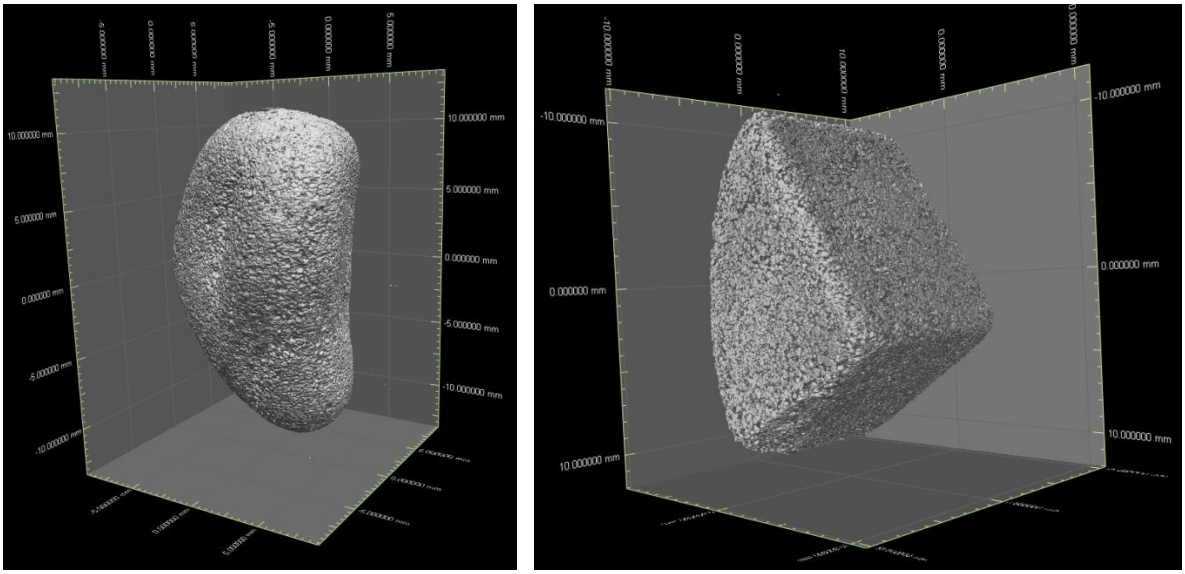

(a) (b)

Figure 4-14: 3D tomography images for (a) RoM and (b) cut drill core UG2 chromitite - 16 + 13.2 mm specimens

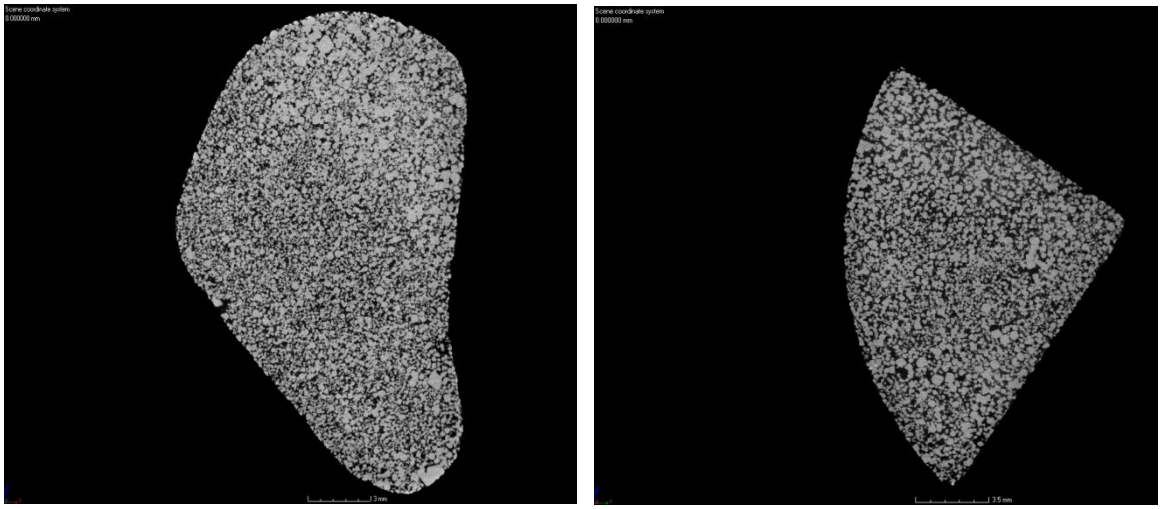

(a) (b)

Figure 4-15: 2D tomography images for (a) RoM and (b) cut drill core UG2 chromitite - 16 + 13.2 mm specimens

From the tomographic images presented in Figure 4-12 to 4-15, there are visible cracks in the large UG2 RoM ore particles. No visible cracks were seen in the corresponding cut drill core particle. This trend was consistent to the findings by Hahne, Pålsson and Samskog (2003) who also showed that RoM ore particles contain microflaws. There are no visible cracks in the small particles. This is to be expected, because as highlighted by studies such as Banini (2000), crack density decreases with decrease in particle size.

Characterisation of the abundant rock types in the subsequent sections is based on results from breakage tests of samples obtained via particle selection method. The reasons were twofold, the availability of RoM samples for experimental work permitting repeats and similar trends observed between the particle selection and cut drill core method results. Results obtained for the cut drill core particles are presented in Appendix C.

4.4.2 Progeny particle size distributions of the main rock types

Progeny particles from breakage tests performed using the RBT of the main rock types identified in the Karee 3 UG2 RoM stock pile were evaluated. Figure 4-16 presents the progeny particle size distributions for small particles (-16.0 + 13.2 mm) of the UG2 chromitite, pyroxenite, spotted anorthosite and mottled anorthosite. Figure 4-16 (a), (b) and (c) show the progeny particle distributions for the main rock types from single impact breakage tests performed at 0.25, 1.0 and 2.5 kWh/t respectively.

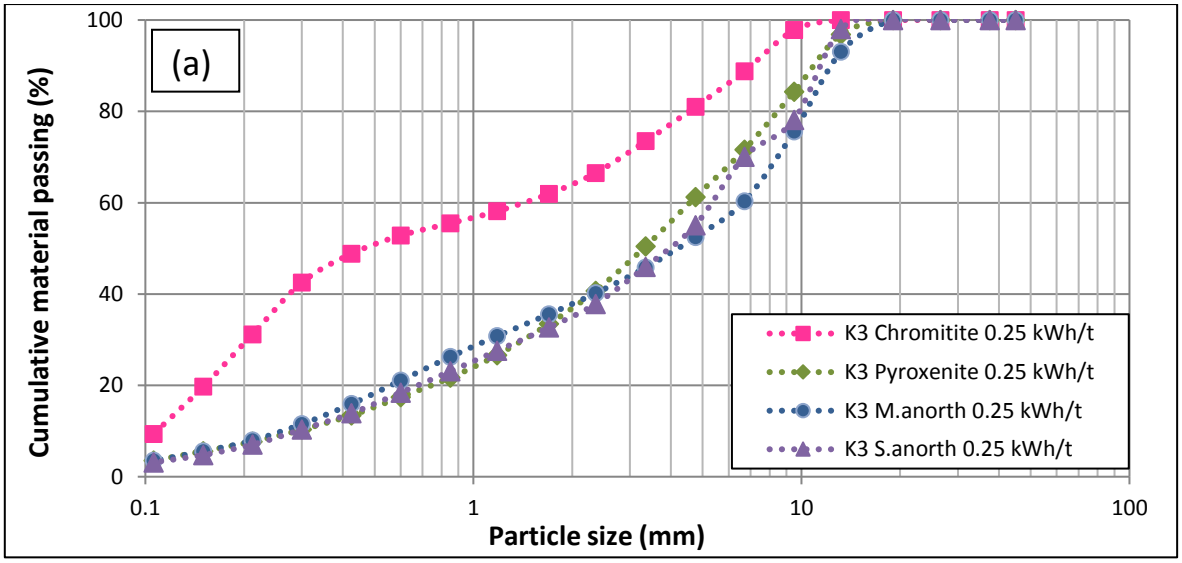

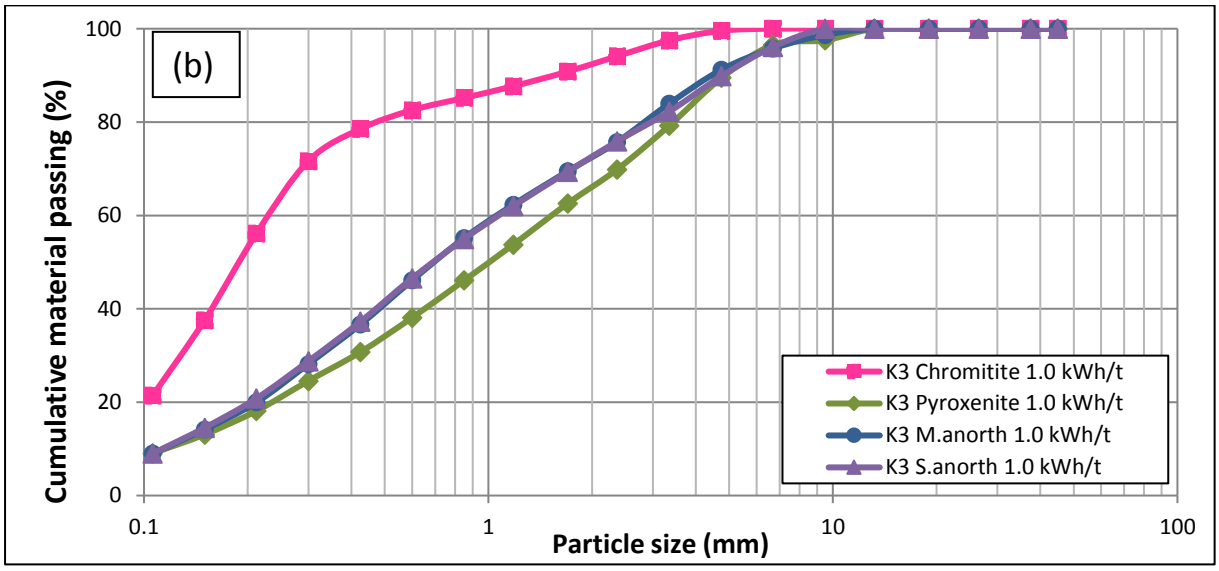

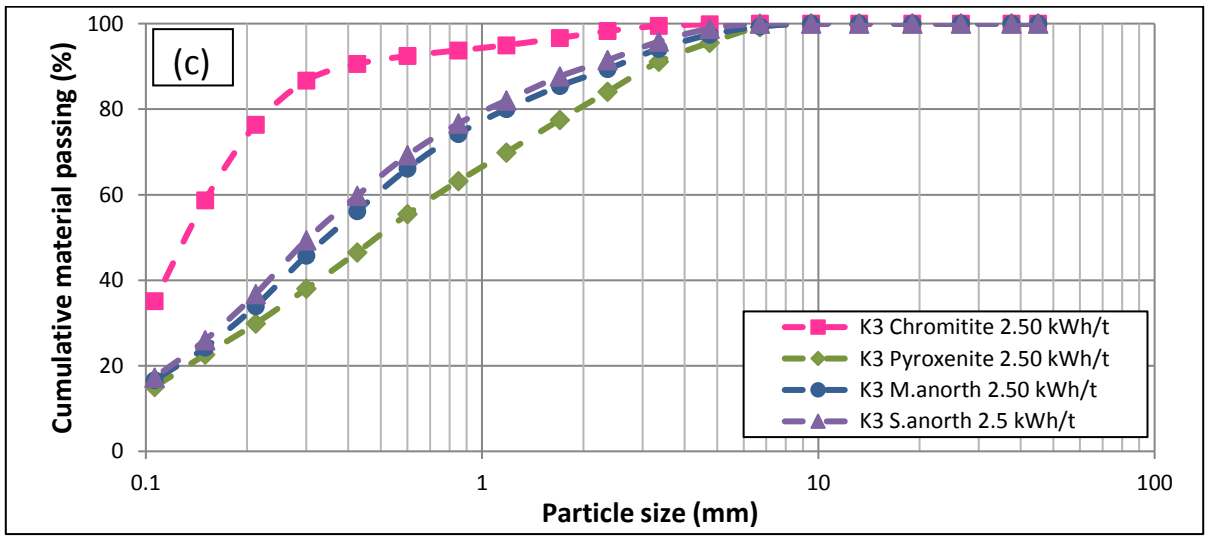

Figure 4-16: Progeny particle size distributions of the UG2 abundant rock types

For all the plots presented in Figure 4-16, the progeny particle size distribution for chromitite were finer than the other rock types at each energy level tested. Similar trends were exhibited for all sizes tested as presented in Appendix C. From the mineralogical analysis presented in section 4.2.1, UG2 chromitite was found to consist predominantly of fine-grained chromite held together mainly by orthopyroxene and plagioclase. Due to the small amounts of orthopyroxene and plagioclase which hold chromite grains together, the particle easily fragments when stress is applied. From their work on RoM ball mills, Mainza and Powell (2006) pointed out that UG2 chromitite (reef) is friable. The friability of the chromitite was also witnessed during the ore sorting stage of this study.

Mottled and spotted anorthosite produce less fines than chromitite as exhibited by the lower cumulative material passing each particular size for all energies in Figure 4-16. The mineralogical analysis presented in section 4.2.3 indicated that mottled and spotted anorthosite are made up of plagioclase crystals which are few centimetres long. These plagioclase crystals were found to be larger than the chromite grains in chromitite thus mottled and spotted anorthosite break into a coarser progeny compared to chromitite after a single impact. In addition, Figure 4-16 shows that there is no significant difference between the progeny particle size distributions for mottled and spotted anorthosite across all three energy input despite the rocks having different textures as presented in sections 4.2.3 and 4.2.4. Both mottled and spotted anorthosite progeny particle size distributions were finer than pyroxenite for all the energies tested. Figure 4-16 also shows that pyroxenite had a coarser progeny particlet size disributions compared to the other rocks. Pyroxenite was found to contain predominantly granular orthopyroxene, interstitial plagioclase and clinopyroxene. This texture tends to be complex as pointed out by Xiao and Laplante (2004), thus fracturing into a coarser product than all the rock types tested.

The shape of progeny particle size distributions for UG2 chromitite presented in Figure 4-10 and 4-16 is bimodal. This is more visible at low energies especially at 0.25 kWh/t. Similar particle size distributions were also obtained for UG2 ore by Van Eck (2007). The observed point of inflection in Figure 4-10 and 4-16 falls in the - 425 + 300 µm size fraction. This corresponds to the chromite grain size class which was found to be in the - 425 + 300 µm size fraction as shown in the work by Daniel (2007). This tends

to indicate that chromitite particles prefentially break along the chromite grain boundaries as suggested by Chernet and Marmo (2003).

The shape of progeny particle size distributions for mottled anorthosite, spotted anorthosite and pyroxenite are smooth curves without kinks. This tend to suggest that random fracture occurs in the breakage process of these rock types and there is no selective breakage of one mineral over another.

4.4.3 Effect of energy input on progeny particle size distributions

The effect of input energy on the progeny particle size distibutions of UG2 rock types was also assessed. Figure 4-10, 4-11 and 4-16 showed that increasing the specific input energy from 0.25 to 2.5 kWh/t results in finer progeny particle size distributions for all rock types tested. This collaborates with the visual presentation in Figure 4-9 which showed that progeny particles become finer as the input energy is increased. Increasing the input energy, increases the stressing intensity which inturn intensifies the propagation of cracks in a material (Tavares, 2007). This results in fracturing of the particle into smaller fragments (Kapur et al., 1997).

4.5 Degree of breakage (t_{10})

Degree of breakage represented by the parameter t_{10} defines the extent of breakage or fineness of the progeny particle size distribution resulting from the applied energy. t_{10} is defined as the progeny percentage passing one tenth of initial mean particle size (Napier-Munn et al., 1996).

A tenth of the original particle geometric mean size (t_{10} screen size) for each of the size fractions used in the standard impact breakage tests was calculated to aid in the determination of t_{10}. The t_{10} parameter was determined by interpolating the cumulative percent passing data between the two closest sieve sizes to the t_{10} screen size (see Appendix B).

4.5.1 Comparison of the t_{10} for particle selection and cut core methods

The aim of this section was to assess the extent of breakage or fineness of the progeny fragments for UG2 samples collected via particle selection and cut core method. A comparison of the degree of breakage for progeny particles from breakage tests using

the RBT of grab samples collected from the stockpile and cut drill core particles was made for the -16.0 + 13.2 mm and - 31.5 + 26.5 mm of each rock type tested. The comparison for the two size classes was possible because cut drill core particles were available only in these size fractions. Figure 4-17 and 4-19 present the comparison of t_{10} values obtained from the two sampling methods for UG2 chromitite and pyroxenite respectively at three energy levels tested. Similar results were obtained for mottled and spotted anorthosite which are presented in Appendix D.

Figure 4-17 and 4-18 show that at all energy levels tested, higher t_{10} values were obtained for the particle selection method compared to the cut core method. The error bars presented for the particle selection method are $\pm$ one standard error which is 68% confidence interval of the t_{10} values obtained. Higher t_{10} values show that grab samples collected from the stockpile exhibit higher degrees of breakage thus producing a finer progeny than the cut drill core particles. The observed trends for the t_{10} parameter for both chromitite and pyroxenite in Figure 4-17 and 4-18 are consistent with the progeny particle size distribution plots Figure 4-10 and 4-11. This is mainly attributed to cracks present in the RoM stock pile particles as shown in the tomographic scans in Figure 4-13 (a). These cracks are induced through pre-weakening processes such as blasting and transportation of material to the stockpile as pointed out in work such as Hahne, Pålsson and Samskog (2003). The cracks act as stress raisers when the particle is under load (Tavares & King, 1998) resulting in the generation of fine fragments (Schönert, 2004). On the other hand, drill cores were carefully cut thus introducing fewer flaws in the tested particles. No cracks were observed from the tomographic scans of the cut drill core specimens analysed in this work.

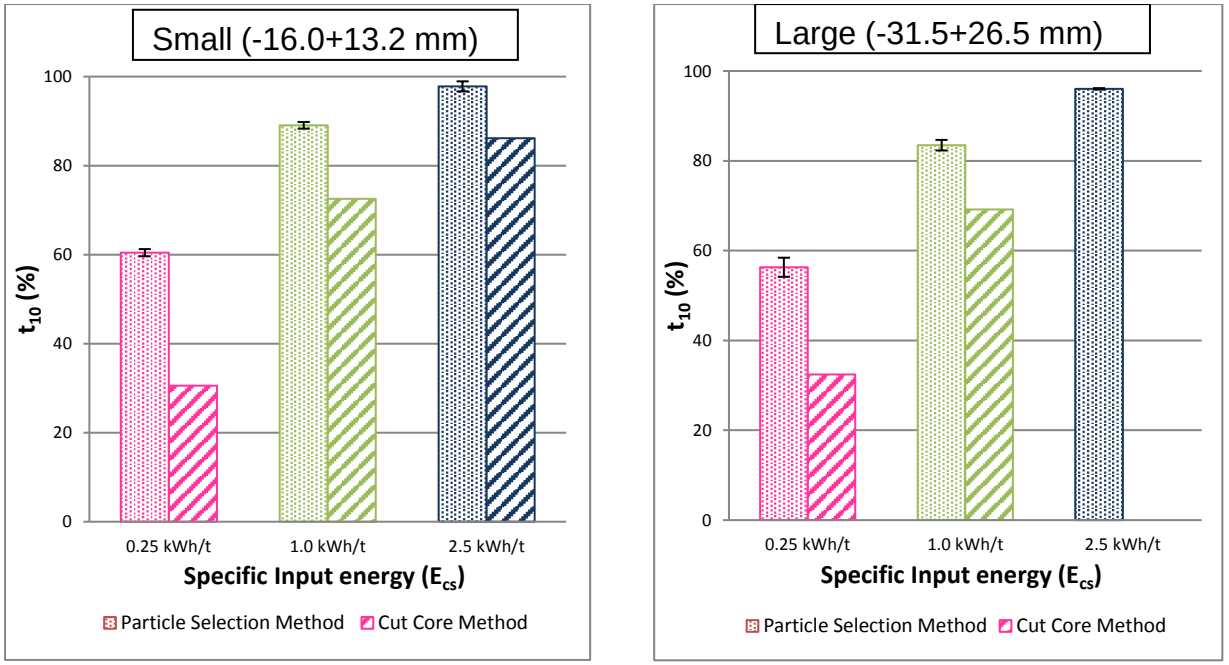

Figure 4-17: Comparison of the t_{10} for UG2 chromitite obtained using the particle selection and cut core method

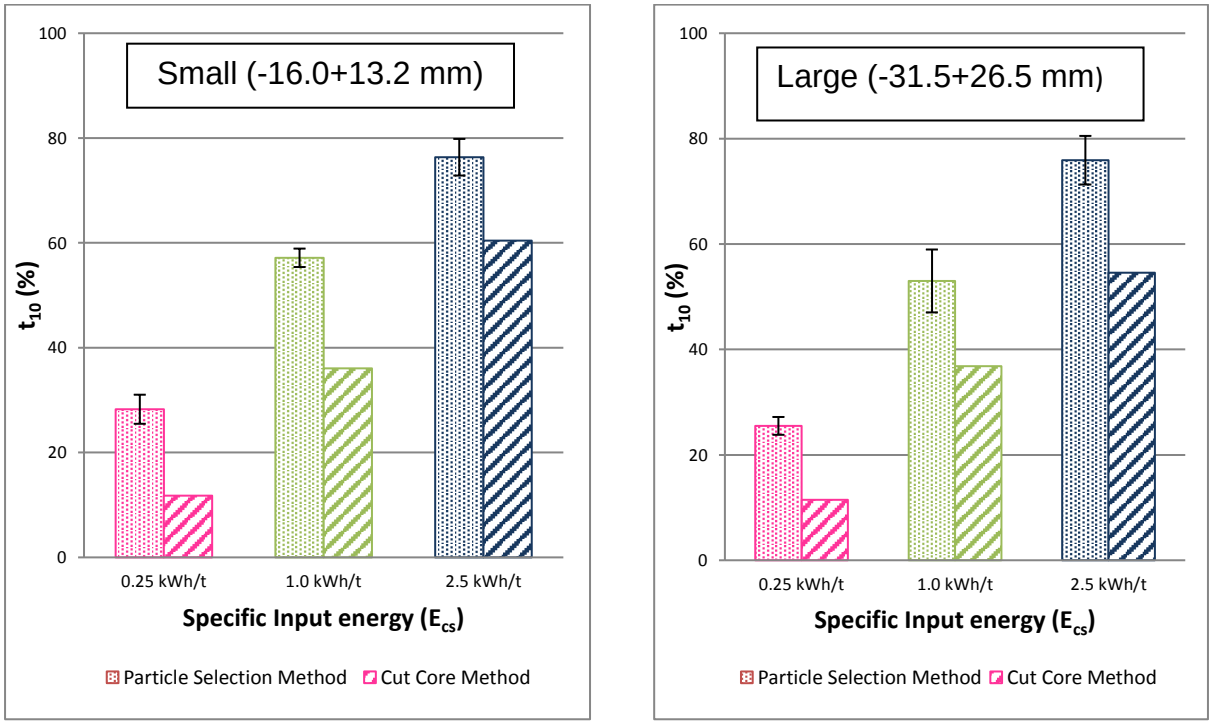

Figure 4-18: Comparison of the t_{10} for UG2 pyroxenite obtained using the particle selection and cut core method

4.5.2 Comparison of the t_{10} for the main rock types

The t_{10} values obtained from the impact breakage test using the RBT were used to evaluate the fineness of the progeny fragments for the main rock types sourced from UG2 RoM stock pile. Table 4-1 presents t_{10} values for UG2 chromitite, pyroxenite, spotted anorthosite and mottled anorthosite particles at each energy-size combination tested. At some energy-size combinations for pyroxenite, spotted and mottled anorthosite, no standard error was calculated because no repeats were done due to limited samples. This was acceptable because for each energy-size test in the standard breakage experiments, 30 particles are used to give results that are statistically valid (Napier-Munn et al., 1996). The results tabulated in Table 4-1 were used to assess the effect of input energy on the degree of breakage (t_{10}) of the main rock types in the subsequent sections. The comparison of breakage properties of the main types is well pronounced and discussed in the following section.

Table 4-1: t_{10} values obtained for the UG2 main rock types

Rock type	Size		Energy	Average t_{10}	Std. error.
	Class	Range (mm)	(kWh/t)	(%)	
Chromitite	Small	16.0 x 13.2	0.25	60.4	0.46
			1.00	89.1	0.43
			2.50	97.8	0.65
	Medium	22.4 x 19.0	0.25	56.9	0.42
			1.00	85.2	1.11
			2.50	96.4	0.57
	Large	31.5 x 26.5	0.25	56.3	1.23
			1.00	83.5	0.68
			2.50	96.0	0.09
	V.Large	45.0 x 37.5	0.10	28.6	1.04
			0.25	46.3	1.66
			1.00	81.4	0.90
Pyroxenite	Small	16.0 x 13.2	0.25	28.3	1.96
			1.00	57.2	1.24
			2.50	76.3	2.47
	Medium	22.4 x 19.0	0.25	25.5	0.67
			1.00	53.0	2.91
			2.50	75.9	0.49
	Large	31.5 x 26.5	0.25	22.8	1.20
			1.00	50.7	4.22
			2.50	75.9	3.26
	V.Large	45.0 x 37.5	0.10	16.1	-
			0.25	24.8	-
			1.00	60.3	-
Spotted Anorthosite	Small	16.0 x 13.2	0.25	30.3	-
			1.00	65.9	-
			2.50	85.0	-
	Medium	22.4 x 19.0	0.25	-	-
			1.00	73.3	-
			2.50	-	-
	Large	31.5 x 26.5	0.25	23.5	-
			1.00	65.5	-
			2.50	-	-
	V.Large	45.0 x 37.5	0.10	11.7	-
			0.25	-	-
			1.00	63.0	-
Mottled Anorthosite	Small	16.0 x 13.2	0.25	33.3	-
			1.00	66.1	-
			2.50	82.8	-
	Medium	22.4 x 19.0	0.25	25.8	-
			1.00	68.8	-
			2.50	79.6	-
	Large	31.5 x 26.5	0.25	20.6	-
			1.00	51.5	-
			2.50	85.3	-
	V.Large	45.0 x 37.5	0.10	11.8	-
			0.25	23.0	-
			1.00	61.0	-

4.5.3 Effect of energy input on the degree of breakage

The t_{10} was used to assess the resistance to breakage for the different rock across different energies tested. Figure 4-19 and 4-20 illustrate the effect of energy input on the degree of breakage, t_{10}, of small (-16.0 + 13.2 mm) and large (-31.5 + 26.5 mm) size classes for all the rock types tested. The energy input was increased from 0.25 to 2.5 kWh/t. Due to limited samples of large spotted anorthosite, no test was performed at 2.50 kWh/t.

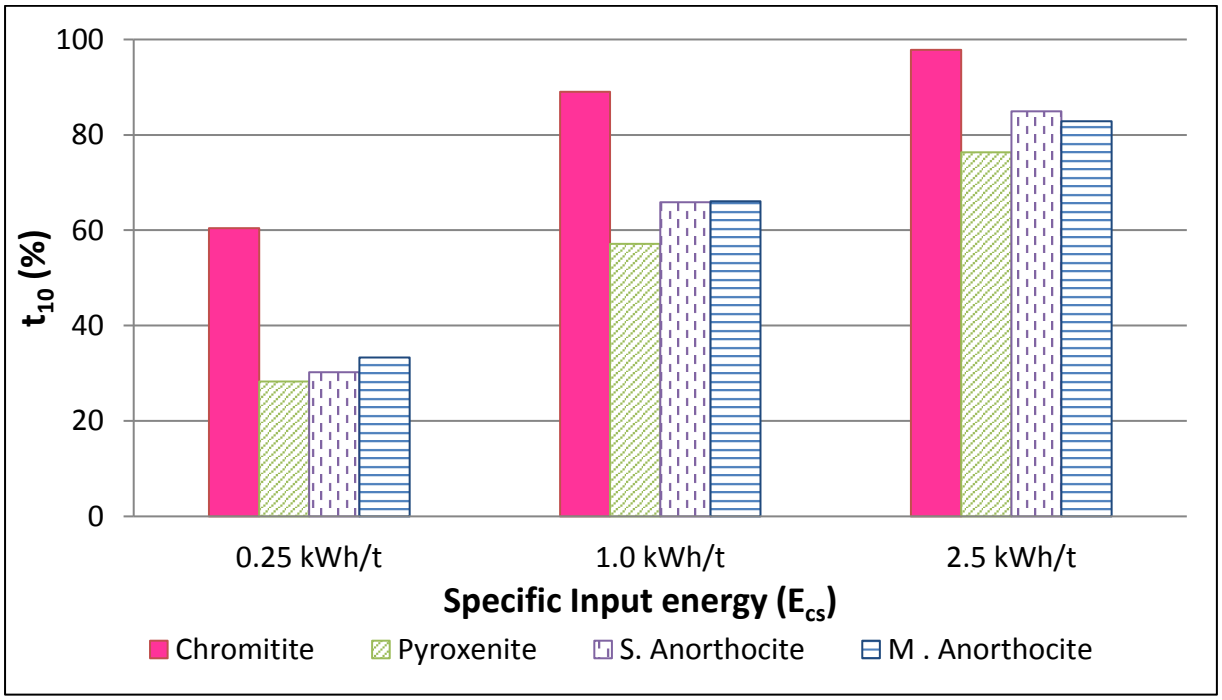

Figure 4-19: Effect of input energy on the degree of breakage of various UG2 rock deposits for small (-16.0 + 13.2 mm) particles.

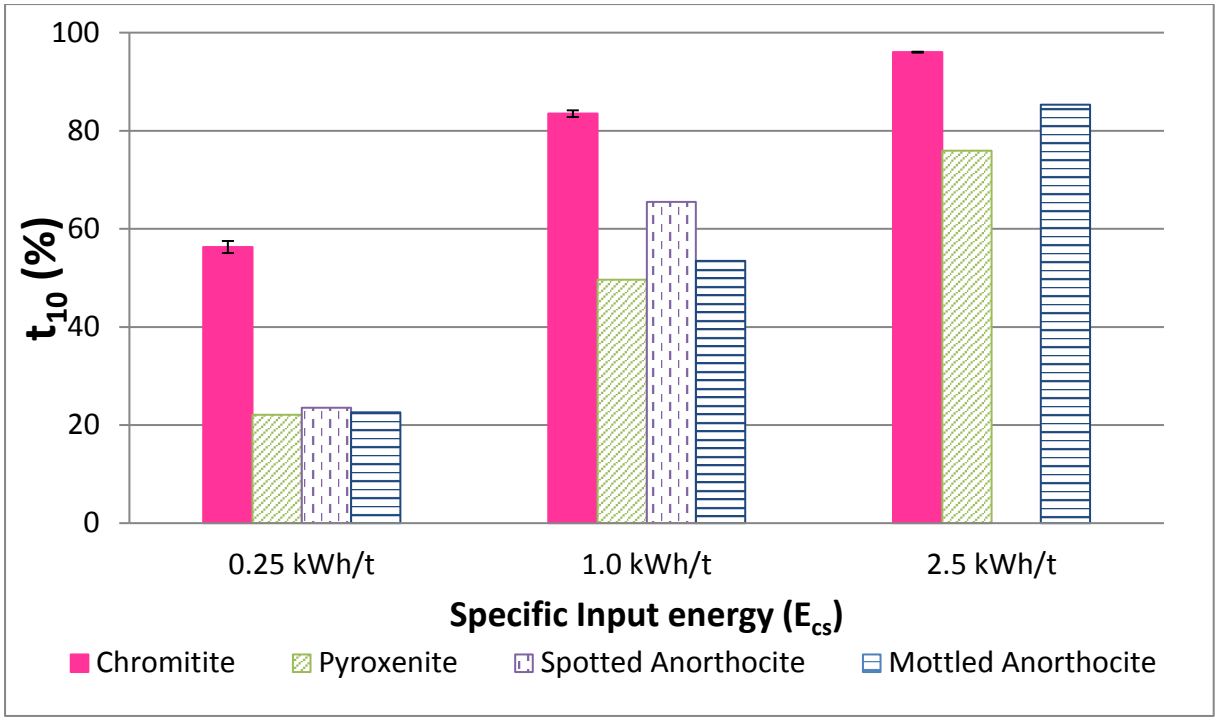

Figure 4-20: Effect of input energy on the degree of breakage of various UG2 rock deposits for large (-31.5 + 26.5 mm) particles.

Figure 4-19 and 4-20 show that t_{10} increased with each successive energy level for all the rock types tested. As t_{10} represents the degree of breakage, increase in the index indicates that more fine particles are generated as the input energy is increased. This observation was found to be consistent for all size fractions tested (presented in Appendix D). This is because increasing the impact energy, increases the stress intensity within the particles thus intensifying the propagation of cracks as shown by Tavares (2007). The increase in the generation and propagation of cracks results in fracturing of the particle into smaller fragments to produce more fine products (Kapur et al., 1997).

Chromitite particles fragment into finer progeny particles compared to the other rock types evidence by the higher t_{10} values at each energy level in Figure 4-19. Therefore, it can be concluded that chromitite has the lowest resistance to breakage for the rock types tested. As discussed in section 4.2.1, UG2 chromitite consists mainly of fine-grained chromite loosely cemented in orthopyroxene and plagioclase matrix. The chromite grains easily crumbles when stress is applied.

The t_{10} values obtained for mottled and spotted anorthosite were found to be lower than chromitite. This is because mottled and spotted anorthosite are coarse-grained

rocks as presented in the mineralogical analysis in section 4.2.3 and 4.2.4 thus they break into coarser progeny fragments as compared to chromitite. In addition, there is no significant difference between the t_{10} values obtained for mottled and spotted anorthosite despite the textural difference for these anorthositic rocks. The textural distinction between mottled and spotted anorthosite presented in section 4.2.3 and 4.2.4 illustrates that constituent pyroxene creates dark speckles giving a ‘’spotted’’ appearance in spotted anorthosite whilst mottled anorthosite was found to be mainly plagioclase.

Figure 4-19 also shows that pyroxenite tended to have the least t_{10} across all energy levels tested. As presented in section 4.2.2, UG2 pyroxenite specimen was found to contain granular orthopyroxene, held together by plagioclase and clinopyroxene similarly to what was reported by Mathez and Mey (2005). This texture tends to be complex, thus fracturing into a coarser product than all the rock types tested. The orthopyroxene grains were found to be relatively larger than the chromite grains in chromitite particles thus a coarser product is expected resulting in a lower t_{10} values.

4.6 Energy – size relationships

The energy-size relationships were investigated using the standard impact breakage characterisation models (equation 2-5 and 2-9) described in section 2.6. These models relate the degree of breakage, t_{10}, to specific input energy E_{cs}.

4.6.1. t_{10} breakage model

The t_{10} values obtained from cumulative material passing data for the progeny particles of the different size fractions from impact breakage tests using the RBT for each rock type were plotted against specific input energy, E_{cs}. The t_{10} breakage model (equation 2-5) was fitted to the breakage data of each rock type by non-linear regression techniques.

Figure 4-21 and 4-22 show the relationship of the measured t_{10} versus the applied specific energy for UG2 chromitite and pyroxenite rock particles collected from Karee 3 shaft. The breakage parameters, A and b, were fitted to provide the least root mean square error (RMSE). The solid and broken black lines represent the model predictions for the particle selection and cut core methods respectively.

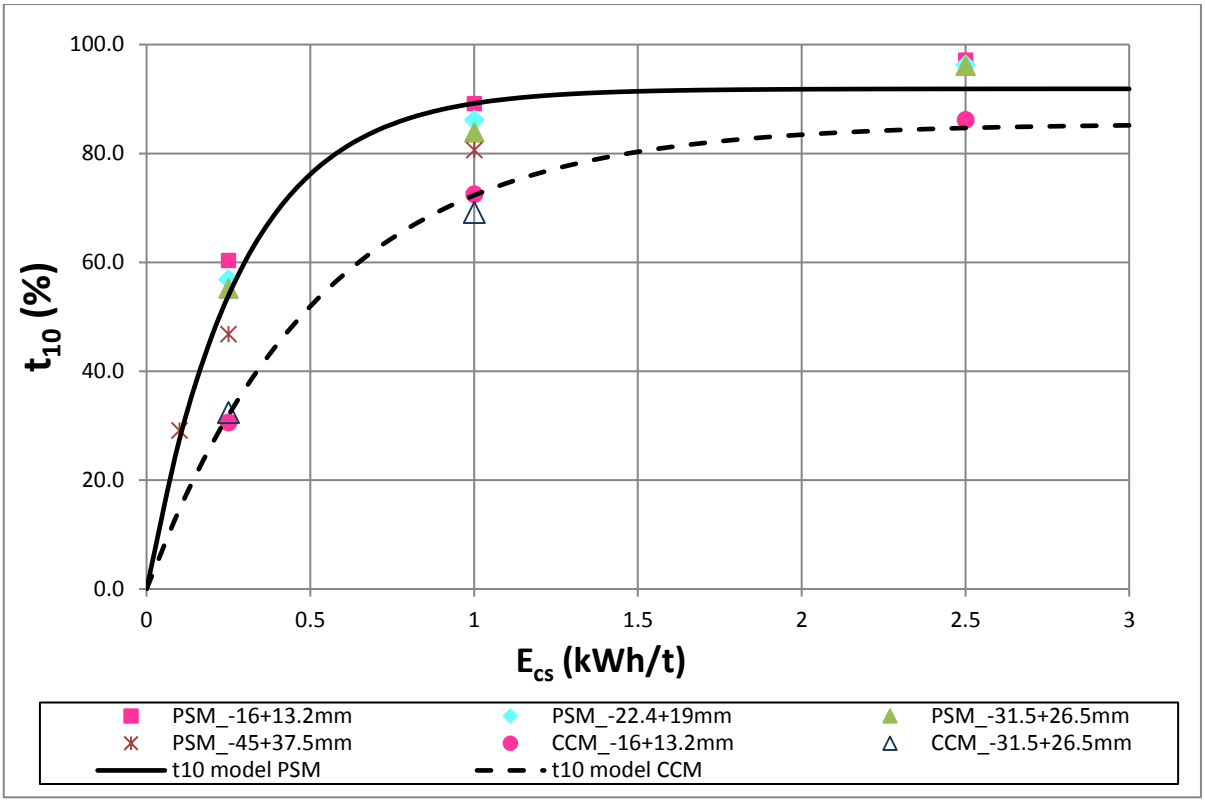

Figure 4-21: t_{10} breakage model fitting to the t_{10}-E_{cs} data for UG2 chromitite rock particles

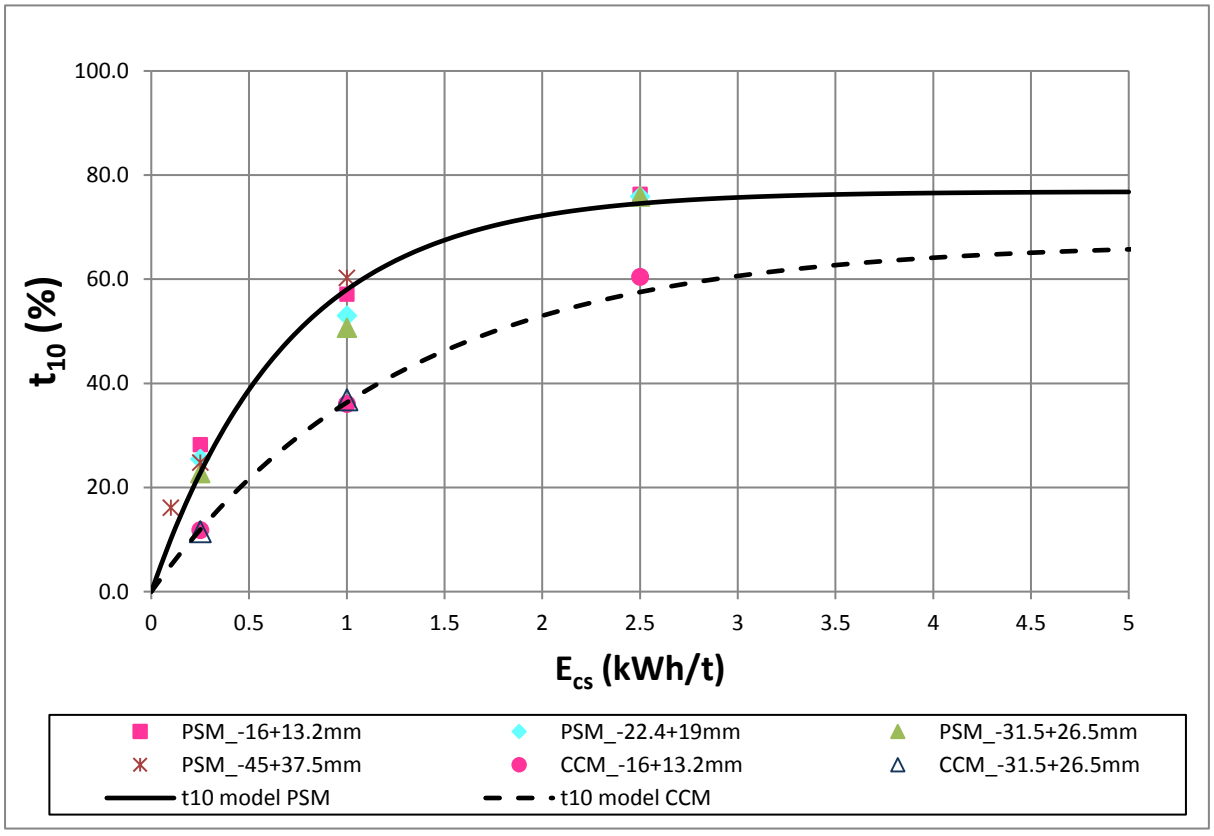

Figure 4-22: t_{10} breakage model fitting to the t_{10}-E_{cs} data for UG2 pyroxenite rock particles

Figure 4-21 and 4-22 confirm that the relationship between t_{10} and E_{cs} is not linear but of the exponential form as first presented by Leung (1987). t_{10} increases with each successive energy level for all particles sizes. Similar trends were obtained for mottled and spotted anorthosite samples tested as presented in Appendix E. This reflects that for higher energy inputs, higher degrees of breakage were attained. However, as the input energy increases, the rate of increase in the degree of breakage decreases until no further significant increase in t_{10} occurs. The maximum t_{10} value or the horizontal asymptote corresponds to parameter A (Napier-Munn et al., 1996). This maximum value indicates that at higher energies, there is little additional size reduction as the E_{cs} is increased, that is, the size reduction process becomes less efficient.

The linear gradient of the t_{10} versus E_{cs} plot at energies lower than 1 kWh/t gives the value of b (Napier-Munn et al., 1996). The value of b can be related to material stiffness (Napier-Munn et al., 1996) which is a measure related to the deformation behaviour (Tavares & King, 1998). Also of great importance is the product of A and b (Axb) which is the slope of t_{10}–E_{cs} curve at 'zero' input energy (Napier-Munn et al., 1996). It is used as an indicator of ore resistance to breakage. A lower Axb value shows that the ore has a high resistance to impact breakage whilst a higher Axb indicates a readiness to fracture (Hahne et al., 2003). The breakage parameters for the chromitite, pyroxenite, spotted anorthosite and mottled anorthosite obtained for RoM ore and cut drill core samples are summarised in Table 4-2 along with their associated regression statistics.

Table 4-2: Ore hardness parameters, A , b and Axb for the UG2 chromitite, pyroxenite, spotted anorthosite and mottled anorthosite determined using the t_{10} model

UG2 Rock type	Sampling method	A	b	Axb	RMSE	R^2
Chromitite	Particle Selection	91.9	3.53	**325**	16.8	0.950
	Cut Core	85.4	1.87	159	3.7	0.996
Pyroxenite	Particle Selection	76.8	1.41	**108**	13.0	0.974
	Cut Core	67.1	0.779	52.3	4.2	0.992
Spotted Anorthosite	Particle Selection	86.0	1.60	**138**	6.6	0.989
	Cut Core	84.1	1.21	101	10.6	0.968
Mottled Anorthosite	Particle Selection	84.9	1.35	**115**	17.2	0.963
	Cut Core	73.8	1.05	77.6	1.8	0.990

Table 4-2 shows that for each rock type tested, higher A values were obtained for particle selection method. Higher A values meant that at higher energies, greater degrees of breakage were achieved. Also, higher values of b were obtained for particle selection method. Higher b values obtained for stockpile materials show a lesser resistance to deformation prior to fracture than cut drill core particles.

Table 4-2 also shows that the samples from the particle selection method tend to have a higher Axb value than cut core samples for all rock types tested. This shows that the RoM ore particles offer less resistance to impact breakage. RoM ore particles contain more microflaws as shown in the tomographic scans in section 4.4.1 induced through pre-weakening processes (blasting and transportation) (Hahne, Pålsson & Samskog, 2003). As discussed in section 4.4.1, these flaws act as stress raisers when the particle is under load thus making the particle less resistant to impact breakage.

Axb values for chromitite sourced via particle selection and cut core methods were determined to be 325 and 159 respectively as presented in Table 4-2. According to Napier-Munn et al (1999), UG2 chromitite tested was thus classified as very soft. Table 4-2 also indicates that Axb values for UG2 chromitite obtained using either particle selection or cut core method were higher than respective breakage indicators obtained for the other rocks. This highlights that chromitite exhibit the highest amenability to fragmentation via impact. UG2 chromitite was found to consist predominantly of fine-grained chromite cemented mainly by orthopyroxene and plagioclase as presented in section 4.2.1. Chromitite was found to be friable and easily fragments when stress was applied due to the small amounts of orthopyroxene and plagioclase which hold the chromite grains together.

Mottled and spotted anorthosite offer more resistance to impact breakage compared to chromitite as indicated by lower Axb values in Table 4-2. The Axb values for both rock types collected via the particle selection and cut core methods range from 77.6 to 138 hence mottled and spotted anorthosite are classified as soft to very soft. The anorthositic rocks are coarse grained as illustrated in sections 4.2.3 and 4.2.4 resulting in lower Axb values. Table 4-2 also shows that pyroxenite has the highest resistance to impact breakage as revealed by the lowest Axb values. As discussed in 4.2.3, UG2 pyroxenite contained orthopyroxene grains that are relatively larger than the chromite grains thus fracturing into a coarser product. In addition, the texture of the pyroxenite

is complex made up of mainly granular orthopyroxene, interstitial plagioclase and clinopyroxene. This tends to have a more compact texture as presented in Figure 4-3 and thus the least responsiveness to breakage. From the size classes reported by Napier-Munn et al (1999), the Axb values for pyroxenite (52.3 to 108) fall into the medium to soft class.

The t_{10} breakage model was found to be deficient in handling variation due to the effect of particle size as presented in Figure 4-21 and 4-22. A and b parameters for each rock type are generated for all particle sizes by assuming that particles of different sizes break in the same way when subjected to the same impact energy (Banini, 2000). However, as illustrated in Figure 4-21 and 4-22, each size class followed a distinct exponential pattern. Further analysis was done by plotting the predicted t_{10} values against the measured values for the UG2 chromitite samples sourced from the stockpile as shown Figure 4-23.

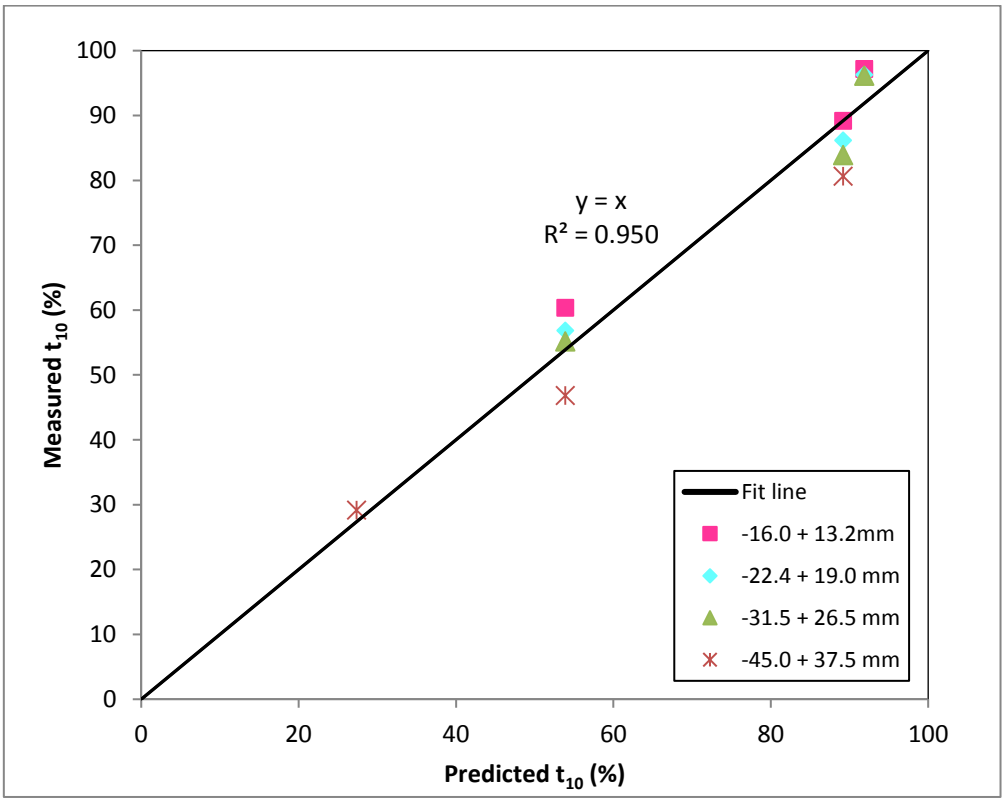

Figure 4-23: Measured vs predicted t_{10} values for the RBT products of UG2 chromitite particles from RoM ore stockpile using the t_{10} breakage model

The closer the points are to the fitted line, y=x, the stronger the correlation between the model's predictions and the measured results. The data points for all sizes of UG2 chromitite particles are scattered around the fit line suggesting that there is a fair

correlation between the predicted and the measured t_{10} values. The R^2 value (a number from 0 to 1) presented in Table 4-2 quantifies how closely the predicted t_{10} values correspond to the measured values. The model is more reliable when the R^2 value for the regressed line is at or close to 1. The R^2 value for the chromitite breakage data was found to be 0.950. The value shows that there are some deficiencies in the model in predicting breakage behaviour for chromitite particles. As shown in Figure 4-23 the data points are more scattered at higher t_{10} values.

The t_{10} breakage model assumes that the size of the particle does not affect the breakage process and thus the particle size is not factored in resultant breakage model. However, the findings presented in Figure 4-21 show some slight size dependency of the resultant breakage event for chromitite particles. Banini (2000), Shi and Kojovic (2007) also demonstrated particle size effects on ore breakage. They found that smaller particles had lower degrees of breakage. This trend is due to the microstructure of smaller particles which have a lower probability of containing cracks and flaws (Shi & Kojovic, 2007; Banini, 2000). According to King (2001), the presence of internal cracks and flaws plays an important role in the fracture of the material. As a result, for a same input energy, a higher degree of breakage is expected for larger particle sizes as demonstrated in Figure 4-21.

4.6.2. Size dependent breakage model

The breakage model developed by Shi and Kojovic (2007) incorporating the effect of size to describe the degree of breakage was fitted to the breakage data by non-linear regression techniques. For the fitting, the number of impacts, k, was taken to be 1 as no incremental breakage tests were performed. The energy threshold (E_{min}) below which infinite impacts will not result in fracture was be taken to be zero as suggested by Zuo and Shi (2015). This was a valid assumption since high t_{10} values were obtained by a single impact even at low energies.

The parameter, f_{mat} is a size dependent material property which characterises the resistance of particulate material against fracture in impact comminution (Zuo & Shi, 2015; Vogel & Peukert, 2004). f_{mat} for each size class and a global M (maximum t_{10} for a material subjected to breakage) for each specific test, were fitted to provide the least root mean square error (RMSE). The model fittings for UG2 chromitite and pyroxenite are presented in Figure 4-24 and 4-25 respectively.

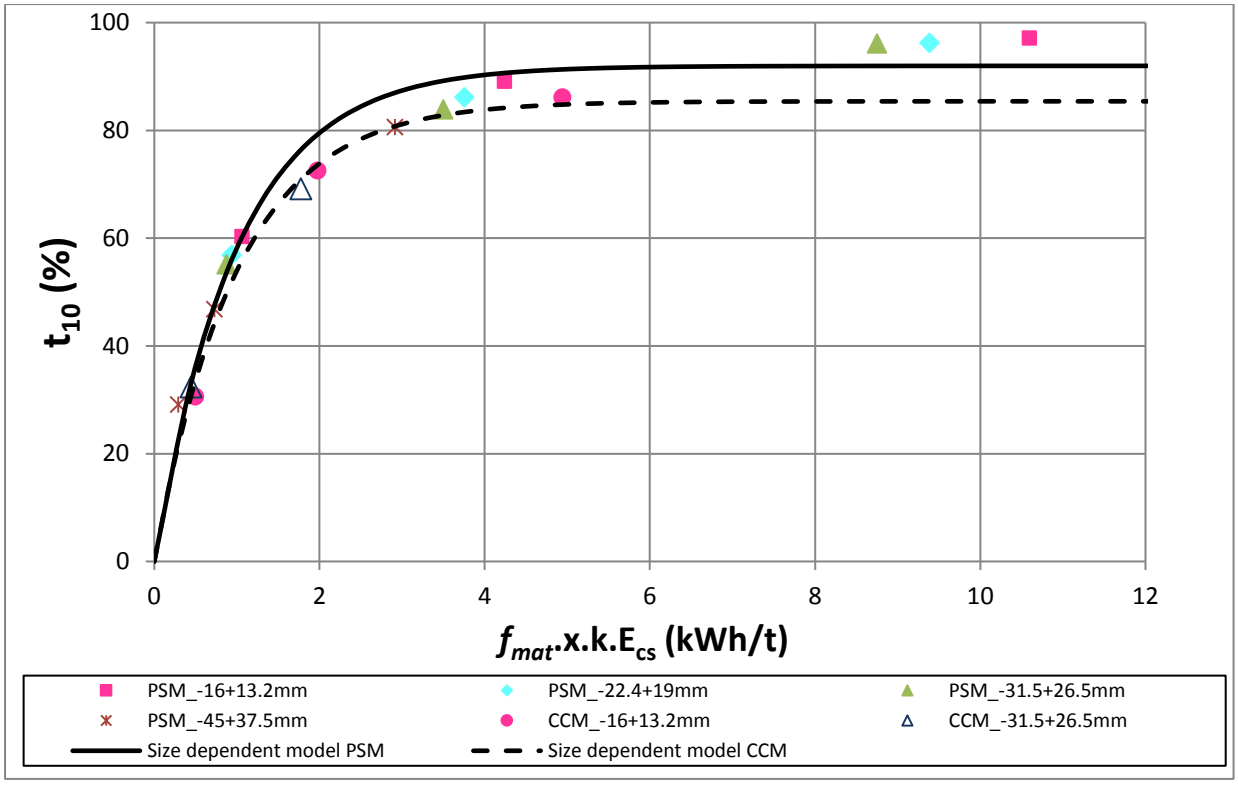

Figure 4-24: Size dependent breakage model fitting to the particle selection and cut core breakage data for UG2 chromitite

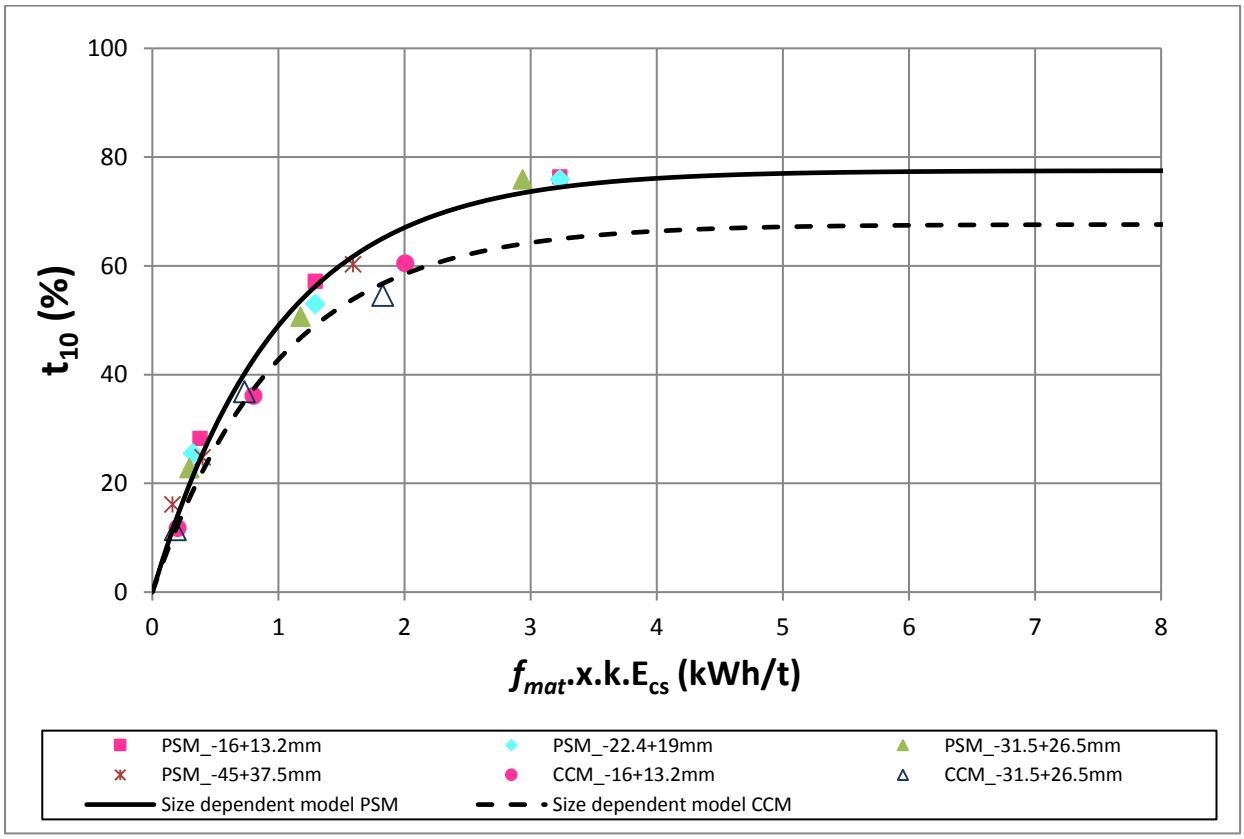

Figure 4-25: Size dependent breakage model fitting to the particle selection and cut core breakage data for UG2 pyroxenite

Figure 4-24 and 4-25 show that the data points are closer to the fitted model especially at lower energy levels compared to the fittings in Figure 4-21 and 4-22 respectively. The model parameters obtained by fitting the size dependent breakage model for chromitite, pyroxenite, spotted anorthosite and mottled anorthosite are summarised in Table 4-3 along with their associated regression statistics.

Table 4-3: Ore breakage parameters for the tested UG2 rock types determined by fitting the breakage data to the size dependent model

			Particle mean size x (mm)					
			14.5	20.6	28.9	41.1		
Ore type	Sampling method	M (%)	f_{mat} (kg J^{-1} m^{-1})				RMSE	R^2
Chromitite	Particle Selection	91.9	0.081	0.050	0.033	0.019	16.8	0.985
	Cut Core	85.4	0.039	-	0.017	-	3.7	0.996
Pyroxenite	Particle Selection	77.5	0.028	0.017	0.011	0.011	15.5	0.988
	Cut Core	67.6	0.017	-	0.008	-	5.2	0.992
Spotted	Particle Selection	85.6	0.031	0.026	0.014	0.010	3.45	0.997
Anorthosite	Cut Core	84.1	0.019	-	0.009	-	6.53	0.990
Mottled	Particle Selection	84.3	0.033	0.021	0.010	0.009	10.4	0.987
Anorthosite	Cut Core	70.1	0.018	-	0.031	-	1.79	0.999

Values of A and M which represent the maximum t_{10} for the t_{10} breakage model and the size dependent model respectively were found to be the same as shown in Table 4-2 and Table 4-3. The value of M followed the same trend as A. Higher M values were achieved for RoM ore samples compared to cut drill core samples as illustrated in Figure 4-24 4-25 and Table 4-3 for all the rock types tested.

Figure 4-24 and 4-25 also show that t_{10}-E_{cs} curve for the particle selection method had a steeper gradient compared to the cut core method. The slope of t_{10}-E_{cs} is closely related to the material property f_{mat} (Zuo & Shi, 2015). The f_{mat} values presented in Table 4-3 for samples obtained from the stockpile were found to be higher than the cut drill core particles across all size tested and for all the rock types. Also, the size dependency of f_{mat} is exhibited, with the parameter increasing with reduction in particle size.

The regression statistics presented in Table 4-3 show lower RMSE and higher R^2 for the size dependent model as compared to the values obtained from the t_{10} breakage model in Table 4-2. This shows stronger correlation between the values predicted by

the size dependent model and the measured t_{10} values. This is also evidenced in Figure 4-26 which shows a better fit of the size dependent model's prediction of the t_{10} plotted against the measured values.

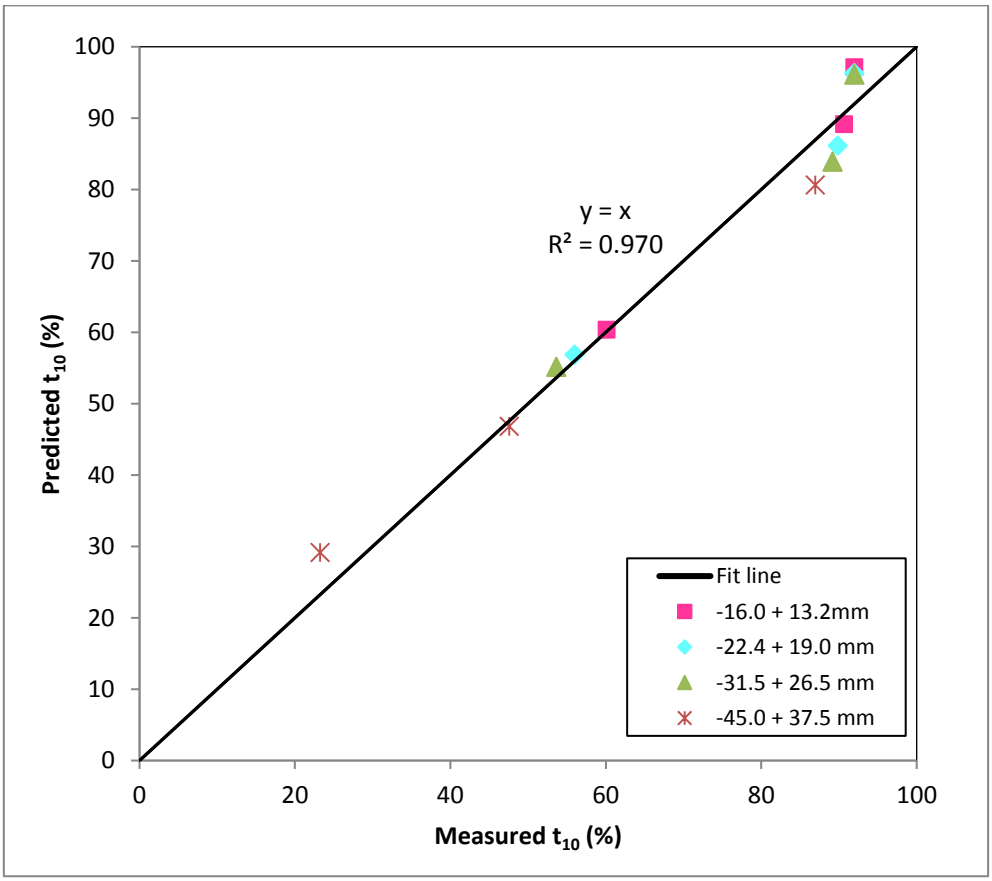

Figure 4-26: Predicted vs measured t_{10} values for the RBT products of UG2 chromitite particles from RoM ore stockpile using the size dependent breakage model

An indicator of ore resistance to breakage (hardness) can also be evaluated for each size class from the parameters in Table 4-3 using equation 4-1. The ore hardness indicator is given by the slope of the t_{10}–E_{cs} curve at 'zero' input energy which is equivalent to Axb.

$$A \times b = 3600.M.fmat.x \qquad \ldots\ldots\ldots\ldots\ldots\ldots\ldots\ldots \quad (4-1)$$

The 3600 in equation 4-1 is used for unit conversion. The equivalent hardness indicators, $3600.M.f_{mat}.x$, for each size class determined using the parameters obtained from the size dependent breakage model are presented in Table 4-4.

Table 4-4: Ore breakage parameters for the tested UG2 rock types determined by fitting the breakage data to the size dependent model

		Particle mean size x (mm)			
		14.5	20.6	28.9	41.1
Ore type	Sampling method	Ore breakage indicator (3600.M.f_{mat}.x)			
Chromitite	Particle Selection	386	341	319	264
	Cut Core	173	-	148	-
Pyroxenite	Particle Selection	112	96	90	127
	Cut Core	59	-	59	-
Spotted	Particle Selection	137	166	124	130
Anorthosite	Cut Core	82	-	78	-
Mottled	Particle Selection	147	133	90	111
Anorthosite	Cut Core	65	-	62	-

The samples from the particle selection method have higher ore breakage indicators than cut core samples for all the rock types tested as presented in Table 4-4. This shows that RoM ore stockpile material offer less resistance to impact breakage. Table 4-4 also shows that breakage indicator values for chromitite particles obtained using both methods were higher than the respective breakage indicators obtained for the other rocks. This illustrates that chromitite offers the least resistance to breakage. Mottled anorthosite and spotted anorthosite were found to have breakage indicators which were lower than chromitite but higher than pyroxenite. Pyroxenite gave the least values for the breakage indicators showing it has the highest resistance to impact breakage. These findings are consistent with the results obtained from the data analysis using the t_{10} breakage model.

Table 4-4 also reveals the effect of parent particle size on the resistance to impact breakage. The ore breakage indicators presented in Table 4-4 tend to decrease with an increase in the parent particle size. This shows that particles become more resistant to impact breakage as the initial particle size increases. However, for pyroxenite, spotted and mottled anorthosite, the indicator decreases between the particle sizes 14 to 28.6 mm but then increases for 41.1 mm. The exhibited trend was not expected. As the particle size decrease, the size and number of flaws decrease (Tavares & King, 1998) as also indicated in the tomographic scans in section 4.4.1. The decrease of the size and number of flaws in the particle result in an increase in particle strength (Schönert, 1991). Thus, most ores show an increase in the resistance to impact breakage ("Axb" decreases) with decrease in the initial particle size as

evidenced by Banini (2000). However, the findings in this study were similar to observations by Shi and Kojovic (2007) presented in Figure 2-12. Shi and Kojovic (2007) showed that for some ores such as lead ore in their work, the Axb values tend to have a general decreasing trend with increase in initial particle size. Figure 2-12 also shows that although Axb values have a general trend, either increasing or decreasing, the values fluctuates with an increase in parent particle size. This could explain the observed trend in Table 4-4 as the tests were carried out at a narrow initial particle size compared to the range tested by Shi and Kojovic (2007).

4.7 Summary of the key findings

The following is a summary of key results from the ore breakage characterisation of UG2 RoM stockpile and cut drill core particles using the RBT:

- Mineralogical analysis of the UG2 samples revealed that chromitite tested consisted predominantly of fine, discrete, rounded chromite grains cemented together by small amounts of plagioclase. Pyroxenite specimens were found to contain mainly granular orthopyroxene, interstitial plagioclase and clinopyroxene. Spotted anorthosite specimens tested were composed primarily of plagioclase with orthopyroxene crystals forming isolated interstitial “spots” creating a poikilitic texture. The analysis of UG2 mottled anorthosite showed that the particles were made up mainly of plagioclase.
- Particles sourced from the RoM ore stockpile were consistently found to break into a finer progeny compared to cut drill core samples. This was demonstrated by the finer progeny size distributions and higher degrees of breakage for the stockpile material for all the rock types tested.
- Tomographic scans revealed the presence of cracks in large (-31.5 + 26.5 mm) RoM ore particles. No visible cracks were seen in the large cut core particle. In addition, there were no cracks observed in the small particles (-16.0 + 13.2 mm) for both the grab samples from RoM ore and cut drill core particles.
- The ore hardness parameters were determined from fitting the breakage data to standard impact breakage characterisation models (t_{10} breakage and size dependent breakage model). The t_{10} breakage model fitted well to the breakage data for all rock types tested with the least R^2 value obtained of 0.950 for chromitite RoM samples. The parameters, A and b, were extracted and used to

determine the ore hardness indicator (Axb). Samples obtained via the particle selection method were found to have higher Axb values thus less resistance to breakage compared to the cut drill core samples. The Axb values for RoM stockpile particles (in decreasing order) of chromitite, spotted anorthosite, mottled anorthosite and pyroxenite were found to be 325, 138, 115 and 108 respectively. A similar trend was observed for the aforementioned rock types tested sourced via the cut core method. Using the ore hardness classes presented by Napier-Munn et al (1999), UG2 chromitite, spotted anorthosite, mottled anorthosite and pyroxenite were thus classified as very soft, soft to very soft, soft to very soft and medium to soft respectively.

- The size dependent breakage model fitted to the breakage data showed an improved fit, compared to the t_{10} breakage model, with a minimum R^2 value obtained of 0.985 for chromitite RoM samples. An equivalent to the Axb for the t_{10} breakage model, $3600.M.f_{mat}.x$, was determined for each size class for the rock types tested. The breakage indicators for size classes tested showed dependency on the initial particle size. The indicators decrease with an increase in the parent particle size. However, for pyroxenite, spotted and mottled anorthosite, the indicator decreases between the particle sizes 14 to 28.6 mm but then increases for 41.1 mm

5. CONCLUSIONS AND RECOMMENDATIONS

Overview

In this chapter, the thesis objectives are assessed and appropriate conclusions are drawn from the work. A number of recommendations for future work have also been suggested.

5.1 Conclusions

The scope of work in this thesis was guided by the hypothesis which postulated that UG2 rock particles sourced from a RoM ore stockpile break more readily to produce a finer product than cut drill core samples from the shaft supplying the same stockpile material.

To interrogate this hypothesis, ore breakage characterisation tests were conducted using the RBT on the UG2 rock particles sourced from a RoM ore stockpile and cut drill core samples. Mineralogical analyses were also done to determine the mineralogical composition, texture and presence of cracks in the samples. The results of this work support the proposed hypothesis as shown by the following conclusions from the research objectives:

5.1.1 Mineralogical composition and texture of UG2 samples

The abundant rock types namely chromitite, pyroxenite, spotted anorthosite and mottled anorthosite from the UG2 RoM ore and drill core samples from Karee 3 shaft in the Marikana region were grouped based on the visible lithological characteristics such as colour, texture, grain size and composition. The analysis done with Leica EZ4D optical microscope and QEMSCAN 650F confirmed the mineralogical differences in the UG2 chromitite, pyroxenite, spotted anorthosite and mottled anorthosite samples. Chromitite comprised of predominantly fine, discrete, rounded chromite grains cemented mainly by plagioclase whilst pyroxenite contained mostly granular orthopyroxene, interstitial plagioclase and clinopyroxene. Spotted and mottled anorthosite samples were found to be coarse grained consisting mainly of plagioclase. In addition, spotted anorthosite was found to contain orthopyroxene crystals forming isolated interstitial “spots” within the plagioclase. Mottled anorthosite sample was found to have negligible amounts of pyroxene.

5.1.2 Progeny particle size distributions and the degrees of breakage

The progeny particle size distributions and the degrees of breakage of UG2 chromitite, pyroxenite, spotted anorthosite and mottled anorthosite sourced from RoM stockpile and cut drill cores subjected to impact breakage using the RBT were compared and the following conclusions were made:

(a) The particle selection and cut core methods

The samples obtained from RoM stockpile were found to break into a finer product compared to cut drill core samples subjected to the same input energies for all the rock types tested. Tomographic scans for RoM stockpile particles revealed the presence of cracks induced through pre-weakening processes such as blasting and transportation. These flaws act as stress raisers when the particle is under load resulting in the generation of fine fragments. No cracks were visible in the tomographic scans of cut drill core samples.

(b) Main UG2 rock types

It was found that UG2 chromitite particles fragment into finer progeny particles compared to the other rock types evidenced at the energy levels tested. As shown from the mineralogical analysis, chromitite consists mainly of fine-grained chromite loosely cemented in orthopyroxene and plagioclase matrix which easily fragments when stress is applied. There is no significant difference between the fineness of the breakage products for mottled and spotted anorthosite despite the textural differences for the anorthositic rocks. Pyroxenite produced a coarser product compared to the other rock types across all energy levels tested. This was attributed to a complex texture found in the pyroxenite resulting from the granular orthopyroxene and interstitial plagioclase and clinopyroxene. The orthopyroxene grains were also found to be larger than the chromite grains in chromitite particles.

(c) Effect of energy input

For the energy levels tested, increasing the specific input energy resulted in finer progeny particle size distributions and higher degrees of breakage for all rock types. When the input energy is increased, the stressing intensity in the particles also increases. This intensifies the propagation of cracks in the particles resulting in fracturing into smaller fragments.

5.1.3 Relative hardness parameters of the different rock types

The t_{10} breakage model and size dependent model were fitted to the breakage data of the UG2 chromitite, pyroxenite, spotted anorthosite and mottled anorthosite particles sourced from RoM ore stockpile and cut drill core particles. From the model fittings, ore hardness parameters were determined. As expected, the breakage models confirmed the exponential relationship between the degree of breakage and the input energy. This reflects that increasing energy inputs results in higher degrees of breakage until no further significant increase occurs. Furthermore, the following conclusions were also drawn from the hardness parameters.

(a) The particle selection and cut core methods

The parameters, A and b, were extracted from the t_{10} breakage model fittings and used to determine the ore hardness indicator (Axb). The maximum degree of breakage, A, obtained from a single impact of the RoM stockpile particles were consistently found to be higher than cut drill core samples for each rock type tested. Also, it was found that RoM ore particles showed less resistance to deformation prior to fracture, b, than cut drill core particles.

In addition, the RoM ore particles offered less resistance to impact breakage shown by higher Axb values as compared to the cut drill core samples. As previously mentioned, RoM ore particles contained more microflaws as shown in the tomographic scans induced through pre-weakening processes which makes the particles breaks more readily. Consequently, more energy is required to break the cut core particles to a similar progeny size distribution as RoM ore particles. This highlights that this consideration should be applied when designing comminution circuits to process ore obtained using rock cutting technology to ensure that the devices are capable of meeting grind and throughput targets.

The equivalent hardness indicators, $3600.M.f_{mat}.x$, for each size class determined using the parameters obtained from the size dependent breakage model decrease with an increase in the parent particle size. This shows that particles become more resistant to impact breakage as the initial particle size increases. However, for pyroxenite, spotted and mottled anorthosite, the indicator decreases between the particle sizes 14 to 28.6 mm but then increases for 41.1 mm.

(b) Main UG2 rock types

It was found that UG2 chromitite particles exhibit the highest amenability to fragmentation via impact, followed by spotted and mottled anorthosite. Pyroxenite has the highest resistance to impact breakage. UG2 chromitite, spotted anorthosite, mottled anorthosite and pyroxenite were classified as very soft, soft to very soft, soft to very soft and medium to soft respectively according to ore hardness classes presented by Napier-Munn et al (1999). The differences in the breakage properties of the main UG2 rock types were attributed to the mineralogical difference of the samples tested.

5.2 Recommendations

The following recommendations are proposed for future test work based on the outcomes of this study:

- The mineralogical analysis with the Leica EZ4D optical microscope and QEMSCAN 650F was done on limited samples of UG2 chromitite, pyroxenite, spotted anorthosite and mottled anorthosite particles. Further investigation on a larger sample of each rock type is required including other waste rocks such as norite, to conclusively confirm the observed mineralogical and textural composition. This will be important in predicting and explaining the breakage properties of the different rocks.
- Chromitite particles tend to break along the chromite grain boundaries as shown by the bimodal progeny particle size distributions indicating preferential breakage. Unlike for pyroxenite spotted anorthosite and mottled anorthosite, the progeny particle size distributions were smooth curves without kinks suggesting random fracture. Further analysis exploring the breakage characteristics and the propagation of cracks for different mode of breakage in these particles is required.
- Impact breakage tests and tomographic analyses should be done on crushed rock particles of similar size classes to tested grab samples from RoM stock pile. This enables the investigation of the amenability of crushed ore particles to impact breakage and whether there is any significant change in crack density from RoM samples.

REFERENCES

Anderson, T.L., 2005. *Fracture Mechanics: Fundamentals and Applications,*CRC press: 640 -641.

Ashby, M.F., Shercliff, H. & Cebon, D. 2007. *Materials: engineering, science, processing and design*. Amsterdam: Elsevier: 166-167.

Ashwal, L.D. 1993. *Anorthosites* (Vol. 21). Springer Science & Business Media.

Banini, G.A. 2000. *An integrated description of rock breakage in comminution machines*. PhD Thesis, JKMRC, University of Queensland, Australia.

Baum, W. 2013. *Ore characterization, process mineralogy and lab automation a roadmap for future mining*. *Minerals Engineering*. 60: 69 -73.

Bbosa, L.S. 2007. *Measurement of impact breakage properties of ore particles using a series of devices.* Postgraduate thesis, Centre for Minerals Research, Department of Chemical Engineering, University of Cape Town.

Bbosa, L., Powell, M.S. & Cloete, T.J. 2006. *An investigation of impact breakage of rocks using the split Hopkinson pressure bar*. Journal of the South African Institute of Mining and Metallurgy, 106(4): 291-296.

Bearman, R.A., Briggs, C.A. & Kojovic, T. 1997. *The application of rock mechanics parameters to the prediction of comminution behaviour*. Minerals Engineering, 1997. 10(3): 255-264.

Bonfils, B. & Powell, M.S. 2013. *Developments in Incremental Rock Breakage Testing Methodologies and Modelling. ESCC2013: 13th European Symposium on Comminution and Classification*: 165–168.

Bourgeois, F.S. & Banini, G. A. 2002. *A portable load cell for in-situ ore impact breakage testing.* International Journal of Mineral Processing. 65(1):31–54.

Bueno, M.P., Kojovic, T., Powell, M.S. & Shi, F. 2013. Multi-component AG/SAG mill model. *Minerals Engineering*. 43-44:12–21.

Cawthorn, R.G. 1999. The platinum and palladium resources of the Bushveld Complex. *South African Journal of Science*. 95: 481–489.

Chernet, T. & Marmo, J. 2003. Direct comparison on mechanical and digital size analyses of Kemi Chromite , Finland. *Minerals Engineering*. 16:1245–1249.

Clarke, B., Uken, R. & Reinhardt, J. 2005. Lithos Structural and compositional constraints on the emplacement of the Bushveld Complex , South Africa. *LITHOS*. 111(1-2): 21–36.

Cleary, P.W. 1998. Predicting charge motion, power draw, segregation and wear in ball mills using discrete element methods. *Minerals Engineering*. 11(11):1061–1080.

Cohen, H.E. 1983. Energy usage in mineral processing. *Trans. I.M.M.* 92:C160–C164.

Condie, K.C. 1992. *Proterozoic crustal evolution*. Elsevier Publishing Co., Amsterdam: 537.

Crabtree, D.D., Kinasevich, R.S., Mular, A.L., Meloy, T.P. & Fuerstenau, D.W. 1964. Mechanisms of size reduction in comminution systems. Part I. Impact, abrasion and chipping grinding. *Transaction of the American Institute of Mining, Metallurgical, and Petroleum Engineers*. 229: 201–206.

Cramer, L.A. 2001. The Extractive Metallurgy of South Africa ' s Platinum Ores. Jom, 53(10): 14-18.

Cropp, A. & Goodall, W. 2013. The influence of rock texture on mineral processing. *Min Assist:* 1–9.

Van Eck, M. 2007. Investigating the products from different modes of particle breakage testing. University of Cape Town, South Africa.

Esen, S., Rosa, D. La, Dance, A., Valery, W. & Jankovic, A. 2007. Integration and Optimisation of Blasting and Comminution Processes. In *EXPLO Conference*. Wollongong, NSW: The Australasian Institute of Mining and Metallurgy. 1–10.

Frew, D.J., Forrestal, M.J. & Chen, W. 2001. A split Hopkinson pressure bar technique to determine compressive stress-strain data for rock materials. *Experimental Mechanics*. 41(1):40–46.

Fuerstenau, D.W., Lutch, J.J. & De, A. 1999. The effect of ball size on the energy efficiency of hybrid high-pressure roll mill/ball mill grinding. *Powder Technology*.

105(1-3): 199–204.

Garcia, D., Lin, C.L. & Miller, J.D. 2009. Quantitative analysis of grain boundary fracture in the breakage of single multiphase particles using X-ray microtomography procedures. *Minerals Engineering*. 22(3):236–243.

Hahne, R., Pålsson, B.I. & Samskog, P.O. 2003. Ore characterisation for—and simulation of—primary autogenous grinding. *Minerals Engineering*. 16(1):13–19.

Hartley, J.., Prisbrey, K.. & Wick, O.J. 1978. Chemical additives for ore grinding: How effective are they?. *Engineering & Mining Journal*. 105.

Hoffman, J.W. & Beer, F.C.D.E. 2011. Characteristics of the Micro-Focus X-ray Tomography Facility (MIXRAD) at Necsa in South Africa. *18th World Conference on Nondestructive Testing*: 16–20.

Hopkinson, B. 1914. A method of measuring the pressure produced in the detonation of high explosives or by the impact of bullets. *Phil. Trans. R Soc. Lond*. A213. 437-456

Huang, J., Xu, S. & Hu, S. 2014. Influence of particle breakage on the dynamic compression responses of brittle granular materials. *Mechanics of Materials*. 68:15–28.

Inglis, C.E. 1913. Stresses in a Plate Due to Presence of Cracks and Sharp Corners. *Transaction of the Institution of Naval Architects*. 55: 219–230.

JKTech Rotary Breakage Tester. 2012. Breakage test procedure. Section 9 Machine manual. *Published by JKTech*

Kapur, P.C., Pande, D. & Fuerstenau, D.W. 1997. Analysis of single-particle breakage by impact grinding. 49: 223–236.

King, R.P. 2001. *Modeling and Simulation of Mineral Processing Systems*. Oxford: Butterworth-Heinemann.

Klerk, W.J. de. 1995. Mineralogy Petrology Textures exhibited by feldspars in the Giant Mottled Anorthosite (GMA) of the Bastard unit in the Upper Critical Zone , Western Bushveld Complex. *Mineralogy and Petrology*. 54: 25–34.

Kojovic, T., Shi, F., Larbi-Bram, S. & Manlapig, E. 2008. Julius Kruttschnitt rotary

breakage tester (JKRBT) – any ore, any mine. In *MetPlant (The Australasian Institute of Mining and Metallurgy: Melbourne):* 91–104.

Krogh, S.R. 1980. Crushing characteristics. *Powder Technology*. 27(2): 171–181.

Larbi-Bram, S. 2009. A Study of Ore Breakage Characterization for AG/SAG Mill Modelling. University of Queensland.

Lee, C.A. 1996. A review of Mineralization in the Bushveld Complex and some other Layered Intrusions. *Elseveir Science*: 103–145.

Leung, K. 1987. An energy based ore specific model for autogenous aand semi-autogenous grinding. University of Queensland, Brisbane, Australia.

Liddell, K.S., McRae, L.B. & Dunne, R.C. 1986. *Process routes for the beneficiation of Noble metals from Merensky and UG2 ores*.

Mainza, A.N. & Powell, M.S. 2006. RoM Ball Mills - A comparison with AG/ SAG Milling. In *Proceedings of International Autogenous and Semi-Autogenous Grinding Technology (2)*: 314–325.

Mathez, E.A. & Mey, J.L. 2005. Character of the UG2 Chromitite and Host Rocks and Petrogenesis of Its Pegmatoidal Footwall, Northeastern Bushveld Complex. *Economic Geology*. 100: 1617–1630.

Mondal, S.K. & Mathez, E.A. 2006. Origin of the UG2 chromitite layer , Bushveld Complex. *Journal of Petrology*. 48(3): 495–510.

Morrell, S., Johnson, G. & Revy, T. 1991. A comparison through observation and simulation of the Power Utilization and Perfomance of two Dissimilar Comminution Plants. In *Proc 4th Mill Operators Conference*. Tasmania: Australasian Institute of Mining and Metallurgy.

Morrell, S., Finch, W.M., Kojovic, T. & Jr, H.D. 1996. Modelling and simulation of large diameter autogeneous and semi-autogeneous mills. 45: 289–300.

Morrison, R.D. & Richardson, J.M. 2002. JKSimMet: A simulator for analysis, optimisation and design of comminution circuits. In *Mineral Processing Plant Design Practice and Control*. A.L. Mular, D.N. Halbe, & D.J. Barratt, Eds. Vancouver, B.C.,

Canada: SME: Society for Mining, Metallurgy and Exploration. 442–460.

Napier-Munn, T. 2014. Is progress in energy-efficient comminution doomed? 73:1–6.

Napier-Munn, T.J., Morell, S., Morrison, R.D. & Kojovic, T. 1996. *Minerals Comminution Circuits: Their operation and optimization*. JKMRC. Brisbane, Australia:

Narayanan, S.. 1985. Development of a Laboratory Single Particle Technique and its Application to Ball Mill Modelling and Scaleup. University of Queensland, Brisbane, Australia.

Pauw, O.G. & Maré, M.S. 1988. The determination of optimum impact-breakage routes for an ore. *Powder Technology*. 54(1):3–13.

Penberthy, C.J. 2001. The effect of mineralogical variation in the UG2 chromitite on recovery of platinumgroup elements. University of Pretoria.

Petruk, W. 2000. *Applied Mineralogy in the Mining Industry*. Oxford: Elsevier Science.

Radziszewski, P. & Laplante, A. 2006. Exploring the effect of friction losses on drop weight breakage results. *AMIRA Project P9N Mineral Processing 5th P9N Technical Report*. 42–49.

Rule, C. & Schouwstra, R.P. 2011. Process mineralogy delivering significant value at Anglo Platinum concentrator operations. *10th International Congress for Applied Mineralogy*. (August):1–5.

Sahoo, R. 2006. Review: An investigation of single particle breakage tests for coal handling system of the gladstone port. *Powder Technology*. 161(2):158–167.

Schönert, K. 2004. Breakage of spheres and circular discs. *Powder Technology*. 143-144:2–18.

Schouwstra, R.P. & Smit, a. J. 2011. Developments in mineralogical techniques - What about mineralogists? *Minerals Engineering*. 24(12):1224–1228.

Schouwstra, R.P., Kinloch, E.D. & Lee, C.A. 2000. A Short Geological Review of the Bushveld Complex. *Platinum Metals Review*. 44(2):33–39.

Schwarz, S. & Richardson, J. 2013. Modelling and simulation of mineral processing

circuits using JKSimMet and JKSimFloat. *2013 SME Annual Meeting & Exhibit (SME 2013) and CMA 115th National Western Mining Conference.* 615 – 622. Available: http://www.ceecthefuture.org/wp-content/uploads/2013/12/Richardson-schwarz.pdf.

Shi, F. & Kojovic, T. 2007. Validation of a model for impact breakage incorporating particle size effect. *International Journal of Mineral Processing*. 82(3):156–163.

Shi, F. & Kojovic, T. 2011. Comparison of impact breakage characterisation methods between the JK Rotary Breakage Tester and drop weight tester. In *SAG 2011 Conference*. V. Paper 101. Vancouver, Canada.

Shi, F., Kojovic, T., Larbi-Bram, S. & Manlapig, E. 2006. Development of a new breakage characterisation device. *AMIRA Project P9N Mineral Processing:5th technical report*. 55–66.

Shi, F., Kojovic, T., Larbi-bram, S. & Manlapig, E. 2009. Development of a rapid particle breakage characterisation device – The JKRBT. *Minerals Engineering*. 22(7-8):602–612.

Stamboliadis, E.T. 2008. The evolution of a mineral liberation model by the repetition of a simple random breakage pattern. *Minerals Engineering*. 21:213–223.

Steyn, J.J. 2012. Developing a framework for the design of the milling and rougher circuits for a platinum-bearing UG2 ore. University of Cape Town.

Tavares, L.. 2004. Optimum routes for particle breakage by impact. *Powder Technology*. 142(2-3):81–91.

Tavares, L.M. 2007. Breakage of Single Particles: Quasi-Static. In *Particle Breakage: Handbook of PowderTechnology*. 12. A.D. Salman, M. Ghadiri, & M.J. Hounslow, Eds. Amsterdam: Elsevier Science & Technology Books. 3–68.

Tavares, L.. & King, R.. 1998. Single-particle fracture under impact loading. *International Journal of Mineral Processing*. 54(1):1–28.

Tavares, L.. & King, R.. 2002. Modeling of particle fracture by repeated impacts using continuum damage mechanics. *Powder Technology*. 123(2-3):138–146.

Tavares, L.M. & King, R.P. 2004. Measurement of the load–deformation response

from impact-breakage of particles. *International Journal of Mineral Processing*. 74:S267–S277.

Tuzcu, E.T., Dhawan, N. & Rajamani, R.K. 2012. Coarse particle fracture with the ultrafast load cell. 28(4).

Umucu, Y., Deniz, V. & Unal, N. 2013. An evaluation of a modified product size distribution model based on t-family curves for three different crushers. *Physicochemical Problems of Mineral Processing*. 49(2):473–480.

Vassiliev, P. V, Ledoux, H. & Gold, C. 2008. Modeling Ore Textures and Mineral Liberation Using 3D Voronoi Diagrams. In *International conference on Numerical geometry, grid generation and scientific computing*. V.A. Garanzha, Y.G. Evtushenko, B.K. Soni, & N.P. Weatherhill, Eds. Moscow. 220–225.

Vogel, L. & Peukert, W. 2003. Breakage behaviour of different materials—construction of a mastercurve for the breakage probability. *Powder Technology*. 129(1-3):101–110.

Vogel, L. & Peukert, W. 2004. Determination of material properties relevant to grinding by practicable labscale milling tests. *International Journal of Mineral Processing*. 74:S329–S338.

Vogel, L. & Peukert, W. 2005. From single particle impact behaviour to modelling of impact mills. *Chemical Engineering Science*. 60(18):5164–5176.

Williams, N.R. & Holtzhausen, S. 2001. The impact of ore characterization and blending on metallurgical plant performance:437–446.

Wills, B.A. & Napier-Munn, T. 2006. Mineral Processing Technology. 7th Edition. Elsevier Science & Technology Books.

Xiao, Z. & Laplante, a. R. 2004. Characterizing and recovering the platinum group minerals - A review. *Minerals Engineering*. 17:961–979.

Xu, W., Dhawan, N., Lin, C.L. & Miller, J.D. 2013. Further study of grain boundary fracture in the breakage of single multiphase particles using X-ray microtomography procedures. *Minerals Engineering*. 46-47(3):89–94.

Yahyaei, M., Hilden, M., Shi, F., Liu, L., Ballatyne, G. & Palaniandy, S. n.d.

Comminution. In *Production, Handling and Characterization of Particulate Materials*. 157–200.

Zuo, W. & Shi, F. 2015. A t 10 -based method for evaluation of ore pre-weakening and energy reduction. *Minerals Engineering*. 79:212–219.

Zuo, W. & Shi, F. 2016. Ore impact breakage characterisation using mixed particles in wide size range. *Minerals Engineering*. 86(2016):96–103.

A. APPENDIX A

1.1 Raw Data

Table A-1: Breakage data for UG2 Chromitite RoM ore sample run 1 showing the mass retained on the standard screens

Size (mm)	45.0 x 37.5			31.5 x 26.5			22.4 x 19.0			16.0 x13.2		
rpm	938	1408	2606	1408	2606	3915	1408	2606	3915	1408	2606	3915
E_{cs} (kWh/t)	0.10	0.25	1.00	0.25	1.00	2.50	0.25	1.00	2.50	0.25	1.00	2.50
No. of particles	30			30			30			30		
Initial mass	5416.1	5193.6	5024.1	1909.7	1758.3	1891.1	624.6	726.1	678.3	212.1	237.1	189
After breakage	5396.2	5086.7	4885.3	1899.8	1750.4	1855.3	620.7	711.6	665.2	211.2	236.8	186.2
45.0	0	0	0	0	0	0	0	0	0	0.0	0.0	0.0
37.5	132.4	0	0	0	0	0	0	0	0	0.0	0.0	0.0
26.5	502.2	72.7	0	0	0	0	0	0	0	0.0	0.0	0.0
19.0	970.5	328.3	27.2	64.8	0	0	0	0	0	0.0	0.0	0.0
13.2	801.6	471.5	107.5	120.9	19	0	13.1	0	0	0.0	0.0	0.0
9.50	638.2	483.5	159.6	149.2	38	0	38.6	7.1	0	9.3	0.0	0.0
6.70	400.9	488.6	215.1	136.7	63.7	8.9	52.1	7.5	0	15.3	0.5	0.0
4.75	388.5	436.8	268.9	176.8	76.4	16.8	64.6	25.3	1.1	15.6	3.2	0.0
3.35	216.4	343	237.4	120.2	74.9	29.1	54.4	29.9	4.6	14.7	6.3	0.5
2.36	150.8	244.7	200.7	98	71	38.6	39.7	30.6	8.4	12.6	5.7	0.8
1.70	89	177.1	174.6	61.4	61.3	33.9	28.8	24.8	7.4	10.2	5.1	1.6
1.18	69.3	137.1	141	55.7	54.2	35.3	23	23.6	8	8.2	5.6	2.3
0.85	47.3	92.6	103.1	40.6	38.8	28.2	16	17.7	7.3	6.3	4.7	2.1
0.60	55.4	85.3	109.5	48.4	43	30.1	17.1	19.5	8.3	7.1	5.5	2.2
0.425	89.5	95.2	159.6	72	64.4	47.7	22.8	28.3	13.3	10.1	7.5	3.6
0.300	132.3	160.2	330.3	115.7	119.1	108.3	40	48.7	31.4	15.9	15.6	7.5
0.212	205.9	272.5	717	194.3	239.1	237.3	63.4	104	76.2	23.1	32.2	19.1
0.150	193.5	291.9	827.2	186.3	261	322.1	59.7	120.7	114.5	22.3	40.2	30.3
0.106	128.8	279.1	530.5	118.3	239.2	370.6	46.7	92.2	149.1	20.5	44.8	44.0
Pan (-0.106)	179.2	273.5	670.6	136.7	284.6	540.1	49.1	129.2	232.8	19.2	52.8	69.7
Sum (g)	5391.7	4733.6	4979.8	1896	1747.7	1847	629.1	709.1	662.4	210.4	229.7	183.7
Breakage Loss (g)	19.9	106.9	138.8	9.9	7.9	35.8	3.9	14.5	13.1	0.9	0.3	2.8
Loss Breakage (%)	0.367	2.06	2.76	0.52	0.45	1.89	0.62	2.00	1.93	0.42	0.13	1.48
Sieving loss (g)	4.5	353.1	-94.5	3.8	2.7	8.3	-8.4	2.5	2.8	0.8	7.1	2.5
Loss Sieving (%)	0.083	6.942	-1.934	0.200	0.154	0.447	-1.353	0.351	0.421	0.379	2.998	1.343

Table A-2: Breakage data for UG2 Chromitite RoM ore sample run 2 showing the mass retained on the standard screens

Size (mm)	45.0 x 37.5			31.5 x 26.5			22.4 x 19.0			16.0 x13.2		
rpm	938	1408	2606	1408	2606	3915	1408	2606	3915	1408	2606	3915
E_{cs} (kWh/t)	0.10	0.25	1.00	0.25	1.00	2.50	0.25	1.00	2.50	0.25	1.00	2.50
No. of particles	30			30			30			30		
Initial mass	5422.2	5306.7	4916.4	1756.9	2026.2	1816.5	683.9	642.6	664.8	214.8	230.9	214.8
After breakage	5415.2	5291.3	4896.2	1755.1	2006	1790.8	664.1	637.8	658.4	214.6	228.3	213.2
45.0	0	0	0	0	0	0	0	0	0	0.0	0.0	0.0
37.5	680	0	0	0	0	0	0	0	0	0.0	0.0	0.0
26.5	439.3	0	0	0	0	0	0	0	0	0.0	0.0	0.0
19.0	611.9	447.4	49.2	48.9	0	0	0	0	0	0.0	0.0	0.0
13.2	578.8	697	67.2	80.1	38.8	0	8.7	0	0	0.0	0.0	0.0
9.50	614.4	642.6	243.3	195.8	28.4	0	38.7	0	0	8.1	1.9	0.0
6.70	466.4	524.5	264.8	119.1	71.8	0	40	8	2	11.6	0.0	0.0
4.75	291.6	500.9	214.3	170.2	64.1	15.8	84	24.5	3.8	21.5	3.7	0.0
3.35	208.5	320.7	233.7	123.5	75.3	35.2	56.1	20.7	8.2	18.3	7.0	0.8
2.36	134	221.9	189.4	90.3	73.3	44.9	46.6	26.4	11.2	13.5	6.0	1.3
1.70	86.6	148.2	155.8	62.8	61.4	38.7	28.2	19.8	10.5	9.2	5.3	1.7
1.18	71.1	118.6	137.4	51.9	61.4	41.6	26.1	20.6	11	8.1	5.0	2.0
0.85	51.9	85	98.1	38.4	44.4	31.4	19.2	15.3	9.2	5.5	4.4	2.0
0.60	59.8	91.2	107.7	42.8	50.3	32.3	20.8	16.5	9.7	5.8	4.6	2.4
0.425	97.2	128.2	163.2	65.3	80.4	45.5	27.9	23.7	14.3	7.7	6.3	3.2
0.300	190.9	215.4	320.9	108.1	156.6	93.3	38	43	32.4	13.2	13.9	6.7
0.212	282.5	287.3	620.5	177	291.1	251.2	71.9	92.1	76.1	26.7	30.7	21.8
0.150	230.1	352	780.6	156.5	309.6	348.2	71.6	111.4	112.2	26.6	39.7	40.5
0.106	164.2	226	576.9	103.7	278.1	309.2	46.1	96.1	139.8	17.7	43.3	44.6
Pan (-0.106)	151.9	280.9	661.8	118.8	319.2	499.3	53.3	118.6	216.5	19.8	53.2	86.2
Sum (g)	5411.1	5287.8	4884.8	1753.2	2004.2	1786.6	677.2	636.7	656.9	213.3	225	213.2

Breakage Loss (g)	7	15.4	20.2	1.8	20.2	25.7	19.8	4.8	6.4	0.2	2.6	1.6
Loss Breakage (%)	0.13	0.29	0.41	0.10	1.00	1.41	2.90	0.75	0.96	0.09	1.13	0.74
Sieving loss (g)	4.1	3.5	11.4	1.9	1.8	4.2	-13.1	1.1	1.5	1.3	3.3	0
Loss Sieving (%)	0.08	0.07	0.23	0.11	0.09	0.23	-1.97	0.17	0.23	0.61	1.45	0.00

Table A-3: Breakage data for UG2 Chromitite RoM ore sample run 3 showing the mass retained on the standard screens

Size (mm)	45.0 x 37.5			31.5 x 26.5			22.4 x 19.0			16.0 x13.2		
rpm	938	1408	2606	1408	2606	3915	1408	2606	3915	1408	2606	3915
E_{cs} (kWh/t)	0.10	0.25	1.00	0.25	1.00	2.50	0.25	1.00	2.50	0.25	1.00	2.50
No. of particles	30			30			30			30		
Initial mass	4858.9	4877.8	4948.7	1768.4	1818	1801	600	646.1	656.4	233.4	235.4	240.6
After breakage	4853.2	4865.3	4927.4	1762.5	1804.9	1786.5	599.1	640.1	651.8	232.2	233.3	236.5
45.0		0	0	0	0	0	0	0	0	0.0		0.0
37.5	90.9	0	0	0	0	0	0	0	0	0.0	0.0	0.0
26.5	380	149	0	0	0	0	0	0	0	0.0	0.0	0.0
19.0	569.3	336.7	41.5	91.8	0	0	0	0	0	0.0	0.0	0.0
13.2	842.1	494.6	99.7	94.8	4.7	0	10.3	0	0	0.0	0.0	0.0
9.50	617.6	526.2	238	177.1	15.7	0	33	0	0	5.1	0.0	0.0
6.70	418.6	475.4	232	158	48.7	13.2	45.3	9.9	2.7	20.9	0.0	0.0
4.75	391.1	346	293.2	155.9	86.9	14.7	54.8	13.4	2.5	18.0	1.0	0.4
3.35	214.6	269.7	247.9	116.8	84.7	23.3	65.3	22	6.6	17.4	4.8	0.9
2.36	139.4	207.5	195.9	77.7	74.9	32.5	44.7	22.3	10	16.1	7.9	2.8
1.70	89.6	139.5	163.1	57.8	57.6	34	36.4	18.6	9.7	10.6	7.6	3.8
1.18	72.6	114.9	138.6	44.4	53.1	36.2	22.9	17.4	11.4	8.8	7.3	4.0
0.85	52.7	82.4	99.7	31.8	39.6	28.5	18.9	14.2	9.6	6.1	5.8	2.8
0.60	57.2	93.8	108.7	34.6	41.6	30.2	13.3	16.1	10.2	6.2	6.1	3.1
0.425	76.7	144.3	154.1	54.5	57	44.5	19.3	24.2	13.5	9.2	9.3	4.4
0.300	134	243.4	290.9	106.7	112.5	99.4	45.9	46	25.9	14.6	16.0	9.2
0.212	235.7	373.5	705.7	170.4	281.6	240.5	61.2	90.4	80.8	26.3	36.0	24.2
0.150	201.4	345.1	848.8	158.9	313.7	327	58.8	111.4	125.1	26.5	43.1	41.7
0.106	127.3	258.5	461.2	123.9	225.4	353.7	54.8	121	146.2	23.9	37.5	55.5
Pan (-0.106)	139.3	259.9	603.4	106.7	305.6	506.1	38.2	112.7	195.7	21.7	49.7	82.6
Sum (g)	4850.1	4860.4	4922.4	1761.8	1803.3	1783.8	623.1	639.6	649.9	231.4	232.1	235.4

Breakage Loss (g)	5.7	12.5	21.3	5.9	13.1	14.5	0.9	6	4.6	1.2	2.1	4.1
Loss Breakage (%)	0.12	0.26	0.43	0.33	0.72	0.81	0.15	0.93	0.70	0.51	0.89	1.70
Sieving loss (g)	3.1	4.9	5	0.7	1.6	2.7	-24	0.5	1.9	0.8	1.2	1.1
Loss Sieving (%)	0.06	0.10	0.10	0.04	0.09	0.15	-4.01	0.08	0.29	0.34	0.51	0.47

Table A-4: Breakage data for UG2 Chromitite drill core sample run 1 showing the mass retained on the standard screens

Size (mm)	45.0 x 37.5			31.5 x 26.5			22.4 x 19.0			16.0 x13.2		
rpm	938	1408	2606	1408	2606	3915	1408	2606	3915	1408	2606	3915
E_{cs} (kWh/t)	0.10	0.25	1.00	0.25	1.00	2.50	0.25	1.00	2.50	0.25	1.00	2.50
No. of particles	30			30			30			30		
Initial mass				1729.3	1758.9					268.1	270	249.3
After breakage				1722.5	1747.7					264	265.2	243.7
45.0				0	0					0.0	0.0	0.0
37.5				0	0					0.0	0.0	0.0
26.5				0	0					0.0	0.0	0.0
19.0				342.5	17.9					0.0	0.0	0.0
13.2				295.8	88.9					50.4	0.0	0.0
9.50				173.8	101.4					49.0	11.5	0.0
6.70				145.9	124.8					39.0	14.4	3.5
4.75				95.1	85.4					22.8	14.3	3.9
3.35				75.4	87.1					18.5	12.7	7.8
2.36				54.8	68.9					12.0	8.3	9.2
1.70				38.8	53.3					8.0	7.4	5.9
1.18				30.1	44.1					5.7	6.5	6.0
0.85				19.9	28					4.1	4.4	4.2
0.60				21.3	28.9					4.0	5.1	3.9
0.425				30.9	41.8					5.7	7.6	5.1
0.300				52.9	85.3					9.9	15.1	10.8
0.212				102.1	210.1					16.3	34.9	24.8
0.150				93.2	245.3					16.3	41.2	37.4
0.106				64.3	195.9					14.9	32.4	47.2
Pan (-0.106)				82.3	236.9					15.0	45.2	69.8
Sum (g)				1719.1	1744					291.6	261	239.5

Breakage Loss (g)				6.8	11.2					4.1	4.8	5.6
Loss Breakage (%)				0.39	0.64					1.53	1.78	2.25
Sieving loss (g)				3.4	3.7					-27.6	4.2	4.2
Loss Sieving (%)				0.197	0.212					-10.455	1.584	1.723

Table A-5: Breakage data for UG2 pyroxenite RoM ore sample run 1 showing the mass retained on the standard screens

Size (mm)	45.0 x 37.5			31.5 x 26.5			22.4 x 19.0			16.0 x13.2		
rpm	938	1408	2606	1408	2606	3915	1408	2606	3915	1408	2606	3915
E_{cs} (kWh/t)	0.10	0.25	1.00	0.25	1.00	2.50	0.25	1.00	2.50	0.25	1.00	2.50
No. of particles	30			30			30			30		
Initial mass	2590.4	2669.7	2752.7	1559.3	1429.9	1509	505.3	549.2	519.2	189.8	195.8	245.6
After breakage	2585	2666.6	2745.1	1555.2	1423.7	1486.6	503.9	547.5	514.1	188.5	191	242.2
45.0	0	0	0	0	0	0	0	0	0	0.0	0.0	0.0
37.5	89.6	0	0	0	0	0	0	0	0	0.0	0.0	0.0
26.5	638.7	525.7	62.2	103.9	0	0	0	0	0	0.0	0.0	0.0
19.0	538.8	424.4	116.1	298.4	51.3	0	21.7	0	0	0.0	0.0	0.0
13.2	344.9	337.2	196.3	269.8	125.8	45.8	58.7	22.3	0	5.9	0.0	0.0
9.50	231.7	305.7	221.5	185.1	123.9	72.3	99.7	28.1	4.8	23.7	4.7	0.0
6.70	180.3	184.2	243.4	134.1	166.7	60	76.8	39.8	15.7	23.8	1.9	2.0
4.75	108.1	173.5	167.4	126.1	136.4	99.2	55.5	43.1	24.6	19.6	13.4	8.7
3.35	76.6	115.5	177.2	71.4	112.6	88.1	33.5	48.6	33.9	20.3	19.5	10.8
2.36	58.7	89.1	152.7	59.5	97.4	88.1	23.5	42.1	29	18.3	17.9	16.9
1.70	49.1	69.4	151.5	45.7	77	90.3	18.7	37.4	39.1	13.6	13.8	15.8
1.18	46	72	156.6	41.9	78.9	100.5	19.1	40.7	41.9	12.9	16.8	18.3
0.85	36.5	61.1	128.4	30.5	63.5	91.6	14.6	34.4	36.6	9.3	14.6	16.1
0.60	35	58.5	139.6	28.6	62.2	99.2	15.1	33.9	39.9	8.0	15.2	18.6
0.425	32.1	52.7	149.7	27.8	60.6	102.9	13.9	31.9	39	7.5	14.0	21.5
0.300	27.9	43.1	141.1	25.8	51	98	11.2	27.5	35.7	5.9	11.8	20.5
0.212	21.8	43	129.6	25.2	50	102	11.2	25.5	38.4	5.0	12.2	19.6
0.150	19.4	33.7	107.5	24.1	40.2	86.6	9	23.2	33.5	3.9	9.6	17.5
0.106	17.5	23.9	102	18.1	40.8	71.8	6.9	23.6	26.5	3.9	7.7	18.2
Pan (-0.106)	30.9	51.7	197.1	35.5	84.3	189.1	13.5	44.1	72.3	6.6	17.2	36.2
Sum (g)	2583.6	2664.4	2739.9	1551.5	1422.6	1485.5	502.6	546.2	510.9	188.2	190.3	240.7

Breakage Loss (g)	5.4	3.1	7.6	4.1	6.2	22.4	1.4	1.7	5.1	1.3	4.8	3.4
Loss Breakage (%)	0.208	0.12	0.28	0.26	0.43	1.48	0.28	0.31	0.98	0.68	2.45	1.38
Sieving loss (g)	1.4	2.2	5.2	3.7	1.1	1.1	1.3	1.3	3.2	0.3	0.7	1.5
Loss Sieving (%)	0.054	0.083	0.189	0.238	0.077	0.074	0.258	0.237	0.622	0.159	0.366	0.619

Table A-6: Breakage data for UG2 pyroxenite RoM ore sample run 2 showing the mass retained on the standard screens

Size (mm)	45.0 x 37.5			31.5 x 26.5			22.4 x 19.0			16.0 x13.2		
rpm	938	1408	2606	1408	2606	3915	1408	2606	3915	1408	2606	3915
E_{cs} (kWh/t)	0.10	0.25	1.00	0.25	1.00	2.50	0.25	1.00	2.50	0.25	1.00	2.50
No. of particles	30			30			30			30		
Initial mass				1508.9	1537	1626.6	530.7	573	606.8	211.5	221.5	196.8
After breakage				1504.2	1528.3	1608.9	529.1	569.6	596.2	211.5	220.3	195.2
45.0				0	0	0	0	0	0	0.0	0.0	0.0
37.5				0	0	0	0	0	0	0.0	0.0	0.0
26.5				37.1	0	0	0	0	0	0.0	0.0	0.0
19.0				204.2	26.7	0	27.5	0	0	0.0	0.0	0.0
13.2				336.4	74.9	10.5	49.9	26.3	0	6.5	0.0	0.0
9.50				218.6	116.3	22.4	101.2	42	22	21.8	5.2	0.0
6.70				118.3	159.5	66.3	81.6	48.7	13.5	47.4	16.5	3.2
4.75				119.2	138	88.9	43.5	55.7	19.9	31.6	15.7	6.4
3.35				80.1	119.8	99.9	43	48	33.1	16.1	19.1	8.0
2.36				60.6	113.8	99.8	32.9	46.3	35	16.8	18.5	8.6
1.70				46.4	101.1	88.7	23.1	35	36.1	10.6	14.5	9.3
1.18				49.2	104.7	108.7	22.2	41	45.1	10.7	15.7	11.8
0.85				36.8	86.5	97	17.4	33.3	40.6	8.0	13.6	11.3
0.60				40.9	87.1	120.2	16.7	33.7	44.2	8.2	13.6	14.4
0.425				37.4	78.8	121.3	15.2	30.6	43.4	7.9	14.5	17.4
0.300				29	67.5	117.1	12.7	25.6	42.8	6.0	13.5	17.1
0.212				24.4	60.4	124.4	11.6	26	45.4	6.0	13.3	19.2
0.150				18.4	49.7	111.5	8.8	19.3	40.4	4.5	12.4	17.5
0.106				14.8	46.8	100	8.1	17.2	43.1	3.4	12.7	15.9
Pan (-0.106)				30.7	93.8	228.4	12.8	37.8	87.6	6.0	21.1	33.9
Sum (g)	0	0	0	1502.5	1525.4	1605.1	528.2	566.5	592.2	211.5	219.9	194.0

Breakage Loss (g)	0	0	0	4.7	8.7	17.7	1.6	3.4	10.6	0	1.2	1.6
Loss Breakage (%)				0.31	0.57	1.09	0.30	0.59	1.75	0.00	0.54	0.81
Sieving loss (g)				1.7	2.9	3.8	0.9	3.1	4	0	0.4	1.2
Loss Sieving (%)				0.11	0.19	0.24	0.17	0.54	0.67	0.00	0.18	0.61

Table A-7: Breakage data for UG2 pyroxenite drill core sample run 1 showing the mass retained on the standard screens

Size (mm)	45.0 x 37.5			31.5 x 26.5			22.4 x 19.0			16.0 x13.2		
rpm	938	1408	2606	1408	2606	3915	1408	2606	3915	1408	2606	3915
E_{cs} (kWh/t)	0.10	0.25	1.00	0.25	1.00	2.50	0.25	1.00	2.50	0.25	1.00	2.50
No. of particles	30			30			30			30		
Initial mass				2181.5	2124.4	2101.2				222.3	216.7	214
After breakage				2176.8	2119.3	2095				219.9	213.1	209.4
45.0				0	0	0				0.0	0.0	0.0
37.5				0	0	0				0.0	0.0	0.0
26.5				345.3	0	0				0.0	0.0	0.0
19.0				542.5	150.3	18.8				0.0	0.0	0.0
13.2				603	409	162.2				73.9	0.0	0.0
9.50				182	298.4	216.3				51.4	18.8	4.1
6.70				114.9	183.9	211.5				21.8	41.2	6.5
4.75				67.8	157.4	153.5				19.1	18.6	13.1
3.35				49.7	96.9	132.2				10.2	19.8	18.2
2.36				40.5	88.3	120.2				7.4	14.2	17.3
1.70				33.5	99.6	109.8				6.3	15.1	14.7
1.18				32.1	98.4	118.8				5.9	14.1	17.6
0.85				24.2	79.8	94.1				4.4	11.0	15.2
0.60				24.2	74.1	100.2				3.8	10.7	14.8
0.425				21.9	68.5	95.1				3.6	9.7	14.9
0.300				19.3	63.5	96				2.4	7.4	13.5
0.212				18.6	57.1	101.3				2.3	7.8	12.8
0.150				14.2	46.4	82.4				1.8	5.7	11.2
0.106				11.5	44.1	69.3				1.5	4.6	10.4
Pan (-0.106)				28.7	100.7	210				2.9	11.5	23.6
Sum (g)				2173.9	2116.4	2091.7				218.7	210.2	207.9

Breakage Loss (g)				4.7	5.1	6.2				2.4	3.6	4.6
Loss Breakage (%)				0.22	0.24	0.30				1.08	1.66	2.15
Sieving loss (g)				2.9	2.9	3.3				1.2	2.9	1.5
Loss Sieving (%)				0.133	0.137	0.158				0.546	1.361	0.716

Table A-8: Breakage data for UG2 spotted anorthosite RoM ore sample showing the mass retained on standard screens

Size (mm)	45.0 x 37.5			31.5 x 26.5			22.4 x 19.0			16.0 x13.2		
rpm	938	1408	2606	1408	2606	3915	1408	2606	3915	1408	2606	3915
E_{cs} (kWh/t)	0.10	0.25	1.00	0.25	1.00	2.50	0.25	1.00	2.50	0.25	1.00	2.50
No. of particles	30			30			30			30		
Initial mass	3746.1			1087.5	1228.7			474.4		165.9	149.3	159.4
After breakage	3736.5			1084.6	1222.6			472.1		163.2	147.5	153.2
45.0	0			0	0			0		0.0	0.0	0.0
37.5	448.3			0	0			0		0.0	0.0	0.0
26.5	1105.2			25.7	0			0		0.0	0.0	0.0
19.0	733.9			150.1	0			0		0.0	0.0	0.0
13.2	455.1			292.9	36.8			0		3.2	0.0	0.0
9.50	220.1			147.2	62.4			6.5		32.3	0.0	0.0
6.70	197.3			126.3	76.5			25		13.1	5.7	0.0
4.75	97.9			60.2	112.3			24.6		24.4	9.2	1.8
3.35	82.5			51.3	98.3			28.7		14.8	11.1	4.6
2.36	55.7			35.4	74.7			28.8		13.2	9.4	6.6
1.70	39.6			25.7	70.3			27.4		8.4	9.5	5.8
1.18	37.8			25	74.2			32.5		8.3	10.8	8.5
0.85	34.1			21.7	72.2			32.4		7.3	10.3	8.2
0.60	39.5			23	88.7			40.8		7.6	12.4	11.2
0.425	39.9			23.6	91.1			46.6		7.3	13.6	14.4
0.300	36.9			20.8	85.3			44.8		5.8	12.4	15.8
0.212	27.4			17.1	82.1			37.6		5.4	11.7	19.1
0.150	23			13.5	58.6			28.9		3.7	9.2	16.4
0.106	19.8			12.2	45.8			23.8		2.6	8.1	13.3
Pan (-0.106)	39.4			24.1	90.9			42.9		5.1	13.2	26.2
Sum (g)	3733.4			1071.3	1220.2			471.3		162.5	146.6	151.9
Breakage Loss (g)	9.6			2.9	6.1			2.3		2.7	1.8	6.2
Loss Breakage (%)	0.256			0.26	0.50			0.48		1.63	1.21	3.89
Sieving loss (g)	3.1			0.8	2.4			0.8		0.7	0.9	1.3
Loss Sieving (%)	0.083			0.073	0.196			0.169		0.429	0.610	0.849

Table A-9: Breakage data for UG2 spotted anorthosite drill core sample showing the mass retained on standard screens

Size (mm)	45.0 x 37.5			31.5 x 26.5			22.4 x 19.0			16.0 x13.2		
rpm	938	1408	2606	1408	2606	3915	1408	2606	3915	1408	2606	3915
E_{cs} (kWh/t)	0.10	0.25	1.00	0.25	1.00	2.50	0.25	1.00	2.50	0.25	1.00	2.50
No. of particles	30			30			30			30		
Initial mass				1733.6	1723	1727.3				194.5	188.8	194
After breakage				1729.9	1718.4	1720.2				191.7	186.1	187.6
45.0				0	0	0				0.0	0.0	0.0
37.5				0	0	0				0.0	0.0	0.0
26.5				129.8	0	0				0.0	0.0	0.0
19.0				226	0	0				0.0	0.0	0.0
13.2				376.1	100	0				19.2	0.0	0.0
9.50				269.8	146.9	17.2				61.0	0.0	0.0
6.70				176.6	155.9	95.8				34.9	11.2	0.0
4.75				86.7	164.1	75.5				23.2	16.3	1.2
3.35				65.8	106.5	91.7				8.8	21.4	3.7
2.36				43.9	87.2	78.3				5.6	12.8	5.6
1.70				31.5	64.6	65				4.0	9.3	6.6
1.18				33.6	73	73.9				3.8	9.7	7.0
0.85				32.9	84.1	83.8				3.7	10.4	10.1
0.60				42.8	105.1	128.9				4.0	14.2	15.2
0.425				42.6	120.4	155.8				4.2	16.0	20.6
0.300				39.8	114.3	160.6				4.1	13.5	21.9
0.212				37.3	105.8	170				3.6	14.1	21.8
0.150				26.5	80.9	145.7				2.6	10.2	17.7
0.106				20.3	71.2	145				2.2	7.6	16.8
Pan (-0.106)				46	135.9	230.5				4.8	17.0	35.8
Sum (g)				1728	1715.9	1717.7				189.7	183.7	184

Breakage Loss (g)				3.7	4.6	7.1				2.8	2.7	6.4
Loss Breakage (%)				0.21	0.27	0.41				1.44	1.43	3.30
Sieving loss (g)				1.9	2.5	2.5				2	2.4	3.6
Loss Sieving (%)				0.110	0.145	0.145				1.043	1.290	1.919

Table A-10: Breakage data for UG2 mottled anorthosite RoM ore sample showing the mass retained on standard screens

Size (mm)	45.0 x 37.5			31.5 x 26.5			22.4 x 19.0			16.0 x13.2		
rpm	938	1408	2606	1408	2606	3915	1408	2606	3915	1408	2606	3915
E_{cs} (kWh/t)	0.10	0.25	1.00	0.25	1.00	2.50	0.25	1.00	2.50	0.25	1.00	2.50
No. of particles	30			30			30			30		
Initial mass	3376.8	3206.3	3213.4	1099.5	947.3	1018.5	474.5	435.2	443	179.6	181.3	190.2
After breakage	3375.5	3198.7	3199.6	1096.6	939.5	998.2	473.2	427.9	441.3	178.6	180.5	184.7
45.0	0	0	0	0	0	0	0	0	0	0.0	0.0	0.0
37.5	606.5	0	0	0	0	0	0	0	0	0.0	0.0	0.0
26.5	819.4	360.8	74.4	25.7	0	0	0	0	0	0.0	0.0	0.0
19.0	598.8	582.1	49.9	150.1	10.1	0	11.5	0	0	0.0	0.0	0.0
13.2	403.8	629.6	255.8	292.9	65.6	6.4	70.4	0	0	12.3	0.0	0.0
9.50	262.4	388.4	291.5	147.2	86.5	7.7	91	7.1	0	30.8	2.4	0.0
6.70	168	284.6	216.6	126.3	106.4	21.4	63.6	17.1	11.7	26.9	5.2	1.2
4.75	80.3	164	266.6	60.2	84.7	47.1	46.2	37.3	25	13.9	8.2	3.6
3.35	77.7	114.4	195.9	51.3	75.2	41.8	34.8	28.3	21.8	11.7	13.1	6.0
2.36	49.9	87.5	158.9	35.4	56.6	47.2	26	31.9	23.2	9.9	14.9	8.7
1.70	35.1	69.3	141	25.7	51.8	38.7	16.3	24.9	17.9	8.1	11.2	7.3
1.18	36.8	69	152.5	25	49.9	50	16.4	28.8	22	8.5	13.0	9.9
0.85	32.8	62.5	153.5	21.7	45.2	55.3	13.7	29.6	23.1	8.0	12.8	10.6
0.60	35.8	67.9	192.6	23	49.5	78.8	14.7	37.4	33.3	9.2	16.4	14.9
0.425	37.2	70.2	206.8	23.6	51	94.5	14.8	38.1	39.1	9.0	17.0	18.2
0.300	31.6	61.1	195.2	20.8	47	96	13	34.3	40.8	7.8	15.3	19.1
0.212	25.8	49.7	178	17.1	39.6	100.7	10.7	32.3	45	6.3	14.8	21.7
0.150	19.5	36.8	133.6	13.5	30.1	82.4	8.3	23.2	36.8	4.2	10.5	17.8
0.106	17.2	31	95.7	12.2	27.4	64.6	7.2	16.6	28.9	3.6	9.3	14.0
Pan (-0.106)	35.8	67.7	234.3	24.1	60.6	164.2	14.2	39.1	72	6.2	16.2	30.5
Sum (g)	3374.4	3196.6	3192.8	1095.8	937.2	996.8	472.8	426	440.6	176.4	180.3	183.5

Breakage Loss (g)	1.3	7.6	13.8	2.9	7.8	20.3	1.3	7.3	1.7	1	0.8	5.5
Loss Breakage (%)	0.038	0.24	0.43	0.26	0.82	1.99	0.27	1.68	0.38	0.56	0.44	2.89
Sieving loss (g)	1.1	2.1	6.8	0.8	2.3	1.4	0.4	1.9	0.7	2.2	0.2	1.2
Loss Sieving (%)	0.033	0.066	0.213	0.073	0.245	0.140	0.085	0.444	0.159	1.232	0.111	0.650

Table A-11: Breakage data for UG2 mottled anorthosite drill core sample showing the mass retained on standard screens

Size (mm)	45.0 x 37.5			31.5 x 26.5			22.4 x 19.0			16.0 x13.2		
rpm	938	1408	2606	1408	2606	3915	1408	2606	3915	1408	2606	3915
E_{cs} (kWh/t)	0.10	0.25	1.00	0.25	1.00	2.50	0.25	1.00	2.50	0.25	1.00	2.50
No. of particles	30			30			30			30		
Initial mass					1564					195.6	199.4	190.2
After breakage					1552.8					193.9	189	181.9
45.0					0					0.0	0.0	0.0
37.5					0					0.0	0.0	0.0
26.5					0					0.0	0.0	0.0
19.0					178.6					0.0	0.0	0.0
13.2					332.7					108.3	13.3	0.0
9.50					246.6					43.7	50.2	1.0
6.70					158.3					13.0	32.6	24.8
4.75					110.9					9.2	20.7	24.7
3.35					87.9					2.8	12.6	20.2
2.36					67.2					3.5	9.5	14.2
1.70					57.1					1.8	7.3	12.6
1.18					52.7					1.8	7.3	11.4
0.85					37.1					1.3	4.9	9.4
0.60					36.9					1.2	4.8	8.7
0.425					32.8					1.1	4.3	8.7
0.300					27.3					1.0	3.5	7.5
0.212					28.5					1.0	3.7	7.3
0.150					22.2					0.8	3.0	6.2
0.106					17.5					0.7	2.4	6.4
Pan (-0.106)					52.7					1.5	6.3	14.5
Sum (g)					1547					192.7	186.4	177.6
Breakage Loss (g)					11.2					1.7	10.4	8.3
Loss Breakage (%)					0.72					0.87	5.22	4.36
Sieving loss (g)					5.8					1.2	2.6	4.3
Loss Sieving (%)					0.374					0.619	1.376	2.364

B. APPENDIX B

2.1 Calculations

This section presents a summary of the calculation for the impact breakage tests.

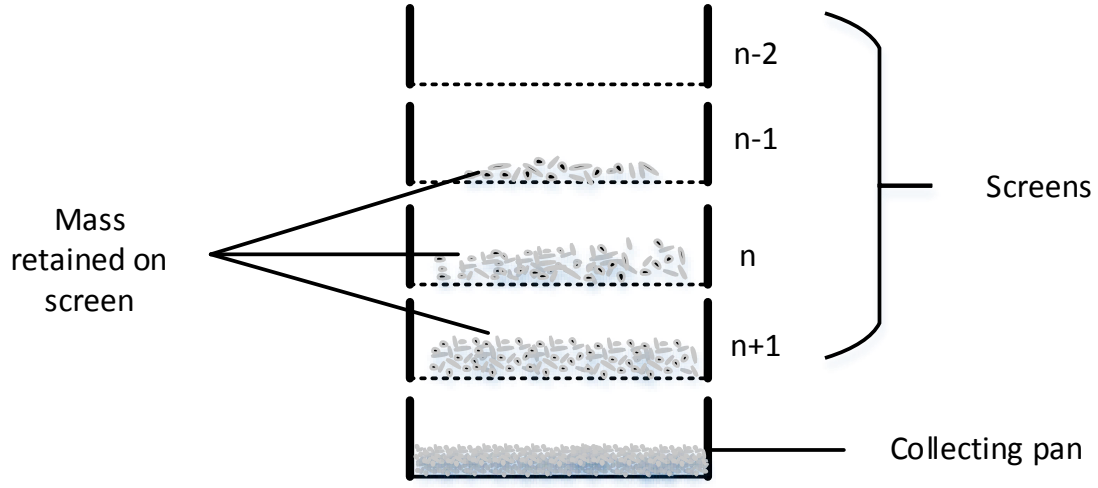

Figure B-1: Schematic diagram showing the mass retained on each screen

The following calculations are going to be used for the analysis of the progeny particles from the impact breakage in the RBT. The mass retained on screen (sieve) will be determined by weighing the particles collected on each screen.

$$Mass\ retained\ (g) = Weigh\ particles\ collected\ on\ each\ screen$$

The total mass retained is the sum of the masses retained at each screen. This should be equal to the original mass before screening.

$$Total\ mass\ retained\ (g) = \sum mass\ retained\ on\ each\ screen$$

The percentage retained is given by:

$$Percentage\ retained\ (\%) = \frac{Mass\ retained\ (g)}{Total\ mass\ retained\ (g)} \times 100$$

Cumulative percentage retained is obtained by adding up the percentages of the mass retained on each screen. This should total up to 100%.

$$Cumulative\ percentage\ retained\ (\%) = \sum Percentage\ retained\ on\ each\ screen$$

The percentage of material passing the nth sieve is calculated by the following equation:

$$\begin{Bmatrix} Percentage\ passing \\ n^{th}\ screen \end{Bmatrix} = \begin{Bmatrix} Percentage\ passing \\ n-1^{th}\ screen \end{Bmatrix} - \begin{Bmatrix} Percentage\ retained \\ on\ the\ n^{th}\ screen \end{Bmatrix}$$

If no mass is retained on a screen, the percentage passing is 100%. Usually, no mass is retained on the top screen, thus the percentage passing is 100%.

The original particle feed size is obtained by taking a geometric mean of the two screen sizes as given by the following equation:

$$Geometric\ mean = \sqrt{X_{top} \times X_{bottom}}$$

The t_{10} size is 1/10th of the original particle feed size.

$$t_{10,\ size} = \frac{Geometric\ mean}{10}$$

The percentage material passing 1/10th of the original feed size (t_{10}) is determined by interpolation.

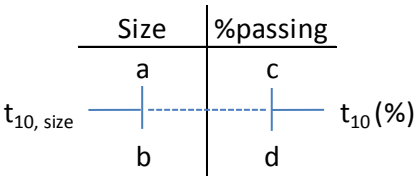

If a>b and c>d, t_{10} is then determined by the following equation:

$$t_{10}\ (\%) = \left[\left(\frac{t_{10,\ size} - b}{b - a}\right) \times (c - d)\right] + d$$

C. APPENDIX C

3.1 Particle size distributions

This section present a comparison of the particle size distributions obtained from the impact breakage test on the RoM ore and cut drill core samples.

3.1.1 UG2 Chromitite

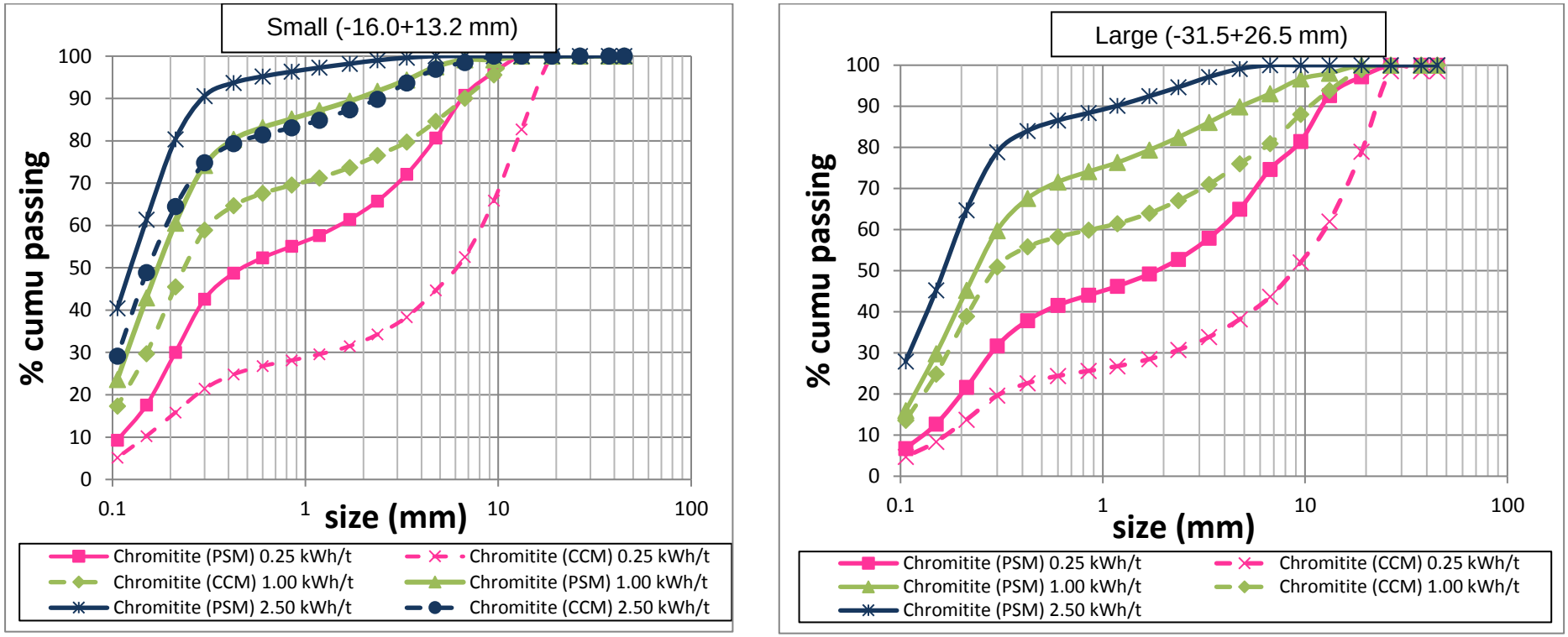

Figure C-1: Product size distribution for small and large chromitite particles

3.1.2 UG2 Pyroxenite

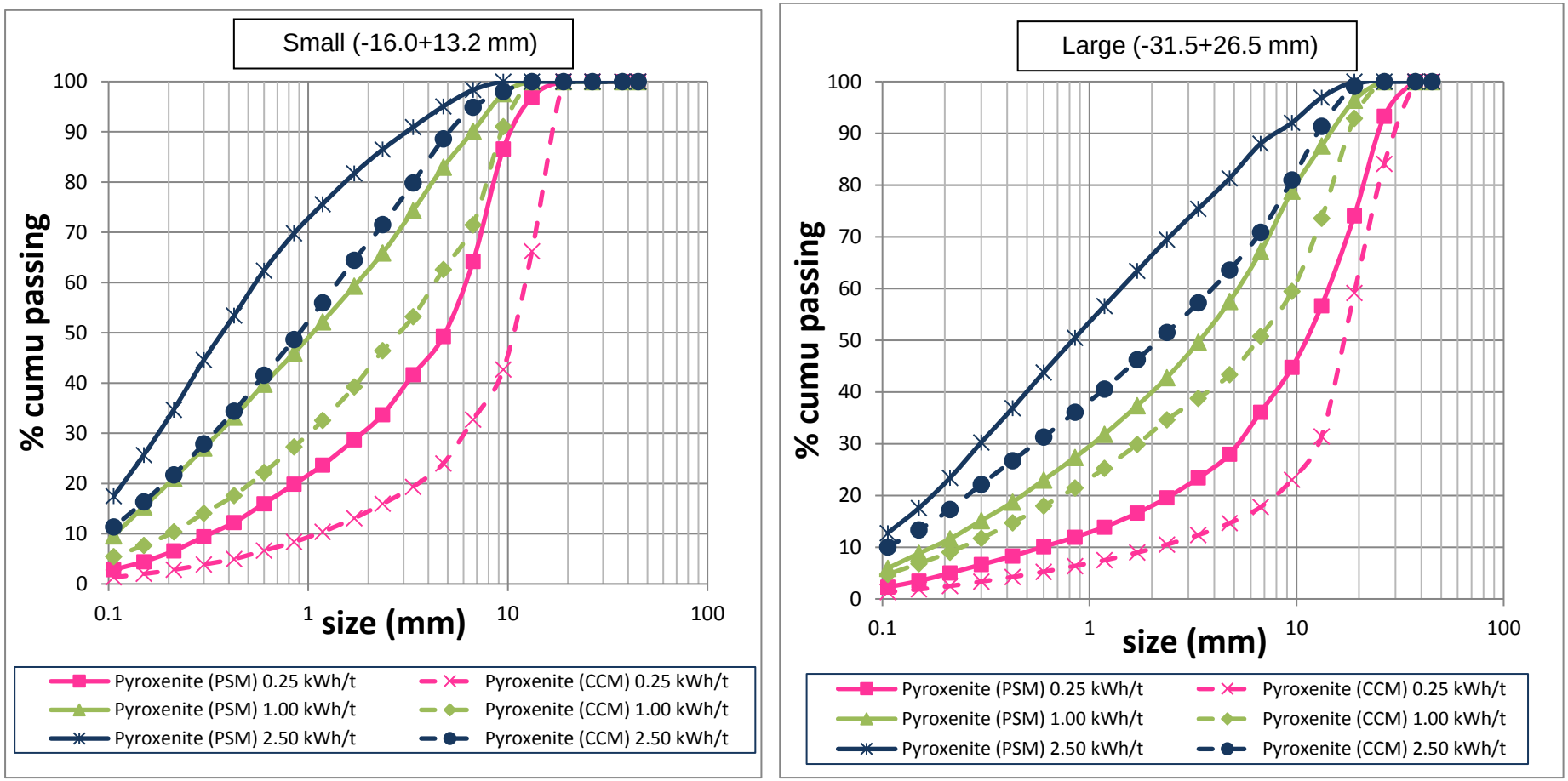

Figure C-2: Product size distribution for small and large UG2 pyroxenite particles

3.1.3 UG2 Spotted Anorthosite

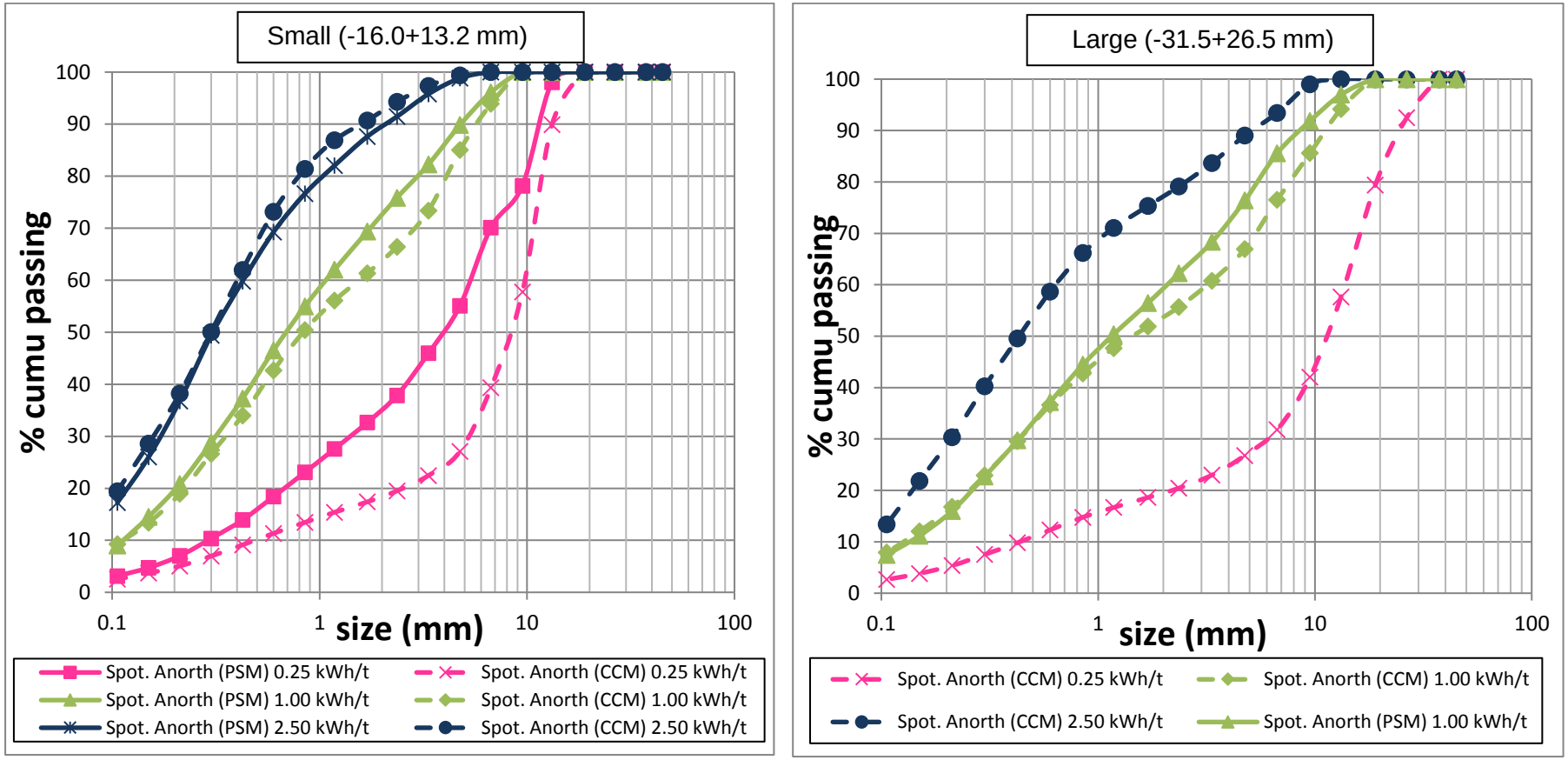

Figure C-3: Product size distribution for small and large UG2 spotted anorthosite particles

3.1.4 UG2 Mottled Anorthosite

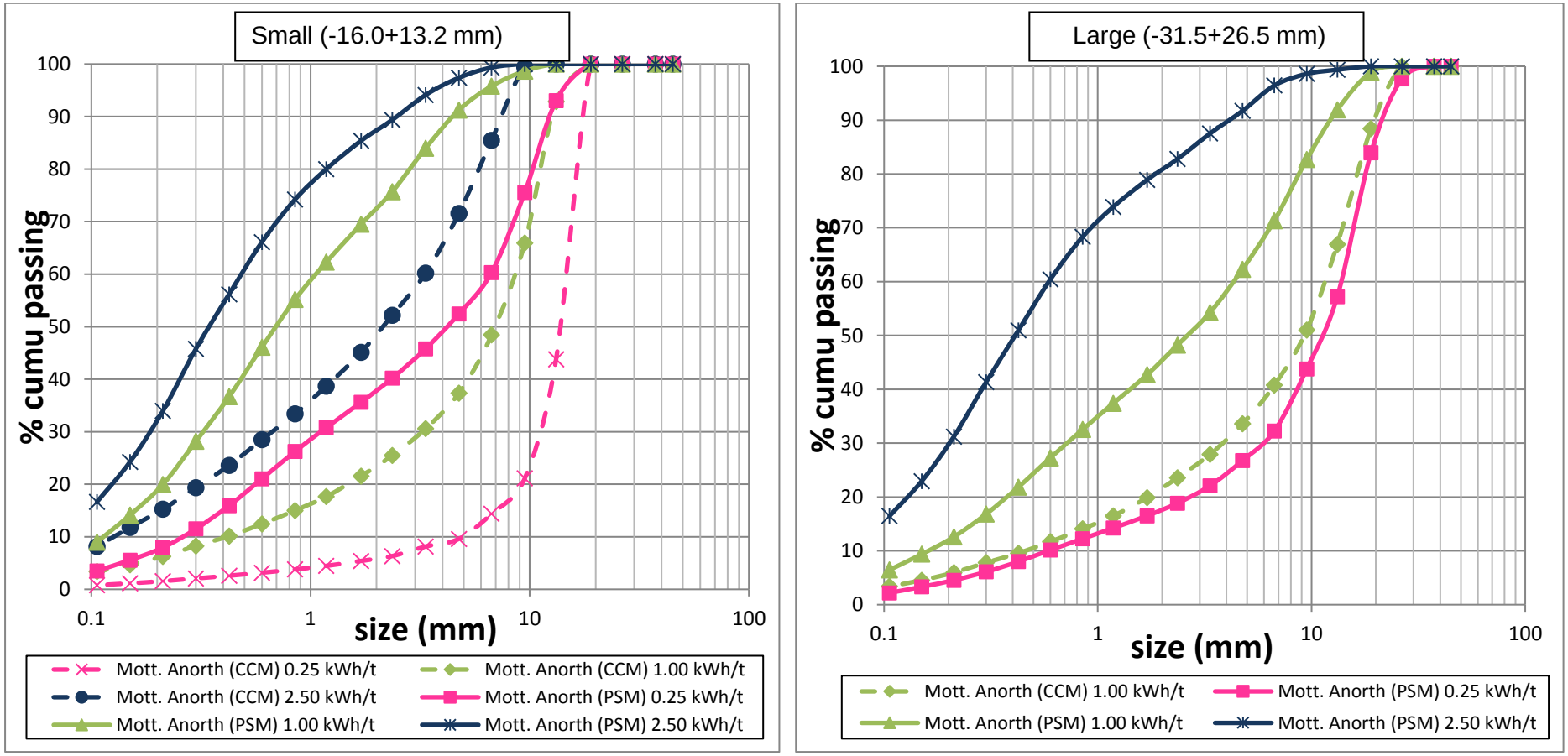

Figure C-4: Product size distribution for small and large UG2 mottled anorthosite particles

D. APPENDIX D

4.1 Degree of breakage (t_{10} parameters)

Rock type	Method	Size		Energy	Average t_{10}	Std. dev.
		Class	Range (mm)	(kWh/t)	(%)	
Chromitite	Particle Selection Method	Small	16mm x 13.2mm	0.25	60.4	0.80
				1.00	89.1	0.75
				2.50	97.8	1.13
		Medium	22.4mm x 19.0mm	0.25	56.9	0.73
				1.00	85.2	1.93
				2.50	96.4	0.99
		Large	31.5mm x 26.5mm	0.25	56.3	2.13
				1.00	83.5	1.18
				2.50	96.0	0.16
		V.Large	45.0mm x 37.5mm	0.10	28.6	1.81
				0.25	46.3	2.88
				1.00	81.4	1.55
	Cut Core Method	Small	16mm x 13.2mm	0.25	30.6	-
				1.00	72.5	-
				2.50	86.2	-
		Medium	22.4mm x 19.0mm	0.25	0.0	-
				1.00	0.0	-
				2.50	0.0	-
		Large	31.5mm x 26.5mm	0.25	32.4	-
				1.00	69.2	-
				2.50	0.0	-
		V.Large	45.0mm x 37.5mm	0.10	0.0	-
				0.25	0.0	-
				1.00	0.0	-
Pyroxenite	Particle Selection Method	Small	16mm x 13.2mm	0.25	28.3	2.77
				1.00	57.2	1.76
				2.50	76.3	3.49
		Medium	22.4mm x 19.0mm	0.25	25.5	0.95
				1.00	53.0	4.12
				2.50	75.9	0.70
		Large	31.5mm x 26.5mm	0.25	22.8	1.69
				1.00	50.7	5.97
				2.50	75.9	4.61
		V.Large	45.0mm x 37.5mm	0.10	16.1	-
				0.25	24.8	-
				1.00	60.3	-
	Cut Core Method	Small	16mm x 13.2mm	0.25	11.8	-
				1.00	36.1	-
				2.50	60.4	-
		Medium	22.4mm x 19.0mm	0.25	0.0	-
				1.00	0.0	-
				2.50	0.0	-
		Large	31.5mm x 26.5mm	0.25	11.5	-
				1.00	36.8	-
				2.50	54.6	-
		V.Large	45.0mm x 37.5mm	0.10	0.0	-
				0.25	0.0	-
				1.00	0.0	-

Rock type	Method	Size		Energy	Average t_{10}	Std. dev.
		Class	Range (mm)	(kWh/t)	(%)	
Mottled Anorthosite	Particle Selection Method	Small	16mm x 13.2mm	0.98	33.3	-
				0.98	66.1	-
				0.97	82.8	-
		Medium	22.4mm x 19.0mm	0.97	25.8	-
				0.96	68.8	-
				0.95	79.6	-
		Large	31.5mm x 26.5mm	0.95	20.6	-
				0.94	51.5	-
				0.94	85.3	-
		V.Large	45.0mm x 37.5mm	0.93	11.8	-
				0.93	23.0	-
				0.92	61.0	-
	Cut Core Method	Small	16mm x 13.2mm	0.92	5.0	-
				0.91	19.7	-
				0.90	42.1	-
		Medium	22.4mm x 19.0mm	0.90	0.0	-
				0.89	0.0	-
				0.89	0.0	-
		Large	31.5mm x 26.5mm	0.88	-	-
				0.88	25.9	-
				0.87	0.0	-
		V.Large	45.0mm x 37.5mm	0.87	0.0	-
				0.86	0.0	-
				0.86	0.0	-
Spotted Anorthosite	Particle Selection Method	Small	16mm x 13.2mm	0.85	30.3	-
				0.84	65.9	-
				0.84	85.0	-
		Medium	22.4mm x 19.0mm	0.83	-	-
				0.83	73.3	-
				0.82	-	-
		Large	31.5mm x 26.5mm	0.82	23.5	-
				0.81	65.5	-
				0.81	-	-
		V.Large	45.0mm x 37.5mm	0.80	11.7	-
				0.80	-	-
				0.79	63.0	-
	Cut Core Method	Small	16mm x 13.2mm	0.78	16.4	-
				0.78	58.8	-
				0.77	88.9	-
		Medium	22.4mm x 19.0mm	0.77	0.0	-
				0.76	0.0	-
				0.76	0.0	-
		Large	31.5mm x 26.5mm	0.75	21.8	-
				0.75	58.4	-
				0.74	81.6	-
		V.Large	45.0mm x 37.5mm	0.74	0.0	-
				0.73	0.0	-
				0.72	0.0	-

E. APPENDIX E

5.1 UG2 Spotted anorthosite

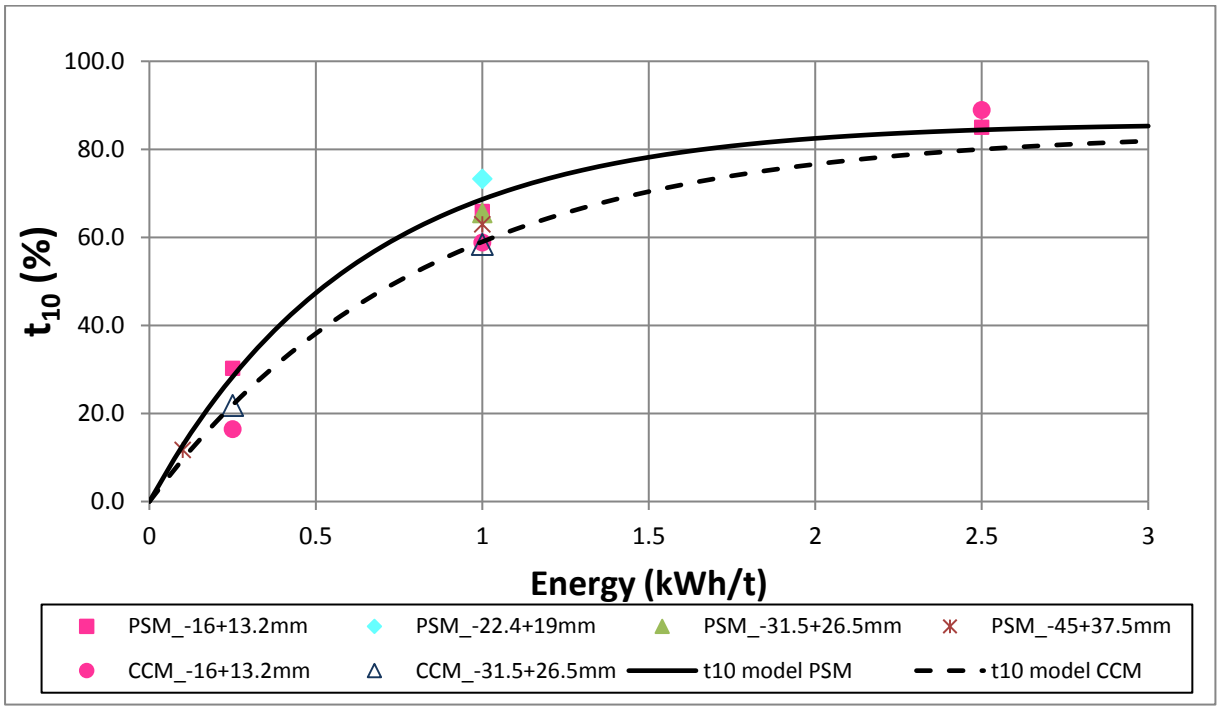

Figure E-1: t_{10} breakage model fitting to the t_{10}-E_{cs} data for UG2 spotted anorthosite rock particles

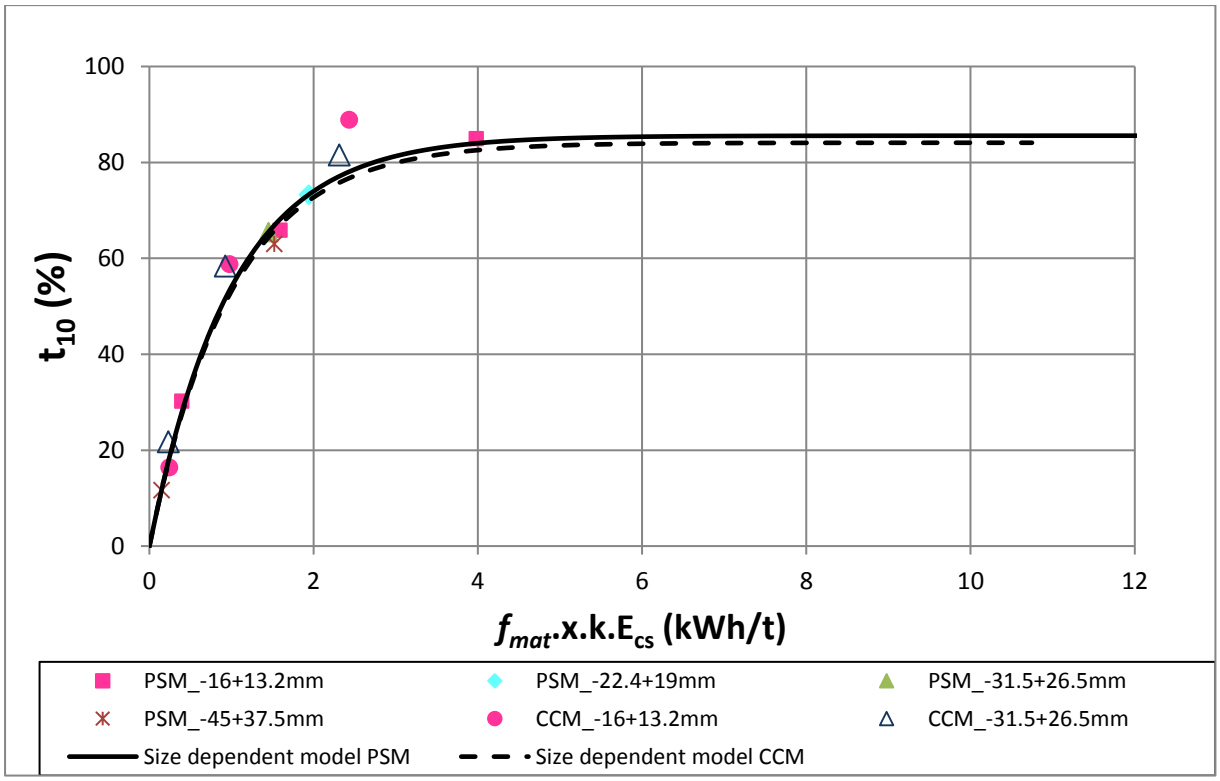

Figure E-2: Size dependent breakage model fitting to the particle selection and cut core breakage data for UG2 spotted anorthosite

5.2 UG2 Mottled anorthosite

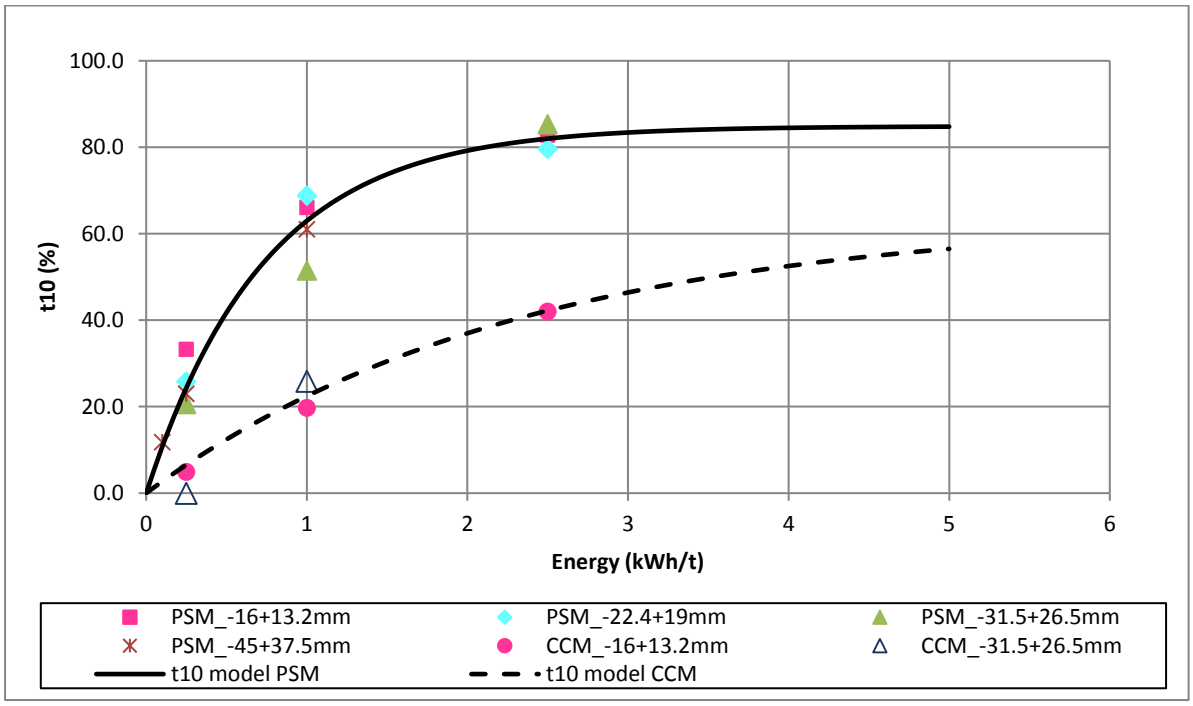

Figure E-3: t_{10} breakage model fitting to the t_{10}-E_{cs} data for UG2 mottled anorthosite rock particles

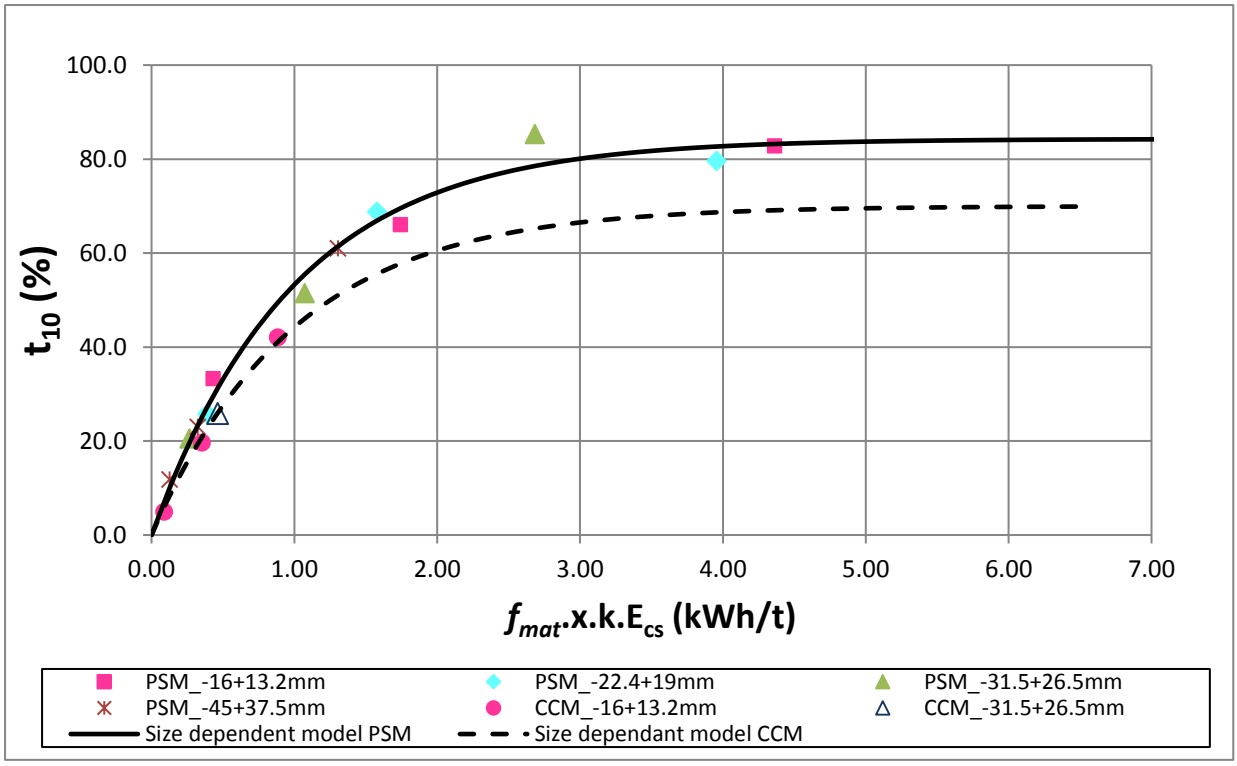

Figure E-4: Size dependent breakage model fitting to the particle selection and cut core breakage data for UG2 mottled anorthosite